CONSTRAINING MODIFIED GRAVITY USING GALAXY CLUSTER DYNAMICS

by

Eliza C. Diggins

A Senior Honors Thesis Submitted to the Faculty of
The University of Utah
In Partial Fulfillment of the Requirements for the

Honors Degree in Bachelor of Science

in Physics

Approved:

Dr. Daniel Wik Thesis Faculty Supervisor	Dr. Carsten Rott Chair, Dept. of Physics and Astronomy
Dr. Jordan Gerton Honors Faculty Advisor	Dr. Monisha Pasupathi Dean, Honors College

May, 2024

© May, 2024 Eliza C. Diggins

© May, 2024 Eliza C. Diggins
All Rights Reserved

ABSTRACT

Various sources of evidence, from galaxy rotation curves to the formation of cosmic structure, suggest the necessity of additional, unobserved, mass in the universe. Generally, these phenomena are attributed to "dark matter;" however, another potential approach is the modification of the theory of gravity. Modified Newtonian Dynamics (MOND) is the most popular of these and has successfully matched observations on galaxy scales and made several successful, *a priori* unexpected, predictions therein; however, the paradigm fails to match observations on larger scales, specifically in groups and clusters of galaxies. To rectify these tensions, various branches of MOND theory extensions have emerged; however, many of these introduce mathematical abstractions or additional free parameters which make these extensions difficult to refute or confirm. In this work, two such branches—EMOND and MOND plus Dark Matter (MOND+DM)—are challenged using observational and theoretical constraints which emerge from galaxy clusters. We apply the theoretical framework of these extensions to predict observable deviations from the ΛCDM paradigm, which could serve as observational tests of the MOND extensions in question. *CHANDRA* observations of a collection of galaxy clusters are used to constrain the asymptotic behavior of the cluster temperature profiles in each MOND branch. The assumption of hydrostatic equilibrium implies very tight constraints on the MOND phenomenology and introduces some non-trivial points of failure in both branches. We demonstrate that the MOND+DM paradigm may constrained by the imposition of hydrostatic equilibrium in galaxy clusters and several results are derived to that effect. We show that these constraints could be tested with upcoming X-ray missions, including XRISM. Further-

more, we illustrate significant inconsistencies in the EMOND paradigm which suggest that extension to be non-viable in clusters of galaxies. Modified gravity theories in the MOND research program continue to produce intriguing results on galaxy scales; however, classical theories of MOND gravity continue to fail on the cluster scale. In galaxy clusters, this work has demonstrated that MOND extensions make refutable predictions which should be detectable with current or upcoming observational technologies, signifying that each of these theories could be tested by observing missions. While the failure of these extensions doesn't necessarily indicate that MOND is fundamentally flawed, showing that these extensions fail to produce viable results clearly places the burden of progression on MOND theorists to establish MOND paradigms in which such phenomenology is no longer predicted.

TABLE OF CONTENTS

Page

ABSTRACT **ii**

LIST OF FIGURES **vii**

LIST OF ALGORITHMS **xiii**

1 Introduction **1**

1.1 Impetus 1

1.2 Background 3

1.2.1 MOND 4

1.2.2 Galaxy Clusters 14

1.3 Summary of Results 17

2 Modeling Galaxy Clusters **19**

2.1 Introduction 19

2.2 Clusters As We See Them 20

2.3 Idealized Models 26

2.3.1 Cluster Modeling: Baseline 26

2.4 The Cluster Sample 29

3 Constraining MOND Extensions **31**

3.1 MOND+DM 31

3.2 EMOND 39
3.2.1 Monte Carlo Constraints 46
3.3 Discussion 47
3.3.1 Fundamental Assumptions 49
3.3.2 MOND+DM 50
3.3.3 EMOND 51
3.4 Conclusion 53

4 Non-Equilibrium MOND Phenomenology in Clusters 54
4.1 Fluid Effects 54
4.1.1 The Mathematics of Infall 55
4.1.2 Shocks in Major Mergers 59
4.1.3 Ram Pressure Stripping 63
4.1.4 In a Newtonian External Field 65
4.1.5 In a MONDian External Field 67
4.2 Impacts 69

5 Discussion 70
5.1 Scientific Philosophy 71
5.2 Is MOND Refuted? 73
5.3 Is MOND Correct? 75
5.4 Moving Forward 76

6 Conclusion 79

Bibliography 81

Appendix A Non-Physical Correction 94
A.1 Introduction 94
A.2 Correcting Non-Physical Regions 95

A.2.1 The Naive Approach 96

A.2.2 Numerical Methods 97

Appendix B Mathematical Derivations **109**

B.1 MOND+DM Constraints 109

LIST OF FIGURES

Page

1.1 (Presumed) dark and phantom mass fractions for each of the 13 clusters in the sample. The total internal mass of each type was measured at $r_{\rm det}$ corresponding to the 3σ X-ray brightness boundary in the *Chandra* observations used to generate the models. The horizontal (vertical) line corresponds to the mean dark (phantom) mass ratio across the sample of clusters. The red line indicates the best linear fit to the scatter plot of the form $f_{\rm dm} = \alpha f_{\rm ph}$. In this sample, the missing mass problem is reduced by approximately 1/5 compared to the Newtonian case. . . . 9

1.2 Comparison of the Newtonian internal field and the MOND internal field in the asymptotic regime under the influence of an external field. Red fields are the MOND internal field, black fields are the Newtonian equivalent. Right hand panels show the phase difference between the fields (color) and the relative difference between their magnitudes (shaded). Note that relative difference is largely a function of $\nabla\Psi^E/a_0$. Units are set such that $[L] = \mathrm{Mpc}$, $[M] = \mathrm{M}_\odot$, and $G = 1$. 13

2.1 Collection of clusters showing several types of radio emission, shown in contours, overlaid onto the X-ray emission, shown in colors. Clusters are (from left to right and from top to bottom) A 2219 (halo), A 2744 (halo + relic), A 115 (relic), A 754 (complex, halo plus relic), A 1664 (relic), A 548b (relic), A 520 (halo), A 2029 (mini-halo), RXCJ1314.4-2515 (halo plus double relics). Figure adapted from Feretti et al. [50]. 22

2.2 Top six panels: Radial magnetic field intensity profiles at redshift zero. The figure presents the stacked profiles of the FOF groups in the virial mass bins indicated in each panel for the IllustrisTNG simulations. The solid blue line represents the (mass-weighted) median trend while the dark and light grey regions show the 1σ and 2σ spread around the median value, respectively. Bottom six panels: Radial profiles of β at redshift zero. To facilitate the comparison in the overlapping mass bins, we report the median relation for the TNG300 run in the TNG100 results as a blue dashed line. Adapted from Marinacci et al. [87]. . . . 23

2.3 Radial profiles of non-thermal pressure fraction, P_{NT}/P_{tot}. Solid lines show profiles calculated using turbulent velocities, and dashed lines show profiles calculated with velocity dispersions (see Section 2.4). Purple/pink lines show the profiles for FABLE at z = 0, 1, and 2, with shaded regions showing the 10–90th percentile scatter in the v_{turb} derived profiles at z = 0 and z = 2. Black dots show observational results from X-COP (Eckert et al. 2019). Dark blue lines show results from z = 0 in the simulations of Angelinelli et al. (2020) (though we note vturb has not necessarily been calculated in the same way). In light blue, we show representative z = 0 data from Pearce et al. (2020). Adapted from Bennett and Sijacki [20]. 25

2.4 A comprehensive diagram of the cluster generation processes used in `cluster_generator`. The left hand column indicates input quantities, the right hand side output quantities. The central column describes the different generation algorithms. Brackets following output quantities show the relative smoothness of the output. If the least smooth input function is $f \in C^n[a, b]$, then an output with a bracketed value k will be $g \in C^{n-k}[a, b]$. Values with 0 may be as smooth or more than the input. 28

3.1 Calculated values of r_{viable} and R_{viable} for each of the clusters in our sample. Overdensity radii were computed assuming a Plank18 cosmology [111]. Background shading represents the *Chandra* field of view for each of the clusters presented as described in Forman et al. [52]. Notably, inner boundaries were determined by the radius of the smallest annulus used for the temperature map and the outer boundary corresponds to detected X-ray brightness at $> 3\sigma$. In all but 2 cases (A2390, RXJ1159+5531), observed viability radii, r_{viable} were within r_{500}. . . . 33

3.2 Characteristic viability of galaxy clusters (as modeled by NFW profiles) in the MOND+DM paradigm. Data was produced by Monte Carlo simulation, calculating R_{viable} on set set of $N = 20,000$ randomly sampled NFW profiles. Profiles were constructed from their virial mass ($10^{13} - 10^{15}\text{M}_\odot$) and concentration parameter ($10 - 40$), and the maximal viable radius R_{viable} (image) was computed as well as the corresponding over-density at that radius (contours). Data was interpolated using the cubic Bezier scheme of Alfeld [7] as implemented in the `SciPy` package [140]. 35

3.3 Calculated temperature profiles for each of the galaxy clusters in the sample. Temperature profiles were computed in a pure AQUAL framework (wherein only the ICM is present) as well as an AQUAL+DM framework which includes a phantom mass component. In cases where the AQUAL and AQUAL+DM paradigms led to physical inconsistencies, the "minimal" correction approach was used to produce the best (physically viable) approximation to the original. In all but 1 cluster (RXJ 1159+5531), the necessary corrections were sufficient to force significant deviation in the resultant temperature profile. It should be noted that RXJ 1159+5531 and USG CS152 (excluded for plot spacing) are the only clusters in our sample which have R_{viable} outside of the *Chandra* field of view and therefore did not require any correction on that domain. 36

3.4 Calculated $A_0(\Phi)$ curves for each of the cluster models in our sample. The function $\alpha \exp(\Phi/\Phi_0)$ was fit using a least-squares approach to the calculated curves (black dashed). Panel A shows a symmetrically logarithmic scaling of the calculated $A_0(\Phi)$ curves as they pass through the gauge point at r_{200}. Panel B shows a zoomed version of panel A with standard logarithmic scaling to reduce visual artifacts. It should be noted that many cluster models do not appear to asymptote to the expected a_0 value at low potential and substantial scatter is observed in the best fit curve. 41

3.5 Calculated temperature profiles for each of the galaxy clusters in the sample. Temperature profiles were computed in the context of ΛCDM, and EMOND. Two EMOND cases are presented, one for which $A_0(\Phi)$ is free between clusters and one where it is fixed. Additionally, temperature profiles for the AQUAL+DM paradigm are also provided. In cases where the AQUAL+DM paradigms led to physical inconsistencies, the "minimal" correction approach was used to produce the best (physically viable) approximation to the original. In each of the clusters in the sample, EMOND was able to perfectly match temperature profiles when $A_0(\Phi)$ is freed; however, for the best fit model $\mathbf{A}_0(\Phi)$, each cluster showed easily detectable deviation from the observed temperature profile. 42

3.6 EMOND analysis of the idealized cluster models of section 3.2.1. (*upper left*) Generation parameters for each of the cluster models used in the cluster model. (*upper right*) Calculated $A_0(\Phi)$ curves for each of the simulated clusters. The heat map was created by applying a Gaussian kernel-density estimation algorithm to decompose individual curves into a representative PDF. The best fit curve was computed as the average of individual best fit models to each $A_0(\Phi)$ curve and has parameters $\varphi = 0.834\text{kpc}^2\text{Myr}^{-2}$ and $\Phi_0 = 0.80\text{kpc}^2\text{Myr}^{-2}$. The 95% confidence interval was generated by bootstrapping with $N = 1,000$ resamples. (*lower left*) Temperature profiles for each of the sample clusters in both the ΛCDM and EMOND paradigms. (*lower right*) The relative error in the EMOND temperature profile as compared to that of the ΛCDM equivalent. 48

4.1 Comparison of the expected Mach numbers ($\mathcal{M}$) in both the Newtonian and MOND regimes (left and center) as well as their ratio (right). Collision radii where 1 Mpc for the MOND regime and 500 kpc for the Newtonian regime. Infall distance was 16 Mpc in all cases. 62

4.2 Two composite images of so called jellyfish galaxies caused by ram pressure stripping. (Right) ESO 137-001 as it falls into the Norma galaxy cluster. Composite image is composed of observations in the visible (HST-ACS and HST-WFC3), in the millimeter band (orange, ALMA) and in the H-α band (Pink, VLT-MUSE). (Left) ESO 130-001 falling into Abell 3627 with two ram-pressure induced tails. In this image, blue tails are Chandra observations (X-ray) and red regions are H-α observations from SOAR. In both systems, high luminosity in H-α implies star formation in the gasseous tails. 64

4.3 Relative minimum ram pressure for stripping to occur in Newtonian and MONDian paradigms. Resulting curves are shown for interpolation functions of the form $\mu(x) = 1/(1 + x^{\alpha})^{1/\alpha}$. The ratio of the pressure thresholds is $G_{\mathrm{EFE}}(1 + \alpha_E)/G$. The quasi-linear domain is characterized by MOND systems which are significantly more robust against stripping, particularly for small α. In the Newtonian regime, the expected return to the asymptotic behavior appears. 68

LIST OF ALGORITHMS

Page

1 Hole-Identification Algorithm 101

2 Hole-Filling Algorithm 108

Chapter 1

Introduction

1.1 Impetus

Modern astrophysics (predicated upon general relativity, ΛCDM cosmology, and quantum mechanics) has achieved great success over the past century of development. Ever increasing precision, observing power, and data access continues to support, in almost all respects, the current paradigm; however, in the past three decades, emergent discrepancies also brought on by these improvements have continued to compound upon themselves without resolution. At the time of writing, we are no closer to a confirmation of the existence of dark matter than we were three decades ago. Furthermore, mounting evidence points to significant faults in our understanding of cosmology as exemplified by the Hubble Tension [69, 44], the σ_8 tension [110], the lithium problem [43], and others. Not only are these extant issues with the current paradigm well establish, they are also temporally persistent; a characteristic which suggests a possible "crisis" of the paradigm is imminent.

In an effort to shift the standard paradigm, novel theories of cosmology and gravity which no longer require dark matter have emerged in competition. While many of these so-called "modified gravity" theories have proven to be initially progressive

(in the sense of Lakatos [78]), most are susceptible to inconsistencies of the same or greater order of importance as those of the standard paradigm. A philosophical examination of the current state of theoretical astrophysics suggests that the field stands at a crossroads: either ΛCDM will regain its progressivity and render competitors superfluous or it will falter. If the later proves to be the case, a novel paradigm must emerge to takes its place, one which retains the impressive predictive power of ΛCDM while also accounting for its discrepancies. Even if ΛCDM proves to be irreparable, the field cannot progress until a novel paradigm emerges which can subsumes it.

In its current state, no modified gravity theory meets the necessary degree of self-consistency to be a candidate for replacing ΛCDM. Many different classes of modified gravity have been proposed; Modified Newtonian Dynamics (MOND) Milgrom [95] and it's relativistic formulations Bekenstein [19], $F(R)$ Gravity [105], Chameleon Gravity [146], etc. In each case, computational complexity, lack of theoretical constraint, and lack of falsifiability have (to differing extents) rendered many of these paradigms decidedly non-progressive. MOND stands out as one of the few paradigms to have achieved reasonable progressivity (see Merritt [94] for a review); however, it too faces significant challenges, including glaring inconsistencies in galaxy clusters. More recent developments in this theoretical framework have proven to be somewhat exculpatory [65, 102] and difficult to constrain; furthering the already consider lack of consensus in the field.

In an effort to contribute in a progressive way to the body of work regarding these questions, this work focuses on further constraining the MOND paradigm and its extensions using the observable properties of galaxy clusters. Our intention in doing so is two-fold: first, to further explore MOND in the context of galaxy clusters (where it is frequently overlooked). Second, to contribute to the construction of a more progressive heuristic for progress in the MOND paradigm.

1.2 Background

It is well established that gravitational systems in low acceleration regimes exhibit behaviors which are at odds with their apparent baryonic content. The appearance of this so-called missing mass is well established in many astrophyiscal systems, including galaxies [117] and clusters of galaxies [149]. The most common resolution to the missing mass problem (MMP) is to invoke some unseen massive component in these systems which would then be able to account for the observed dynamical differences without changing the observed, and well constrained, baryonic component of the system. Many candidates for such a source of unseen mass have been proposed; however, a great many of these candidates have since been eliminated as possible sources. Hypotheses using compact objects in these systems (so-called MACHOs) have been constrained by microlensing surveys [134, 80] as well as by measurments of the cosmic baryon fraction, which strongly constrain the possibility for baryonic dark matter [55]. Further explanations using more exotic forms of matter (those still well understood without altering the standard model) - particularly black holes at a variety of mass scales - have been sharply constrained by lensing surveys and would also create some inconsistencies with the cosmological predictions for the abundance of compact objects. Additionally, in the case of primordial black holes (PBHs), big bang nucleosynthesis (BBN) models place some constraints of PBH mass ranges because PBH formation would alter the neutron-to-proton ratio [34]. Nonetheless, some mass windows for black holes are still viable and actively explored as dark matter candidates [33, 22]. BBN also indicates that the baryon content of the universe, Ω_b, must be considerably smaller than the total mass content Ω_m, leading to the general consensus that any dark matter based theory most likely relies on some novel form of particulate mass [e.g. 118]. As with baryonic explanations for dark matter, many varieties of particle species have been proposed, of which a significant subset hold promise. Cosmological simulations by White et al. [147] indicate that hot (rela-

tivistic) dark matter theories (HDM) would be inconsistent with galaxy-survey based observations of structure formation in the universe. This has led to the adoption of cold (non-relativistic) dark matter (CDM) as the most viable explanation for the missing mass problem, and, in doing so, forms one of the theoretical pillars of the ΛCDM theory of cosmology, which is widely consistent with observation.

Despite the broad success of ΛCDM, there remain a few inconsistencies between theoretical prediction and observation. Of greatest significance is the persistent failure to directly detect particulate dark matter [1, 2, 8]. Furthermore, there are a litany of smaller observational inconsistencies including the tension in σ_8 and in the Hubble constant as well as the core-cusp problem in galaxy clusters and the apparent viability of the Baryonic Tully Fisher Relation. For a recent review of tensions in ΛCDM, see Perivolaropoulos and Skara [110]. Additionally, the recent launch of the James Webb Space Telescope (JWST) and its observations of galaxies at extreme redshift has introduced some degree of tension with ΛCDM [77]. While none of these weaknesses is capable of undermining ΛCDM to the point of forcing a paradigm shift, they do each represent areas of the ΛCDM paradigm which should be tested and challenged to better understand the underlying cause of the inconsistencies.

1.2.1 MOND

An alternative to the dark matter paradigm is to instead modify gravitational theory to resolve the MMP. The archetype of these modified gravity theories is MOND, which was originally proposed in 1983 [95, 96] with the core intention of resolving the rotation curve problem observed by Rubin and Ford Jr [117]. To this end, MOND proposes 3 core axioms

1. Gravity behaves non-classicaly in low acceleration regimes below some fundamental a_0.

2. In the aforementioned limiting case, the acceleration is altered such that

$$\frac{a}{a_0}\mathbf{a} = \mathbf{g}_N = \mathbf{a}_N, \tag{1.1}$$

where $\mathbf{g}_N$ is the equivalent, Newtonian gravitational field strength.

3. The transition from the Newtonian regime ($a \gg a_0$) to the deep MOND regime, or DMR, ($a \ll a_0$) occurs over a range of accelerations around a_0.

The final axiom is implemented using an *interpolation function* which connects the two asymptotic regimes and would presumably arise from a more fundamental theory.

This first theory in the MOND research program has many flaws, chief among them being its relevance only to spherically symmetric systems, and its failure to obey some of the necessary conservation laws. Nonetheless, this theory made several predictions which were, *a priori*, unexpected in the ΛCDM paradigm. These include the Baryonic Tully-Fisher relation (BTFR), which predicts that the asymptotic speed of disk galaxies should scale with $M^{1/4}$ [95], and the Radial Acceleration Relation (RAR), which predicts a relationship between the predicted Newtonian acceleration $\mathbf{g}_N$ and the observed acceleration $\mathbf{a}$ in galaxies. Both of these relations have been widely corroborated by observational studies [84, 93, 139].

Several classical field theories have been introduced which lead to the phenomenology laid out above. The two most common are AQUAL [18] and QUMOND [100]. The AQUAL framework relies on a non-linear field lagrangian of the form

$$\mathcal{L} = \frac{\rho v^2}{2} - \rho\Phi - \frac{a_0^2}{8\pi G}\mathcal{F}\left(\frac{|\nabla\Phi|^2}{a_0^2}\right), \tag{1.2}$$

where ρ is the mass density, v is the velocity field, Φ is the gravitational potential, and $\mathcal{F}$ is an arbitrary function subject to the constraint that $\mathcal{F}(x) \to x$ in the Newtonian regime, and $\mathcal{F}(x) \to (2/3)x^{3/2}$ in the DMR. Variation of the Lagrangian with respect

to the position yields the typical form of Newton's Second Law ($\mathbf{a} = -\nabla\Phi$), implying that the relationship between acceleration and potential remains valid. On the other hand, variation of the Lagrangian with respect to the field itself (See Landau [79] for a detailed description of the approach) yields a modified Poisson equation of the form

$$\nabla \cdot \left[\mu \left(\frac{|\nabla\Phi|}{a_0} \right) \nabla\Phi \right] = 4\pi G\rho, \tag{1.3}$$

where $\mu(x) = d\mathcal{F}/dz$ and $z = x^2$. This $\mu(x)$ is precisely the interpolation function described in the original theory.

Similar phenomenology is produced by the QUMOND framework with a somewhat easier mathematical formulation. QUMOND utilizes two scalar fields, Ψ and Φ, the former being the classical, Newtonian, field and the later being the "true" field which mediates the system's behavior. The Lagrangian takes the form

$$\mathcal{L} = \frac{1}{2}\rho v^2 - \rho\Phi - \frac{1}{8\pi G} \left[2\nabla\Phi \cdot \nabla\Psi - a_0^2 \mathcal{Q} \left(\frac{|\nabla\Psi|^2}{a_0^2} \right) \right], \tag{1.4}$$

where $\mathcal{Q}$ plays a role similar to $\mathcal{F}$ in equation 1.2 but instead has asymptotic behavior $Q(z) \to z$ for $z \gg 1$ and $Q(z) \to (4/3)z^{3/4}$ for $z \ll 1$. The resulting field equations are

$$\begin{aligned} \nabla^2\Psi &= 4\pi G\rho \\ \nabla^2\Phi &= 4\pi G\hat{\rho} = \nabla \cdot \left(\eta \left(\frac{|\nabla\Psi|}{a_0} \right) \nabla\Psi \right), \end{aligned} \tag{1.5}$$

where η is the QUMOND interpolation function $\eta(y) = d\mathcal{Q}/dy^2$. In general, QUMOND and AQUAL do not yield the same results as each Poisson equation may be written as the curl of a field, which is generally different between theories. In spherical systems,

with which we are primarily interested,

$$\underbrace{\eta\left(\frac{|\nabla\Psi|}{a_0}\right)\nabla\Psi - \nabla\Phi}_{\text{QUMOND}} = \underbrace{\mu\left(\frac{|\nabla\Phi|}{a_0}\right)\nabla\Phi - \nabla\Psi}_{\text{AQUAL}}.$$

Thus, QUMOND and AQUAL are equivalent if and only if the two interpolation functions used are connected in such a way that $y = \eta(x)x \implies x = \mu(y)y$ for all choice of x or y. Such functions will be referred to as *Milgromian* inverses and denoted by $\mu = \eta^{\dagger}$. In several cases throughout this work, direct knowledge of the Milgromian inverse allows for simplified computations. For a more comprehensive account of MOND's theoretical underpinnings and observational success, see Merritt [94].

Further work on the MOND paradigm has largely focused on determining a relativistic theory which comprehensively replicates the desired MOND phenomenology while preserving the central tenants of General Relativity. Many such theories have been proposed [19, 126, 98]; however, there has been very little progress in determining a favored theory upon which to level observational challenges. Furthermore, many relativistic MOND theories rely on different geometric and physical metrics, which typically produce a difference in the predicted speed of gravitational waves from the speed of light. Recent observations appear to be at odds with such statements [122]; however, recent work in relativistic MOND extensions have shown that MOND theories do exist wherein gravitational waves travel at the speed of light [127].

Much of this theoretical focus in the MOND paradigm focuses on establishing a relativistic theory which would provide a comprehensive foundation for MOND cosmology. While this is certainly an important area of inquiry, the failure of the paradigm to produce a theory which is accepted and which can hold up to scrutiny has made this area of MOND research rife with indemnifying arguments in the face of contradictory observational findings. Outside of the relativistic regime, MOND

remains significantly at odds with observational data in clusters of galaxies [5, 58, 48]. An illustration of this is provided in Figure 1.1, which presents both the dark matter fraction and phantom matter factions computed for each of the clusters in our sample. In this set of 13 clusters, MOND appears to reduce the need for "missing mass" by approximately 20%; thus persisting the necessity of some additional missing mass component, be it baryonic or otherwise. Some argument has been made that these discrepancies may represent some persistent missing mass in galaxy clusters which is nonetheless still of a baryonic origin [94, 97]. Others have attempted to expand the MOND paradigm [65, 148] and still other theorists have modified the core MOND theory to account for the discrepancy (among other reasons). The most prominent of these later approaches is the theory of superfluid dark matter proposed by Berezhiani and Khoury [21], which has demonstrated some degree of viability in galaxy clusters [66].

In this work, we demonstrate significant persisting tension in two popular MOND extensions: Extended MOND (EMOND) and MOND+DM. To demonstrate the significant degree of tension which still persists in each of these theories, we utilize the galaxy cluster sample from Forman et al. [52] to explore the implications of galaxy cluster microphysics in relation to predict MOND phenomenology. The remainder of this paper is laid out as follows: in Sections 1.2.2 and 2.2, we discuss the relevant physics in galaxy clusters for our analysis, in Section 3.1 we describe derivable constraints on the MOND+DM paradigm both from a theoretical perspective and through demonstrated analysis on our cluster sample. Similarly, Section 3.2 introduces the EMOND extension and describes it's successes in galaxy clusters. We demonstrate two different approaches to the application of EMOND and discuss the constraints which can be placed on both approaches. Finally, in Section 3.3, we discuss the implications of our findings on the MOND paradigm as a whole and describe several interesting prospects for further observational tests of MOND extensions using

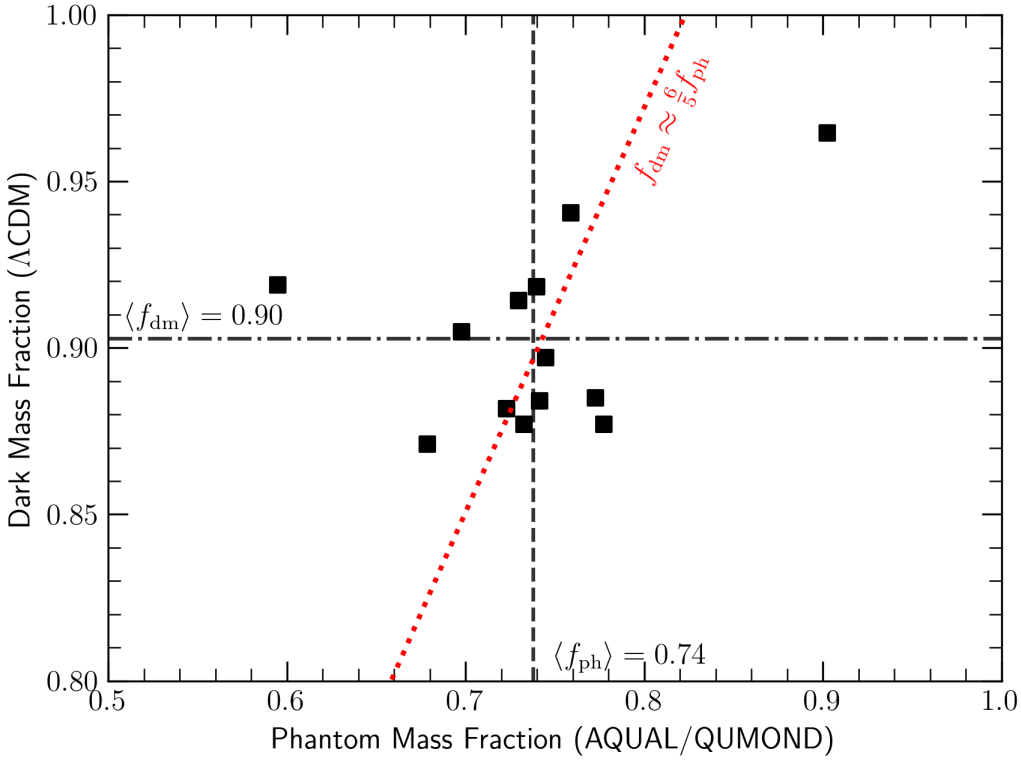

Figure 1.1: (Presumed) dark and phantom mass fractions for each of the 13 clusters in the sample. The total internal mass of each type was measured at $r_{\rm det}$ corresponding to the 3σ X-ray brightness boundary in the *Chandra* observations used to generate the models. The horizontal (vertical) line corresponds to the mean dark (phantom) mass ratio across the sample of clusters. The red line indicates the best linear fit to the scatter plot of the form $f_{\rm dm} = \alpha f_{\rm ph}$. In this sample, the missing mass problem is reduced by approximately 1/5 compared to the Newtonian case.

upcoming observational missions.

The External Field Effect

Among the most significant predictions of the MOND paradigm arises from the explicit non-linearity of its Poisson equations. Consider the AQUAL Poisson equation of the form

$$\nabla \cdot \left[\mu \left(\frac{|\nabla \Phi|}{a_0} \right) \nabla \Phi \right] = 4\pi G \rho.$$

If one then considers the phenomenology of a uniformly accelerating frame relative to that of a frame in an external field, it is apparent that the center of mass motion does not separate from the expression and therefore that the strong equivalence principle is violated by MOND. This effect, called the *External Field Effect* is a critical aspect of MOND phenomenology and drives many predictions of the paradigm. One such prediction, laid out in McGaugh and Milgrom [91] and tested in McGaugh and Milgrom [92], is that a comparison between two dwarf satellites of similar morphology but within different regimes of the external field should have manifestly different velocity dispersions. This assertion was corroborated by McGaugh and Milgrom [92]; however, they failed to obtain sufficiently high quality measurements so as to reach typical standards for statistical significance. Further evidence for the external field effect has been found, most interestingly in the work of Chae et al. [38], which claims to have detected the EFE to within 11σ significance. Further work regarding the behavior of wide-binaries, which would be ideal testbeds for the EFE, indicate that there are discrepancies from the classical expectation[36, 63]. Nonetheless, as a competing paradigm, these results must achieve a higher degree of significance and be replicated before anything can be said with confidence regarding the correctness of the MOND paradigm.

While the EFE is largely described in a phenomenological context, it is possible to derive the far field / asymptotic behavior of the fields. In the remainder of this section, we present the derivations as described in Bekenstein and Milgrom [17]. Considerable detail has been dedicated to this derivation for two reasons. Firstly, the EFE is of significant importance in our discussion of cluster mergers and their dynamics in later sections. Secondly, the results are highly non-intuitive and very much worth understanding.

Consider a system S embedded in an external gravitational field which is, on the scale of S, effectively uniform with acceleration $\mathbf{a}_{ext}$. It is well established [e.g. 17] that the weak equivalence principle does hold and that the center of mass in S accelerates with the external field; however, the internal dynamics of the system may be impacted by the external field. A test particle in S experiences acceleration

$$\mathbf{a}_{int} = \mathbf{a}_g - \mathbf{a}_{\text{ext}} = -\nabla\delta = -\nabla\Phi - (-\nabla\Psi^E),$$

where δ is the *effective field* driving the internal dynamics of the system, Ψ^E is the external field, and Φ is the "true" field. The Bekenstein-Milgrom equation depends on Φ which does not allow for δ and Ψ^E to separate.

If $|\nabla\Psi^E| \gg a_0$, then $|\nabla\Phi - \nabla\Psi^E| \sim |\Psi^E| \gg a_0$ and the dynamics are asymptotically Newtonian with the WEP being respected in this special case. If the external field is smaller than a_0, the dynamics are considerably more complex. Letting $\mathbf{x} = \hat{e}_E + |\nabla\Psi^E|^{-1}\nabla\delta$ and $w = |\nabla\Psi^E|/a_0$,

$$\mu\left(\frac{|\nabla\Phi|}{a_0}\right)\nabla\Phi = a_0\mu\left(|\mathbf{x}|w\right)w\mathbf{x} \approx a_0 w\mu_E\hat{e}_E + \left[a_0 w\mu_E\mathbf{I} + a_0 w^2\mu'_E\hat{e}_E\right]|\nabla\Psi^E|^{-1}\odot\nabla\delta,$$

Where the final expansion is obtained from a Taylor expansion about $\mathbf{x} = \hat{e}_E$. If one integrates over some surface $\partial\Sigma$ where the surface is sufficiently far from the

embedded mass distribution that the above approximation is valid, then

$$\oiint_{\partial\Sigma} \mu\left(\frac{|\nabla\Phi|}{a_0}\right)\nabla\Phi\cdot d\mathbf{S} \approx \underbrace{\oiint_{\partial\Sigma} a_0 w \mu_E \hat{e}_E \cdot d\mathbf{S}}_{=0} + \oiint_{\partial\Sigma} \mu_E \nabla\delta\cdot d\mathbf{S} + \left.\frac{d\mu}{d\ln(z)}\right|_{z=\nabla\Psi^E/a_0} \oiint_{\partial\Sigma} \left(\hat{e}_E\cdot\nabla\delta\right)\left(\hat{e}_E\cdot d\mathbf{S}\right), \tag{1.6}$$

Where $\mu_E = \mu(|\nabla\Psi^E|/a_0)$. We therefore obtain an expression from Gauss' Theorem of the form

$$\oiint_{\partial\Sigma} \nabla\delta\cdot d\mathbf{S} + L_E \oiint_{\partial\Sigma} \left(\hat{e}_E\cdot\nabla\delta\right)\left(\hat{e}_E\cdot d\mathbf{S}\right) = 4\pi G M_{\mathrm{dyn}}(<r)\mu_E^{-1}.$$

Where $L_E = d\ln(\mu)/d\ln(x)$ where $x = |\nabla\Psi^E|/a_0$. If $\partial\Sigma$ has a surface area which grows characteristically as r^2, then for M_{dyn} to be stable at large radii, $\nabla\delta \sim r^{-2}$. By symmetry, one also expects that the field should depend (in cylindrical coordinates with $\hat{e}_E = \hat{z}$) on r and z only. Therefore, the ansatz $\nabla\delta = r^{-2}k(\theta, r) + \mathcal{O}(r^{-3})$ leads directly to the key result:

$$\nabla\delta(\theta, r) \approx \frac{M_{\mathrm{dyn}}}{r^2}\underbrace{\left(G\mu_E^{-1}(1+L_E)^{-1/2}\right)}_{G_{\mathrm{EFE}}}(\hat{e}_r - \alpha_E\cos(\theta)\hat{e}_z)(1-\alpha_E\cos^2(\theta))^{-3/2}. \tag{1.7}$$

Equation 1.7 is the Bekenstein-Milgrom EFE Equation (henceforth BMEE). The interesting result in this case is that the field acts in a *quasi-newtonian* way with a r^{-2} dependence, but with a modified G_{EFE}. This equation will be of critical importance in some of the analytical aspects of this work. Figure 1.2 depicts the asymptotic fields in a variety of different scenarios for $\nabla\Psi_E$ and provides the corresponding G_{EFE}. It should be noted that for sufficiently low accelerations, the quasi-Newtonian G may be many orders of magnitude larger than the classical value.

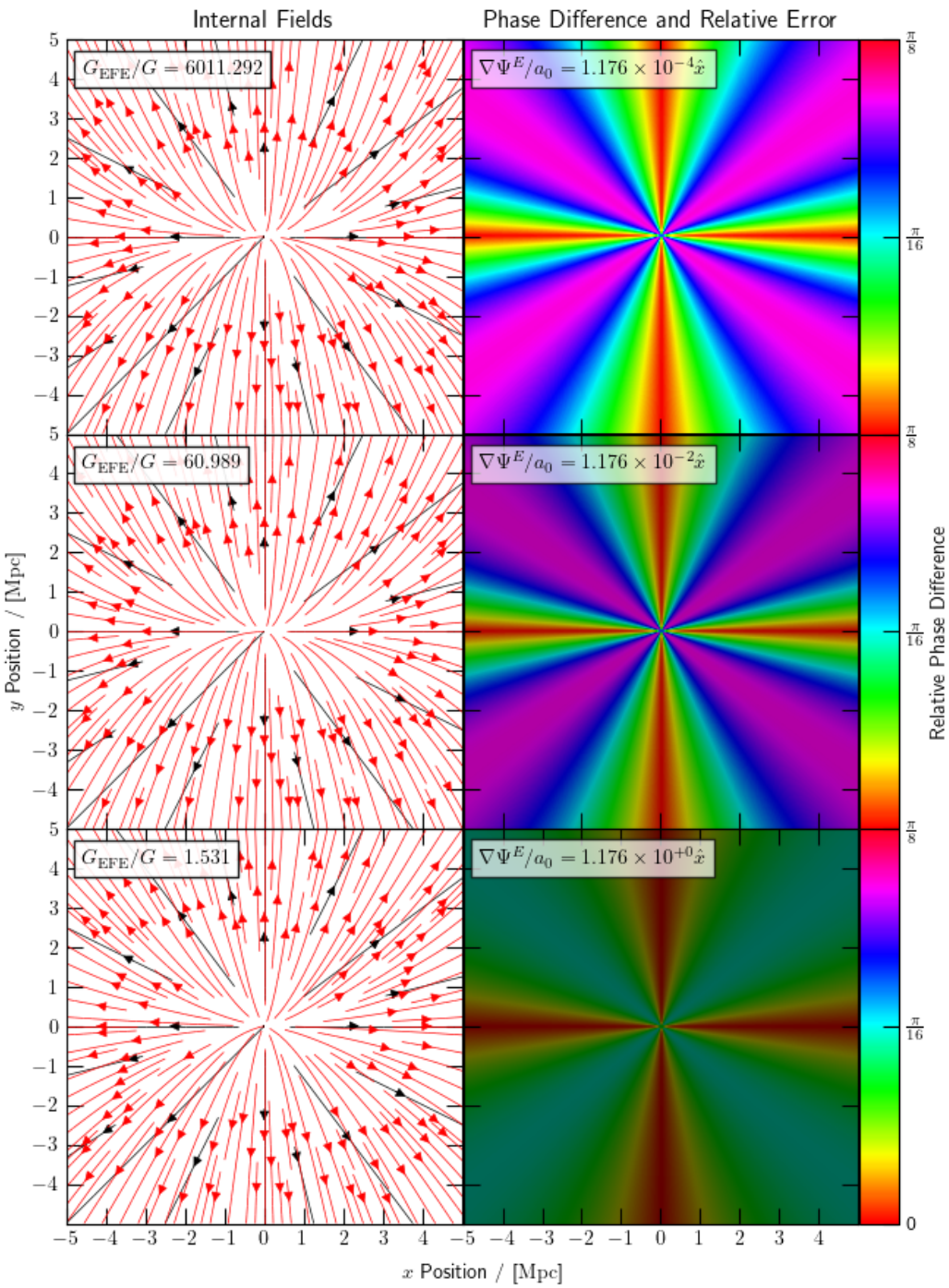

Figure 1.2: Comparison of the Newtonian internal field and the MOND internal field in the asymptotic regime under the influence of an external field. Red fields are the MOND internal field, black fields are the Newtonian equivalent. Right hand panels show the phase difference between the fields (color) and the relative difference between their magnitudes (shaded). Note that relative difference is largely a function of $\nabla\Psi^E/a_0$. Units are set such that $[L] = \text{Mpc}$, $[M] = \text{M}_\odot$, and $G = 1$.

1.2.2 Galaxy Clusters

Galaxy clusters form the largest dynamically stable structures in the universe with dynamical masses on the order of $10^{13} - 10^{15}$ $M_\odot$ and physical sizes on the order of mega parsecs [123]. In optical observations, galaxy clusters typically host on the order of 100-1000 bright galaxies within their gravitational well; however, the most significant massive components of galaxy clusters are the hot intracluster plasma (ICM) and the (apparent) dark matter halo. Typical galaxy clusters are composed of only $\sim 5\%$ stellar mass, with an additional $\sim 15\%$ contributed by the ICM and the remaining $\sim 80\%$ from the presumed dark matter content [119]. The ICM radiates in the X-ray via thermal bremsstrahlung[29], which produces an exponential emission spectrum. Spectral observations of these systems indicate temperatures on the order of 10 keV. Emission spectra may then be fit to those observed in concentric annuli to provide a 2D temperature map of the cluster. A model of ICM temperature may then be fit to the observed profile after projection along the line of sight and convolution with the PSF. Similarly, the gas density can be obtained from the observed surface brightness following a similar procedure. For a comprehensive account of the analysis approaches used in this process, see Eckert et al. [48].

The end product of this analysis approach is to produce radial profiles of the gas temperature T_g, and gas density ρ_g of the ICM. These analyses are typically predicatated on the assumption of spherical symmetry and on the assumption that the ICM plasma is in thermal equilibrium [29, 52, 48]. While each of these assumptions introduces some degree of uncertainty, systematic studies have succeeded in producing reasonable constraints on both of these error contributions [24, 30, 31].

Hydrostatic Equilibrium

Pressure support against gravitational collapse in the ICM may be exploited to determine dynamical masses for galaxy clusters. This is typically done by treating the

ICM as a classical fluid subject to the incompressible Euler equation

$$\frac{D\mathbf{u}}{Dt} = \frac{\partial \mathbf{u}}{\partial t} + (\mathbf{u} \cdot \nabla)\mathbf{u} = -\frac{1}{\rho_g}\nabla p + \mathbf{g}, \tag{1.8}$$

where $\mathbf{u}$ is the velocity field of the fluid, p is the pressure, ρ_g is the gas density, and $\mathbf{g}$ is the gravitational acceleration. If the system is in HSE ($D\mathbf{u}/Dt = 0$), then the Euler equation reduces to

$$\frac{\nabla p}{\rho_g} = \mathbf{g}.$$

The standard assumption in galaxy clusters is that the predominant component of the fluid's pressure is thermal pressure from the ICM. While this approach is generally a reasonable approximation, more recent studies of hydrostatic equilibrium in galaxy clusters have indicated that non-thermal pressure support may play a non-trivial role in the dynamics of the cluster [24, 109, 103, 81]. Of particular interest in the field are the influences of turbulent pressure from bulk movements of the ICM [113] and of the magnetic pressure present in the weakly magnetized ICM [49, 116]. Because these sources of pressure are difficult to model in most cases, we assume in this work that the thermal pressure support in our cluster sample is entirely sufficient to provide for HSE. This approximation, while somewhat crude, is well constrained by simulations, which demonstrate that the ICM is typically thermal pressure dominated with non-thermal components making up only about 10% of the pressure [e.g. 138, 47, 104].

If thermal pressure is assumed to be dominant everywhere, we may assume an ideal gas equation of state and obtain the pressure directly from the observed temperature and density:

$$p_g = \frac{\rho_g T_g k_B}{\omega m_p},$$

where m_p is the proton mass, and ω is the mean molecular mass of the ICM, which is typically ~ 0.60 [123]. In this case, the condition for HSE may be written as

$$\nabla\Phi = -\frac{\nabla p_g}{\rho_g} = \frac{-k_B T_g}{m_p \omega}\left[\frac{d\ln(\rho_g)}{dr} + \frac{d\ln(T_g)}{dr}\right] \tag{1.9}$$

In the classical case,

$$\nabla\Phi = \frac{GM_{\rm dyn}(<r)}{r^2} \implies M_{\rm dyn}(<r) = \frac{r^2}{G}\nabla\Phi.$$

More complex models have been developed which take into account, phenomenologically, non-thermal pressure sources; however, the assumption of HSE remains the cornerstone of ICM physics and is the standard approach used to determine the dynamical mass of systems [48, 52].

In addition to furnishing the dynamical mass of a system, hydrostatic equilibrium may also be utilized in reverse to provide the ICM temperature of a cluster given its hydrostatic parameter. This is quite useful because in cases where a MOND paradigm might alter the form of $\Gamma(\rho_g, T_g)$, as this approach can be used to determine the resulting change in the temperature profile and therefore whether the resulting changes are sufficiently close as to fit within the observational constraints. From Equation 1.9, an ODE for the temperature profile may be derived wherein

$$\frac{dT_g}{dr} + \underbrace{\frac{T_g}{\rho_g}\frac{d\rho_g}{dr}}_{T_g\Omega(r)} = \frac{-m_p\omega}{k}\nabla\Phi. \tag{1.10}$$

The equation has the form

$$\frac{dT_g}{dr} + T_g\Omega(r) = \Psi(r),$$

where Ω is the *pressure term* and Ψ is the *acceleration term*. A complete solution of

the temperature equation can be carried out by multiplying by an integrating factor of ρ_g, leading to the solution

$$T(r) = \frac{-m_p\omega}{k}\frac{1}{\rho_g}\int_{r_0}^{r}\rho_g(r')\nabla\Phi(r')dr' + \frac{\rho_g(r_0)}{\rho_g}T_g(r_0), \tag{1.11}$$

where r_0 is a reference radius from which to begin the integration. Because solutions of ODE's like equation 1.11 are unique, the resulting temperature profile $T(r)$ is invariant under changes to r_0 as long as the underlying ρ_g and $\nabla\Phi$ profiles are not altered. In the context of different MONDian paradigms, solution curves for each profile are generically different from those arising from classical paradigms; an effect which is r_0 dependent. Thus, for the sake of consistency, all temperature profiles in this work which are computed using equation 1.11 assume a boundary condition $T(r_{\min}) = T_N(r_{\min})$, where T_N is the temperature of the system in a Newtonian paradigm. This choice presents the most plausible approach as the available data is at its best outward from $r_{\min}$ and therefore any attempt to set the boundary before that radius increases the opportunity for unmodeled asymptotic behavior.

1.3 Summary of Results

The central accomplishment of this work is to illustrate the comprehensive extent of MOND's failures in clusters of galaxies. We show not only that several popular MOND theories are fundamentally inconsistent with the dynamics of galaxy clusters, but also that those inconsistencies are borne by all theories prescribing to the central tenants of the MONDian paradigm. Our findings lay out a roadmap for a set of comprehensive tests in galaxy clusters which must be passed by any MOND paradigm seeking progressivity. Chapter 3 presents the core of our findings; laying out strict constraints on the popular MOND extensions MOND+DM (section 3.1) and EMOND (section 3.2). To complement the results of chapter 3 (which are predi-

cated on equilibrated systems), we present (chapter 4) some early results in our work on non-equilibrium constraints of MOND. Our work in this regard leads to several, *a priori*, unexplored dynamical results predicted by MONDian gravity.

In the process of developing the main results of this work, several additional contributions to the literature are discussed. Chief among these are the `cluster_generator` code (briefly summarized in section 2.3) and its extended capabilities regarding MONDian gravity and correction of non-physical properties (appendix A). The extended capability of this software, as developed for this work, will enable deeper exploration of MONDian galaxy clusters through numerical simulation. Our work in this regard is ongoing.

Chapter 2

Modeling Galaxy Clusters

2.1 Introduction

With the intention of validating / refuting modified gravity in galaxy clusters, but is critical that we are able to construct reasonable models of these systems. In a generic sense, the implications of any modified gravity paradigm rely directly on our interpretation of their underlying physics from within the current paradigm. In the case of galaxy clusters, three broad areas of concern arise in regard to our theoretical understanding: geometry, microphysics, and gravity. It is our purpose to understand better galaxy clusters as tools for constraining gravity, which, in turn, requires that the other theoretical aspects be strongly constrained. As is the case in many areas of astronomy, galaxy clusters are optically thin and therefore are observed in projection along the observer's line of sight. The resulting image and subsequent analysis of the system is generally interested in reconstructing the underlying 3D system; however, this process is complicated by its reliance on an assumed geometry. In constructing models of these systems, it therefore becomes essential to have constraints which are able to reduce this geometric degeneracy.

In a similar vein, the majority of information available from observations of galaxy

clusters is extrapolated from the emission of the gaseous and stellar components of the system and thus requires a strong grasp of the requisite science. As will be discussed in the following section, the microphysics of the ICM plays a key role in driving a variety of processes in galaxy clusters and is therefore a critical aspect of any model.

In this chapter, we describe the relevant theoretical background from which our models of galaxy cluster dynamics are generated and formulate our methodology for their generation. The remaining sections are laid out as follows: In section 2.2, the relevant literature regarding the physics of galaxy clusters will be explored. Section 2.3 will then build upon this underlying theory in describing our prescription for idealized models of galaxy clusters. Finally, section 2.4 will describe the general process of matching models to observational data and will characterize the cluster sample used in this work.

2.2 Clusters As We See Them

The fundamental properties of galaxy clusters have already been introduced in section 1.2.2, thus we do not reiterate them here; however, several further details of galaxy cluster dynamics remain which play central roles in our construction of idealized models. As the largest dynamically bound systems in the observable universe, galaxy clusters typically span regions on the order of 5-10 Mpc and are X-ray bright in regions of $\approx$ 1Mpc. The large size of these systems, coupled with the relatively diffuse nature of their stellar mass renders their stellar component effectively collision-less with relaxation times on the order of the age of the universe. A similar treatment describes the dark matter halo in which the cluster is embedded because of the necessarily small self-interaction cross-section of the dark matter component.

As has been previously mentioned, the majority of baryonic mass in galaxy clusters is attributed to the intracluster medium (ICM), which is a highly diffuse plasma

largely composed of ionized hydrogen and helium. Because the ICM is the primary observable component of galaxy clusters, and the one from which the most information can be obtained, it is worthwhile to further develop the details of its dynamics.

As was described in section 1.2.2, the ICM in relaxed galaxy clusters is supported against gravitational collapse by its own pressure. Generally, it is acceptable to treat the thermal pressure of the ICM as the only significant pressure component[24, 47, 52]; thus arriving at the equations of hydrostatic equilibrium as they were previously presented. Despite being the ubiquitous choice for its convenience, the assumption of a purely thermal pressure is not an entirely accurate picture. Radio observations of galaxy clusters have revealed synchrotron radiation in the form of radio relics and radio halos / mini-halos; indicating the presence of μG strength magnetic fields in the ICM [e.g. 50, 136, 136, 51, 6]. As a result, magnetic pressure support for the ICM plasma is a non-trivial component of the cluster dynamics. With the addition of a magnetic component, the ICM pressure takes the form

$$p_{\rm ICM} = p_{\rm ICM,therm} + p_{\rm ICM,\mathbf{B}} = p_{\rm ICM,therm} + \frac{B^2}{8\pi}. \tag{2.1}$$

The constraints on the magnetic pressure ratio, $\beta_{\rm magnetic} = p_{\rm ICM}/p_{\rm ICM,\mathbf{B}}$, are an ongoing area of inquiry; however, Faraday rotation measurements (e.g. Bonafede et al. [25] and Vogt and Enßlin [143]) indicate $\beta \approx 100$ in many clusters. Cosmological simulations further affirm this constraint; however, they also indicate that the magnetic pressure should be considerably larger than $\beta = 100$ in the cores of massive galaxy clusters [87]. Figure 2.2 shows the evolution of β as a function of halo radius in the IllustrisTNG simulations. It is clear from examination that these simulations suggest $\beta \sim 1$ near the core of such clusters; indicating that thermal and magnetic pressures should be comensurate on those scales.

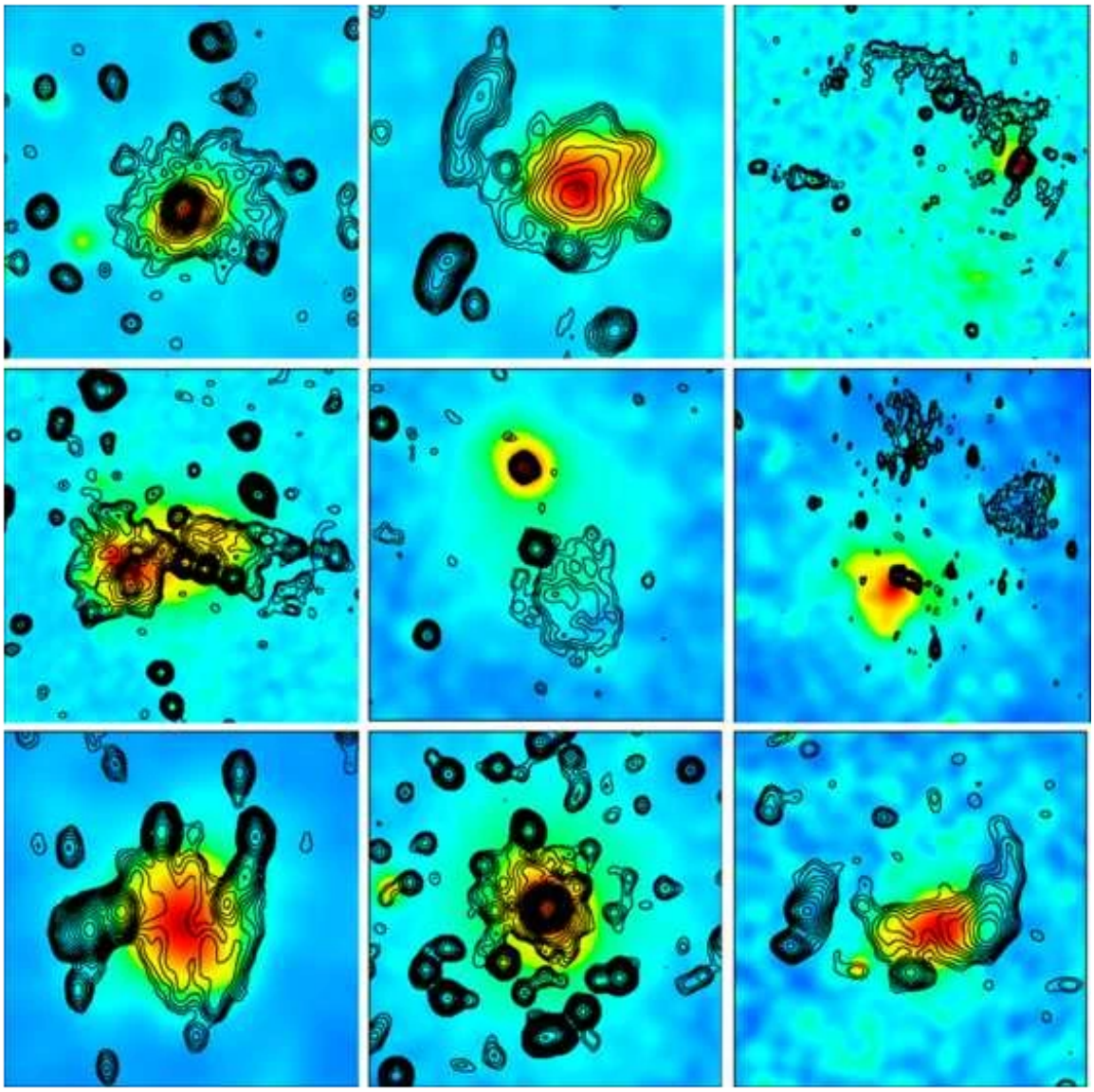

Figure 2.1: Collection of clusters showing several types of radio emission, shown in contours, overlaid onto the X-ray emission, shown in colors. Clusters are (from left to right and from top to bottom) A 2219 (halo), A 2744 (halo + relic), A 115 (relic), A 754 (complex, halo plus relic), A 1664 (relic), A 548b (relic), A 520 (halo), A 2029 (mini-halo), RXCJ1314.4-2515 (halo plus double relics). Figure adapted from Feretti et al. [50].

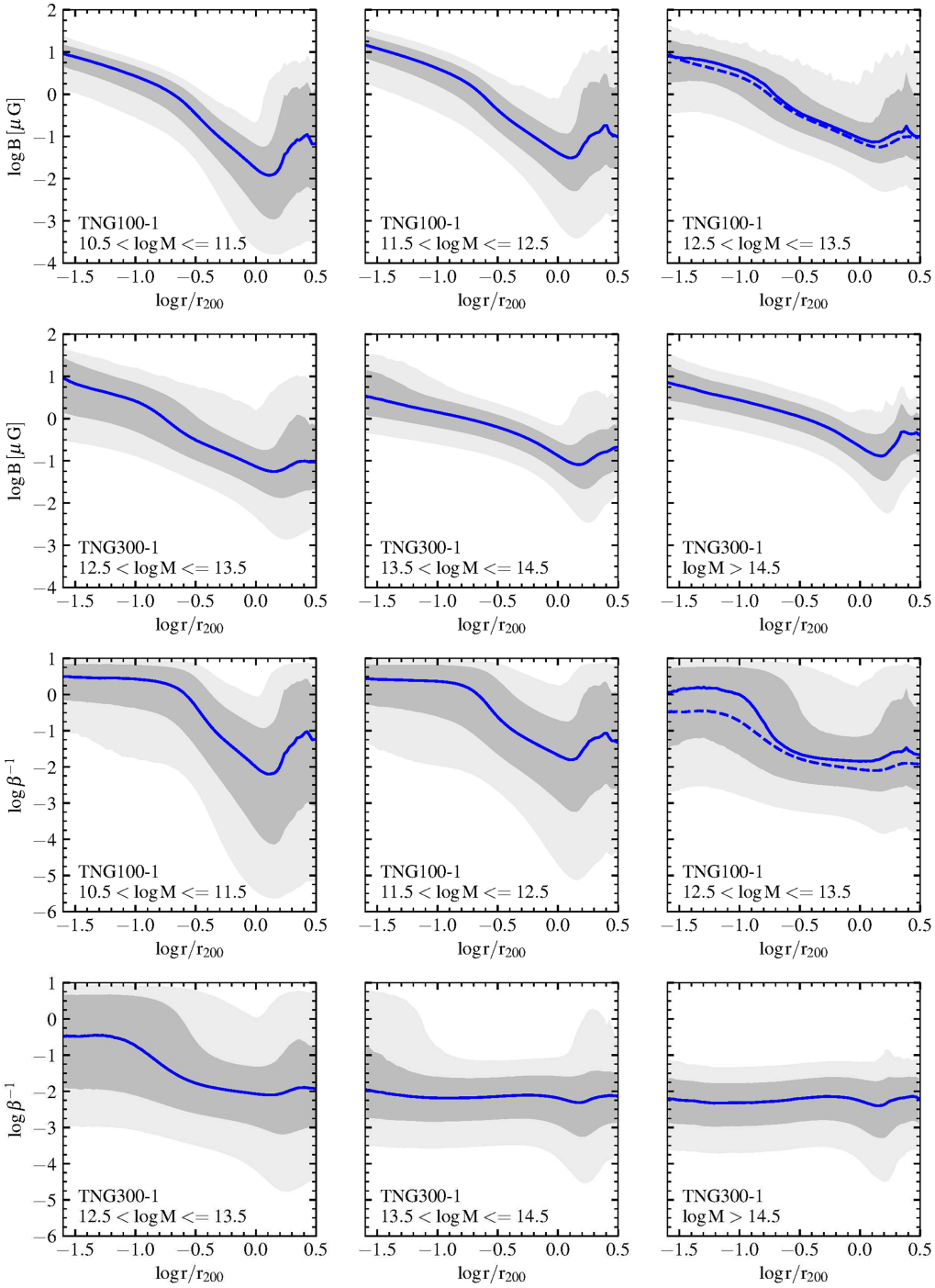

Figure 2.2: Top six panels: Radial magnetic field intensity profiles at redshift zero. The figure presents the stacked profiles of the FOF groups in the virial mass bins indicated in each panel for the IllustrisTNG simulations. The solid blue line represents the (mass-weighted) median trend while the dark and light grey regions show the 1σ and 2σ spread around the median value, respectively. Bottom six panels: Radial profiles of β at redshift zero. To facilitate the comparison in the overlapping mass bins, we report the median relation for the TNG300 run in the TNG100 results as a blue dashed line. Adapted from Marinacci et al. [87].

In addition to magnetic pressure sources, bulk motion of the ICM also complicates the picture of hydrostatic equilibrium in galaxy clusters. In the context of the ubiquitous hierarchical structure formation paradigm [23, 131, 62], galaxy clusters are formed by the sequential mergers of overdensities in the universe. These mergers differ in their phenomenology from major mergers of individually large galaxy clusters to the continuous accretion of material from the cosmic web. Regardless of the exact nature of the formation, the merger history of galaxy clusters is "imprinted" in their bulk motions and turbulence. The modeling of these effects is sophisticated, and largely based on the findings of numerical simulations (see for example Vazza et al. [137]); however, there is broad support in the literature for non-thermal pressure (bulk/turbulent motion and magnetic field) on the order of 10% [138, 46, 124, 20]. One therefore arrives at the approximate heuristic for non-thermal pressure support in clusters of galaxies: $\approx 10\%$ from turbulence, $\approx 1\%$ from magnetic fields.

Compounding on the influence of non-thermal effects, projection effects are also a key source of systematics in observations of galaxy clusters. Because galaxy clusters are optically thin in the X-ray, the surface brightness profile ($\Sigma(r)$) corresponds to the 3D intensity distribution $I(R)$ such that

$$\Sigma(r) = \int_{-\infty}^{\infty} I(\sqrt{r^2 + x^2})dx, \tag{2.2}$$

where x is the line-of-sight coordinate. In special cases where I exhibits cylindrical symmetry, this *projection operator* is equivalent to the Abel transformation and can, given some reasonable assumptions, be inverted to recover the 3D profile. When I does not exhibit such symmetry, it is not possible to regain the information lost by the projection effect. For this reason, it is generally assumed that galaxy clusters are spherical; however, this assumption is not always well founded[56, 83]. Because galaxy clusters are formed through cosmic time by sequential mergers of smaller subhalos,

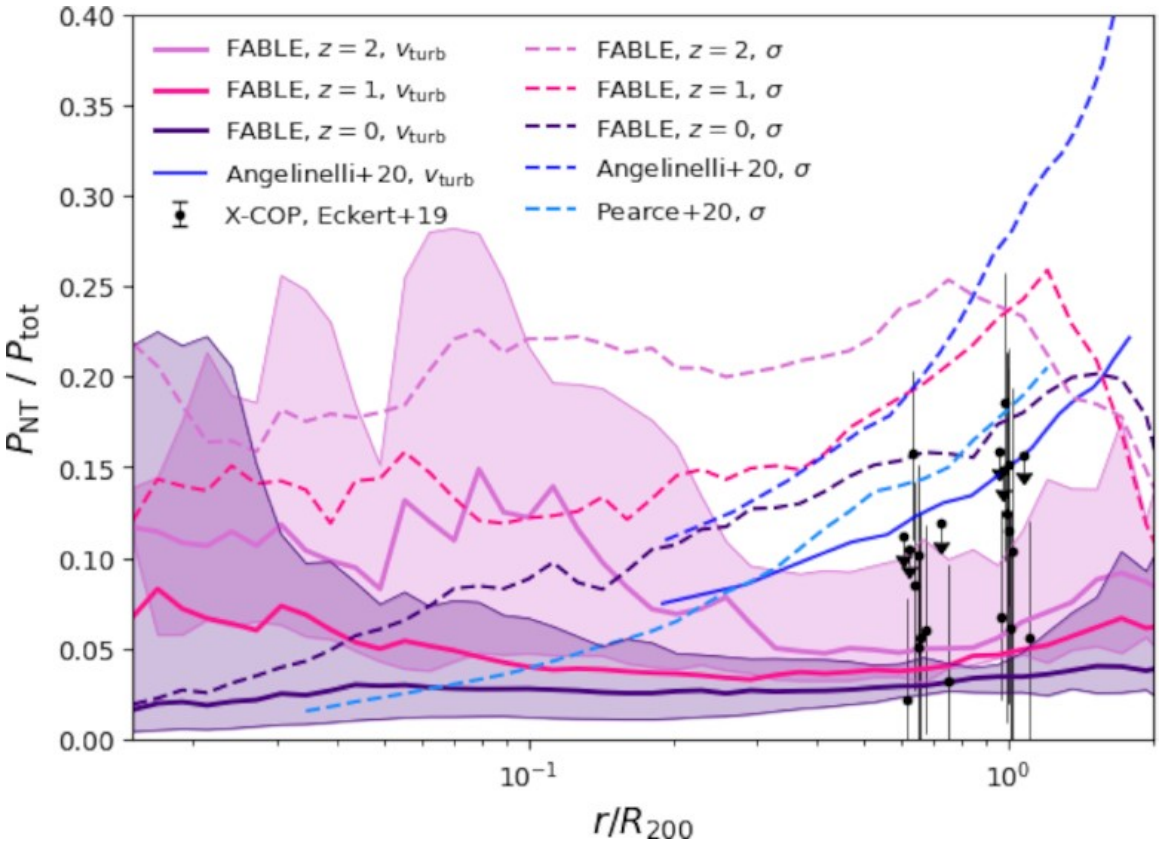

Figure 2.3: Radial profiles of non-thermal pressure fraction, P_{NT}/P_{tot}. Solid lines show profiles calculated using turbulent velocities, and dashed lines show profiles calculated with velocity dispersions (see Section 2.4). Purple/pink lines show the profiles for FABLE at z = 0, 1, and 2, with shaded regions showing the 10–90th percentile scatter in the v_{turb} derived profiles at z = 0 and z = 2. Black dots show observational results from X-COP (Eckert et al. 2019). Dark blue lines show results from z = 0 in the simulations of Angelinelli et al. (2020) (though we note vturb has not necessarily been calculated in the same way). In light blue, we show representative z = 0 data from Pearce et al. (2020). Adapted from Bennett and Sijacki [20].

one would only expect those clusters with negligible persistent rotation and with a significant relaxation time since the last major merger to be spherical. Because galaxy clusters are generically formed by these random mergers, the statistics of their gross rotation should center on $\langle v_{\rm rot} \rangle = 0$. This intuition is supported in the literature [86, 135]; which finds only a small percentage of relaxed clusters retain any measurable rotation. Those which do have rotational velocities on the order $\sim 0.1\sigma_v$, indicating that persistent rotation is unlikely to bias cluster ellipticity. The issue of recent mergers is more dire: many observed galaxy clusters show clear evidence of dynamical activity. Methods to constrain the precise shape of clusters or their

pre-merger progenitors is difficult and we therefore typically rely on statistical bias corrections obtained from simulation.

2.3 Idealized Models

Having now established the most important dynamical details of galaxy clusters, we may begin the critical task of describing the framework from which this work produces the idealized models used in the remaining chapters. In this work, we have constrained ourselves to the discussion of only a relatively simple class of idealized clusters for which the issues of the preceding section are not of concern. We assume that our galaxy cluster models are spherically symmetric, dynamically relaxed, and in hydrostatic equilibrium. In the final subsection of our description of the modeling techniques used, we provide a short introduction to our continuing work on more complex models. The primary intent of this section is to describe the `cluster_generator`[1] package: a python based software package for the generation of idealized galaxy clusters for use in magnetohydrodynamic simulation. The `cluster_generator` package was developed by John ZuHone, with collaboration from the author; a comprehensive account of the methodologies, validation, and usage of the package is in development. In this work, MOND specific capabilities for `cluster_generator`[2] were developed and are undergoing review for subsequent merger with the main codebase.

2.3.1 Cluster Modeling: Baseline

To create idealized models of galaxy clusters, `cluster_generator` exploits hydrostatic equilibrium to produce a self-consistent cluster. Under the simplest assumptions (relaxed, hydrostatic, spherical), only two pieces of information are necessary: one gravitational and the other thermodynamic. Given any cluster property (generi-

[1] https://github.com/jzuhone/cluster_generator
[2] https://github.com/Eliza-Diggins/cluster_generator/tree/pull-request-4

cally a radial profile $g(r)$) from which the potential $\Phi(r)$ might be deduced, one can immediately elucidate the necessary thermodynamic pressure $P(r)$ by insisting on hydrostatic equilibrium. It should be noted by the reader that, in doing so, we have implicitly ignored any sources of non-thermal pressure support. In turn, the thermodynamic pressure is nearly sufficient to provide a complete description of the ICM; however, a degeneracy occurs between pressure, density, and temperature. As such, one must also provide, *a priori*, one of these thermodynamic properties. Because the gas pressure serves as both a thermodynamic and gravitational property, it is also sufficient to provide any two independent thermodynamic properties from which the pressure may be deduced and then used as the gravitational property.

From these two properties, for which we adopt the term *cluster initial conditions* (CICs), all of the remaining thermodynamic and gravitational properties may be deduced. As a typical example of this process, CICs composed of the gas density profile $\rho(r)$ (the thermodynamic property) and the temperature $T(r)$ (the secondary thermodynamic property), the pressure is constructed from the ideal gas law, and the potential is then constructed in quadtrature from the hydrostatic equilibrium equation (equation 1.9). The gas and dark matter components of the mass are then implied by the relevant gravitational framework (Newtonian, AQUAL, etc.) and the computed potential. Because the stellar mass of the cluster contributes very little to the dynamics, it may generally be left out of such models. If one chooses to include it, an additional degeneracy is produced in the gravitational properties and must be resolved by explicitly providing the stellar mass component. A comprehensive diagram of these relationships is provided in figure 2.4.

From the process laid out above, it should be noted that not all potential choices of CICs are actually self-consistent. In fact, it is quite easy to produce galaxy cluster models which imply negative dark matter densities or other non-physical behaviors. When cluster models are generated in an *ad hoc* fashion, this poses no real limitation:

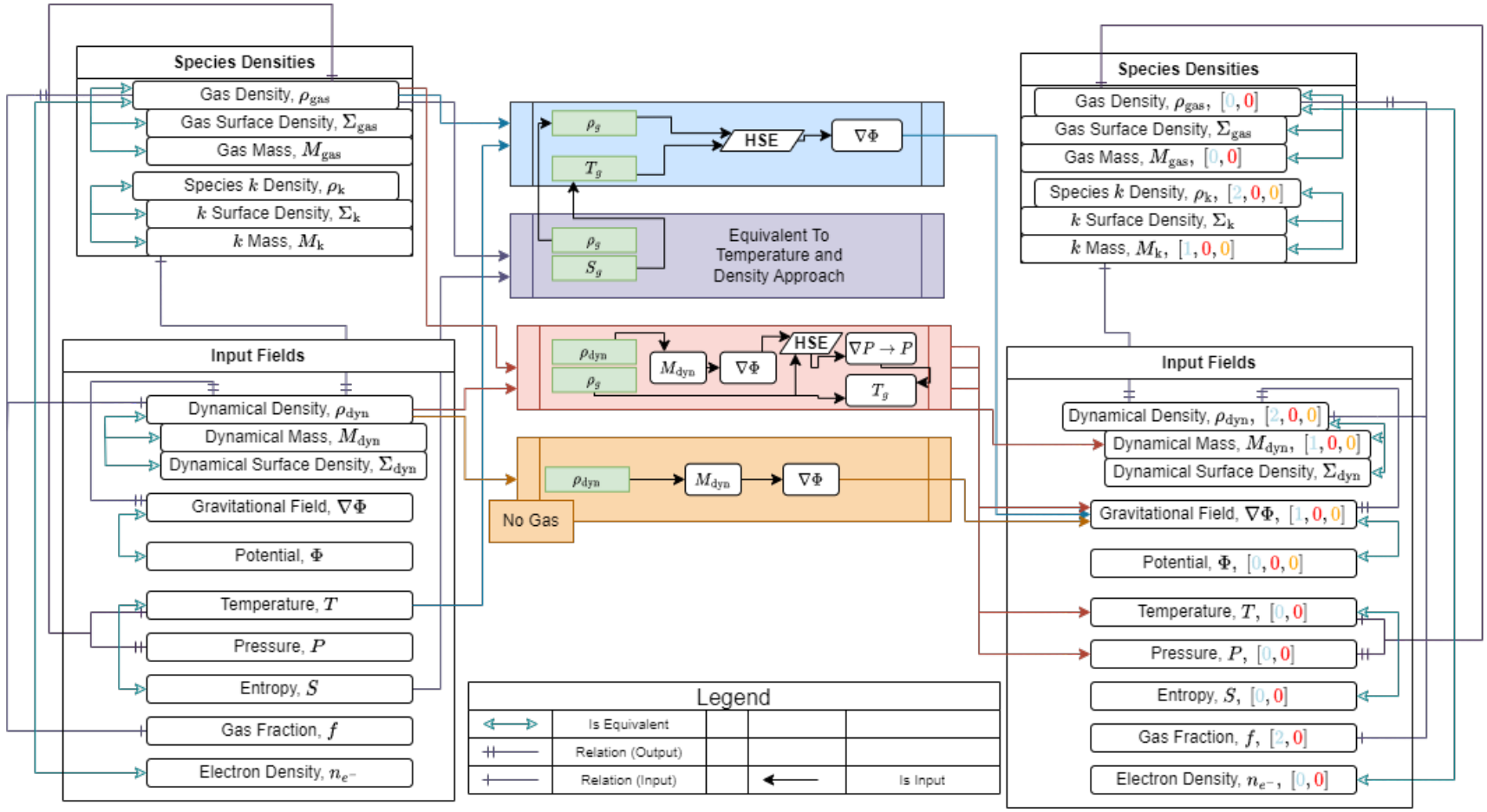

Figure 2.4: A comprehensive diagram of the cluster generation processes used in `cluster_generator`. The left hand column indicates input quantities, the right hand side output quantities. The central column describes the different generation algorithms. Brackets following output quantities show the relative smoothness of the output. If the least smooth input function is $f \in C^n[a, b]$, then an output with a bracketed value k will be $g \in C^{n-k}[a, b]$. Values with 0 may be as smooth or more than the input.

non-physical models simply represent non-physical CICs. Cluster models are, however, not always generated on an *ad hoc* basis; the CICs may be taken from analysis of real systems such as those of Forman et al. [52] or Eckert et al. [48]. In these cases, it is often convenient to fit X-ray data to profiles which can be inconsistent. The parameter space on which these inconsistencies occurs is increased when non-Newtonian gravitational paradigms are also brought into play. To combat these faults, we have established a novel algorithm for non-physical correction summarized in appendix A.

2.4 The Cluster Sample

In this work, we utilize a set of 13 relaxed galaxy clusters at low redshift observed by *CHANDRA*. For each cluster, Forman et al. [52] produced analytical models of cluster gas density based on matching a projected, smooth, 3D model to the observed X-ray surface brightness. A similar process was used to fit a 3D temperature model to the observed X-ray spectra on radial annuli. For a full recounting of the analysis process incorporated, see Forman et al. [52]. Density profiles were chosen in relation to the observed X-ray brightness, which, in turn, is proportional to the product of the ion and electron number densities, $n_p n_e$. The models chosen were of the form

$$\begin{aligned} n_e n_p(r) =& n_0^2 \frac{(r/r_c)^{-\alpha}}{(1+(r/r_s)^2)^{3\beta-\alpha/2}} \frac{1}{(1+(r/r_s)^\gamma)^{\epsilon/\gamma}} \\ &+ \frac{n_0^2}{(1+(r/r_{c2})^2)^{3\beta_2}}. \end{aligned} \tag{2.3}$$

This model expands on the classic β-model [35] by allowing for a cuspy core instead of the flat core of the original model and also allowing the density to steepen at radii beyond $0.3r_{200}$, allowing for a successful fit to a large range of cluster phenomenologies. The gas density of the ICM is related to the emissivity measure by the relation $\rho_g(r) \approx 1.252 m_p \sqrt{n_e n_p}$.

In a similar ilk, the model chosen for the ICM temperatures took the form

$$T(r) = T_0 \frac{(r/r_{\rm cool}) + (T_{\rm min}/T_0)}{(r/r_{\rm cool})^{a_{\rm cool}} - 1} \frac{(r/r_t)^{-a}}{((r/r_t)^b + 1)^{c/b}}, \tag{2.4}$$

which allows for a very general class of temperature profile fits. The relevant best fit parameters which were used for each of these profiles in our analysis of the cluster sample are provided in Forman et al. [52].

For each cluster, $r_{\rm min}$ were specified at which the cluster profiles were truncated due to a variety of factors, predominantly low fit quality in the inner regions of clusters. The authors suggest that this is due to emergent multi-phase characteristics of the ICM in the inner region, as well as observable sub-structures within the cluster centers. We follow these prescriptions for each cluster echoing Forman et al. [52] in that our interest in these clusters is largely focused on the outer regions of the observed cluster and therefore fits in the central annuli are not strictly necessary.

The presumed hydrostatic nature of the ICM provides a critical link between the gravitational phenomena being studied and the better constrained baryonic physics observed in galaxy clusters. In the remainder of this work, the core of our analysis focuses on exploiting this link in a variety of gravitational paradigms in search of inconsistency. In any potential paradigm, the gas density ρ and the gas temperature T will clearly be invariant (they are each constrained by observation); however, the other free parameters of the system may be forced to adjust to accommodate this requirement in a new paradigm. To assure legible notation, we adopt the convention that variables consistent with a Newtonian paradigm are labeled with $\tilde{\cdot}$ and those which are associated with the non-Newtonian paradigm are labeled without. Thus, only ρ and T are assured to have the property that $\rho = \tilde{\rho}$ and $T = \tilde{T}$.

Chapter 3

Constraining MOND Extensions

3.1 MOND+DM

One proposed modification to eliminate MOND's faults in galaxy clusters is the inclusion of an additional (collisionless) massive component which, in principle, could provide the remainder of the apparent missing mass. The exact nature of this additional component varies from theory to theory; however, popular candidates include sterile neutrinos with masses $m_\nu \approx 11$ eV [9, 10], and cold gas content, which would not necessarily be detectable [97]. In either case, the inclusion of such a component is not particularly enticing; however, it remains worthwhile to test such a possibility.

Consider a galaxy cluster with some observed ρ_g, T_g and an inferred (Newtonian) $\tilde{M}_{\rm dyn}(< r)$. For an alternative theory of gravity to be suitable, there must exist some possible cluster in said paradigm which implies the same ρ_g and T_g. In the MOND+DM paradigm, this clearly becomes a question whether there exists a suitable "phantom" mass distribution $M_{\rm phantom}$ which preserves ρ_g and T_g while also eliminating the missing mass problem. Given that ρ_g and T_g are preserved, $\nabla\Phi$ must

also be invariant between paradigms. By equation 1.3,

$$M_{\rm dyn} = \tilde{M}_{\rm dyn}\mu\left(\frac{|\nabla\Phi|}{a_0}\right),$$

where $M_{\rm dyn}$ is the "dynamical" or gravitational mass of the system. The resulting "phantom mass" necessary to reproduce the MOND dynamical mass is

$$M_{\rm phantom}(<r) = \underbrace{\tilde{M}_{\rm dyn}(<r)\mu\left(\frac{|\nabla\Phi|}{a_0}\right)}_{M_{\rm dyn}(<r)} - M_{\rm g}(<r), \tag{3.1}$$

In the DMR ($a \ll a_0$), $\mu(x) \approx x$ and

$$M_{\rm phantom} \approx \frac{|\mathbf{a}(r)|}{a_0}\tilde{M}(<r) - M_{\rm g}(<r).$$

Clearly, if

$$|a(r)|/a_0 \leq M_{\rm g}/\tilde{M}_{\rm dyn}, \tag{3.2}$$

then the necessary phantom mass in non-positive and the cluster becomes inconsistent. This seemingly innocuous result immediately implies severe constraints on the nature of any MOND+DM paradigm.

As was discussed in section 1.2.2, hydrostatic equilibrium is not unilaterally applicable across the entire domain of a cluster; furthermore, observations only constrain ρ_g and T_g to within a (finite) error bound. Together, these two caveats to the idealized case presented suggest that MOND+DM type paradigms might yet escape constraint on the basis that either uncertainty in the relevant profiles or lack of true hydrostatic equilibrium could render moot any inconsistencies in our theoretical predictions. To contend with this possibility, it is worth considering at what characteristic radius of a given cluster such inconsistencies might arise.

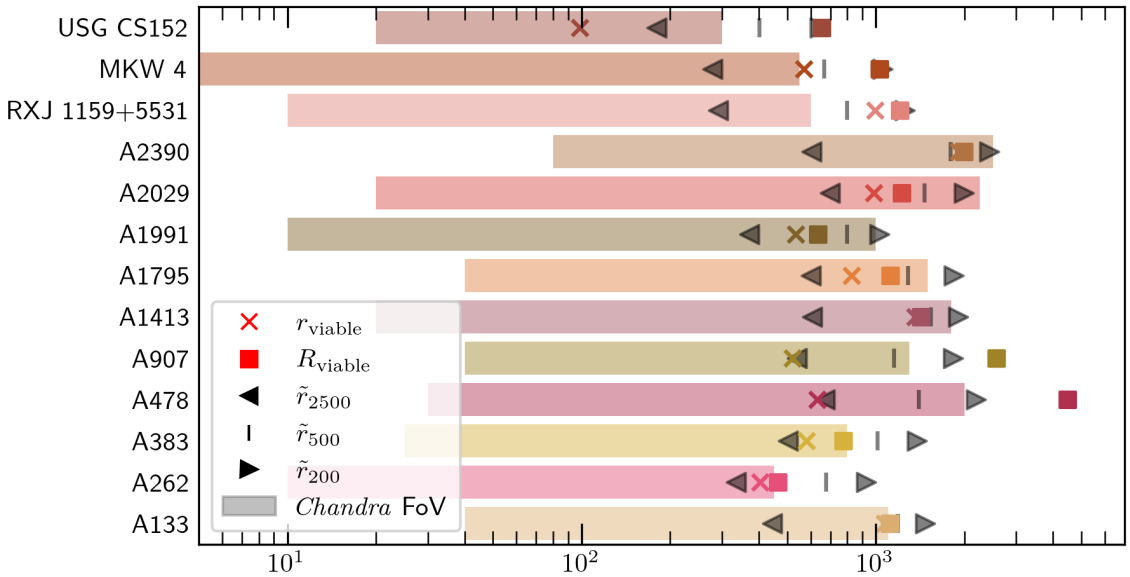

Figure 3.1: Calculated values of $r_{\rm viable}$ and $R_{\rm viable}$ for each of the clusters in our sample. Overdensity radii were computed assuming a Plank18 cosmology [111]. Background shading represents the *Chandra* field of view for each of the clusters presented as described in Forman et al. [52]. Notably, inner boundaries were determined by the radius of the smallest annulus used for the temperature map and the outer boundary corresponds to detected X-ray brightness at $> 3\sigma$. In all but 2 cases (A2390, RXJ1159+5531), observed viability radii, $r_{\rm viable}$ were within r_{500}.

Inequality 3.5 implies that any idealized model of an observed cluster will have some r_{viable} after which the idealized system must bring on physical inconsistency; furthermore, the inequality may be strengthened by recognizing that $\partial_r M_{\rm phantom} > 0$ for all radii. Thus, $r_{\rm viable}$ is the first radius for which this is untrue. To characterize this transition we must consider more rigorously the best case upper bound, which we refer to as the *maximal viable radius* and denote $R_{\rm viable}$; Appendix B.1 explores the derivation of the below two results, but for the sake of brevity, they are presented here without justification:

1. In the general case of arbitrary $\mu(x)$,

$$\partial_r \tilde{M}_{\rm dyn}(< r)\left\{\mu(\gamma) + \gamma\partial_\gamma\mu(\gamma)\right\} - \frac{2\gamma}{r}\tilde{M}_{\rm dyn}(< r)\mu(\gamma) \geq \partial_r M_{\rm bar}(< r), \quad (3.3)$$

where γ is the *relative acceleration* parameter

$$\gamma = \frac{G\tilde{M}_{\rm dyn}(< r)}{r^2 a_0}.$$

It should be noted that this criterion is *entirely determined by the Newtonian equivalent system.*

2. If one assumes an amenable form for μ such that $\mu(x) = x/(1+x^\alpha)^{1/\alpha}$, where $\alpha \in \mathbb{N}$ (a common choice in the literature[72, 16]), then *at best*, an idealized cluster remains physical so long as

$$\frac{d\ln(\tilde{M}_{\rm dyn})}{dr} \geq \frac{1}{r\left(\gamma^\alpha + 1\right)}. \tag{3.4}$$

In this special case, two phenomenologies arise dependent on γ. If $\gamma > 1$, then one can always select an α for which the denominator on the RHS of inequality 3.4 is sufficiently large to satisfy the inequality at arbitrary radius. It should be noted that $\gamma > 1$ implies that the system remains within the Newtonian regime, even in MONDian gravity. If $\gamma < 1$, corresponding to the onset of MOND behavior, then the smallest RHS for a given r is that for which $\alpha = 1$, so

$$\frac{d\ln(\tilde{M}_{\rm dyn})}{dr} \geq \frac{1}{r(\gamma+1)} \Leftarrow \rho \geq \frac{\langle\tilde{\rho}_{\rm dyn}\rangle_r}{6}, \tag{3.5}$$

where $\langle\tilde{\rho}_{\rm dyn}\rangle_r$ is the average density over the entire cluster within a radius r.

Cluster models with best-case viability bounds dictated by $\gamma > 1$ are said to have "Newtonian type viability" (NTV). Likewise, those with viability bounds dictated by $\gamma \leq 1$are said to posses "MONDian type viability" (MTV).

As a more general exploration of these constraints, figure 3.2 illustrates the maximal viable radii of a Monte-Carlo simulation of $N = 20,000$ NFW profiles represent-

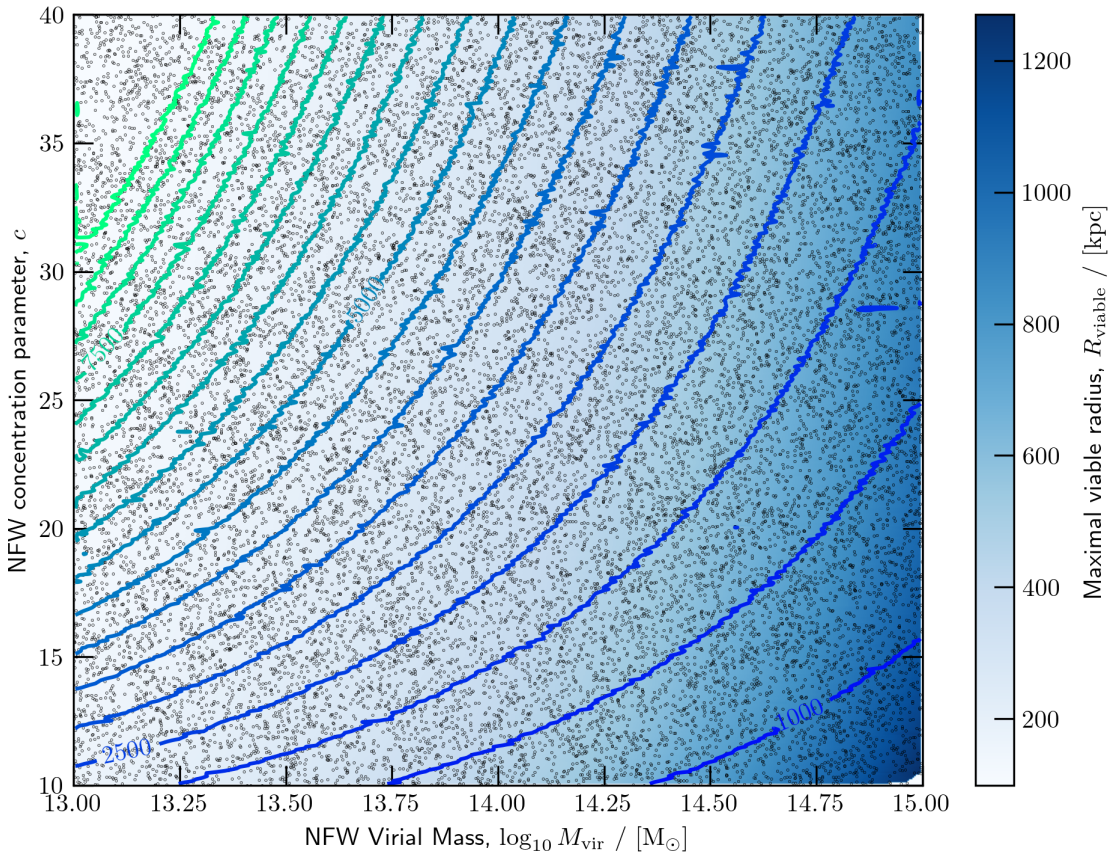

Figure 3.2: Characteristic viability of galaxy clusters (as modeled by NFW profiles) in the MOND+DM paradigm. Data was produced by Monte Carlo simulation, calculating $R_{\rm viable}$ on set set of $N = 20,000$ randomly sampled NFW profiles. Profiles were constructed from their virial mass ($10^{13} - 10^{15}$M$_\odot$) and concentration parameter ($10 - 40$), and the maximal viable radius $R_{\rm viable}$ (image) was computed as well as the corresponding over-density at that radius (contours). Data was interpolated using the cubic Bezier scheme of Alfeld [7] as implemented in the `SciPy` package [140].

ing a comprehensive parameter space of galaxy clusters as observed in the context of ΛCDM. Because the constraints illustrated above are reliant only on the properties of the corresponding Newtonian system; when applied to these NFW profiles, maximal viable radii within a presumed observational region of the cluster correspond to (theoretically) observable deviations in the temperature and density profiles.

In suitable clusters, the results illustrated above suggest that the contradictory behavior of the phantom mass profile can happen well within regions of the cluster for which hydrostatic equilibrium is a reasonable assumption; however, little has yet been said about what this constraint would imply observationally. Thus far, our arguments

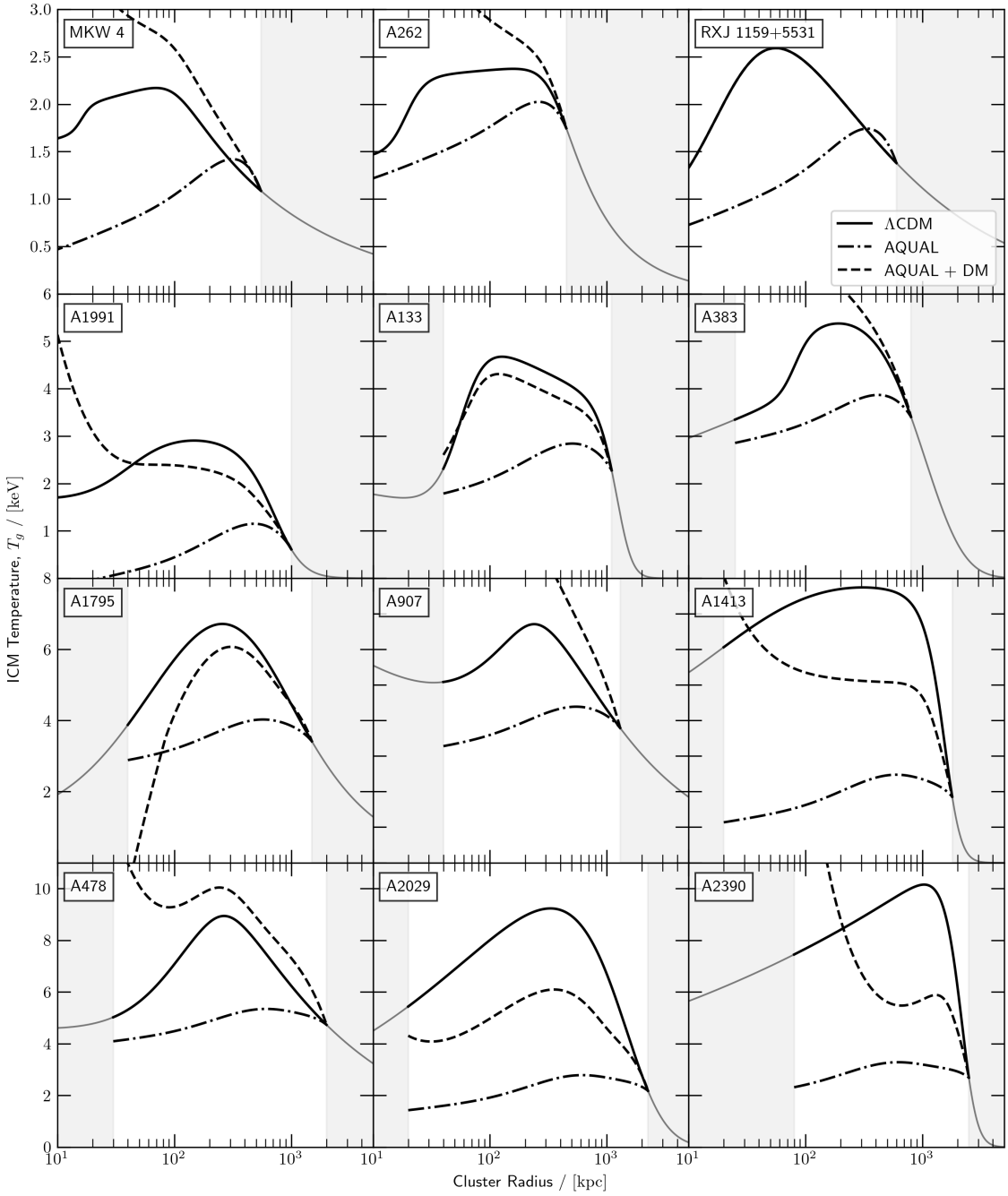

Figure 3.3: Calculated temperature profiles for each of the galaxy clusters in the sample. Temperature profiles were computed in a pure AQUAL framework (wherein only the ICM is present) as well as an AQUAL+DM framework which includes a phantom mass component. In cases where the AQUAL and AQUAL+DM paradigms led to physical inconsistencies, the "minimal" correction approach was used to produce the best (physically viable) approximation to the original. In all but 1 cluster (RXJ 1159+5531), the necessary corrections were sufficient to force significant deviation in the resultant temperature profile. It should be noted that RXJ 1159+5531 and USG CS152 (excluded for plot spacing) are the only clusters in our sample which have R_{viable} outside of the *Chandra* field of view and therefore did not require any correction on that domain.

have relied only on the hydrostatic assumption, particularly that $\nabla\Phi = \nabla\tilde{\Phi}$; however, a more physically illustrative version of the same argument may be obtained instead by explicit examination of equation 1.9. If one assumes that (over some region of interest), $\rho_g \propto r^{\alpha}$ and $T_g \propto r^{\beta}$, then $\nabla\Phi \propto r^{\beta-1}$. Furthermore, Newtonian dynamics would imply that $M_{\rm dyn} \propto r^{\beta+1}$. Thus, for the dynamical mass to be stable, $\beta = -1$ for large r. From the perspective of MOND,

$$M_{\rm dyn} = \tilde{M}_{\rm dyn}\mu\left(\frac{|\nabla\Phi|}{a_0}\right) \propto r^{2\beta}$$

for r sufficient to treat $\mu(x) \approx x$. For the dynamical mass to be stable in a MONDian paradigm, $\beta = 0$ for large r. Thus, the constraints described in this section should emerge in an observational sense from the asymptotic behavior of the relevant temperature profiles. More generally, it is possible to explore the emergence of inconsistency by "correcting" MONDian systems so as to produce a self-consistent system which is minimally different from the equivalent system in the Newtonian paradigm. If the resulting deviations in the temperature profile are sufficiently large and appear at sufficiently low radii, it should be possible to comprehensively refute the MOND+DM paradigm in galaxy clusters. To that end, we conclude this section by carrying out this "correction" on the sample of cluster models described in section 2.4. Corrections are performed on the basis of equation 3.1; first, the implied (potentially inconsistent) dynamical and phantom mass profiles are produced using the known ρ_g and T_g profiles . To correct the emergent inconsistencies, $\rho_{\rm dyn} \rightarrow \rho'_{\rm dyn}$ where $\rho'_{\rm dyn}$ is everywhere $\geq \rho_g$ and therefore implies $\rho_{\rm phantom} \geq 0$. There is no guarantee that such a correction produces a "smooth" $\rho'_{\rm dyn}$; however, all other correction procedures, which might be more physical, create a larger deviation in the underlying profiles. As such, we refer to this approach as "minimum" correction and conclude that other correction approach will only exacerbate our findings. Further discussion

on correction procedures can be found in Appendix A.

Once the corrected ρ'_{dyn} has be produced, the temperature may be recalculated directly from equation 1.11. Because the gravitational field will generally be changed by correction, the solution curves of the temperature equation are no longer independent of the boundary condition. As such, we adopt the convention that $r_0 = r_{3\sigma}$ (the boundary of the *Chandra* field of view) and

$$T(r) = \frac{m_p \omega}{k \rho_g} \int_r^{r_0} \rho_g(\xi) \nabla \Phi(\xi) d\xi + T_0$$

where T_0 is the fixed temperature of the cluster at r_0 regardless of the theoretical framework.

The computed temperature profiles are provided in Figure 3.3 and clearly indicate the expected divergence in the MOND+DM approach. Only clusters RXJ1159+5531 and USG CS152 (not shown in figure) display reasonable agreement with the original temperature profile. This observation matches our prediction on the basis of the calculated r_{viable} as figure 3.1 shows that those two clusters are the one ones for which the viability radius is outside of the observable field of view. It is noteworthy that XRISM's Extend instrument should be able to extend the relevant domain of observation, may be capable of increasing the number of clusters for which these deviations are observable and therefore bolster the cluster population on which one could level arguments for or against MOND+DM predicated on this analysis. Furthermore, the cluster sample presented here is by no means a comprehensive set of clusters. A wider study, in the same ilk as this one, might consider a larger set of clusters on which to perform this analysis and considerable expand the candidate clusters for which these deviations are both predicted and observable.

3.2 EMOND

In seeking an explanation for the disparity in MOND's utility between galaxies and clusters of galaxies, it has long been observed that, because of the size of the gravitational well in clusters, MOND phenomenology does not become dominant except in the outskirts of the system, by which point it cannot "catch up" to the necessary dynamical mass. Extended MOND (EMOND) provides an exculpatory mechanism by which to avoid this issue. Instead of mediating the transition between Newtonian and MONDian dynamics at a constant a_0, one instead uses some $A_0(\Phi)$. If $A_0(\Phi)$ is some (presumably increasing) function of Φ, then clusters would have a higher a_0 cutoff than galaxies and thus a larger domain on which MOND phenomenology can occur. A classical lagrangian was introduced in Zhao and Famaey [148], here after ZF12, which does just that:

$$\mathcal{L}_E = \frac{1}{2}\rho v^2 - \rho\Phi - \frac{\Lambda}{8\pi G}\mathcal{F}\left(\frac{|\nabla\Phi|^2}{\Lambda}\right), \quad \Lambda(\Phi) = A_0(\Phi)^2. \tag{3.6}$$

The resulting Poisson Equation takes the form

$$\begin{aligned} 4\pi G\rho =& \nabla\cdot\left[\mu\left(\frac{|\nabla\Phi|}{A_0(\Phi)}\right)\nabla\Phi\right] \\ &\underbrace{-\frac{1}{2}\left|\partial_\Phi\Lambda\right|\left(\frac{|\nabla\Phi|^2}{\Lambda}\mathcal{F}'\left(\frac{|\nabla\Phi|^2}{\Lambda}\right) - \mathcal{F}\left(\frac{|\nabla\Phi|^2}{\Lambda}\right)\right)}_{T_2}. \end{aligned} \tag{3.7}$$

It is shown in ZF12 that the T_2 term is typically quite small, allowing for an approximation which maintains the Gaussian characteristics of the classical Poisson equation,

$$4\pi G\rho \approx \nabla\cdot\left[\mu\left(\frac{|\nabla\Phi|}{A_0(\Phi)}\right)\nabla\Phi\right].$$

By introducing additional freedom, EMOND avoids many of the theoretical pitfalls

present in more established MOND flavours; however, $A_0(\Phi)$ cannot be left entirely unconstrained. While it is generically true that any idealized cluster model has some $A_0(\Phi)$ which would suffice to eliminate the missing mass problem while preserving the temperature and density profiles, one expects that $A_0(\Phi)$ should arise from some more fundamental theory and therefore that $A_0(\Phi)$ should be uniform across different systems. Hodson and Zhao [65] (HZ17) argued that such an $A_0(\Phi)$ was observed in the same collection of galaxy clusters described in section 2.4; however, considerable scatter was present in their findings. To explain the scatter, one must conclude that observations of the system are sufficiently uncertain to allow for such a breadth of difference. To test this assumption, we will present an extension of the work presented in HZ17 to consider the implications of the scatter in $A_0(\Phi)$ and whether it can be described by uncertainty in the underlying profiles.

In the formalism of EMOND, the unique $A_0(\Phi)$ curve for a given idealized cluster is given by

$$A_0(\Phi) = |\nabla\Phi|\chi\left(\frac{\nabla\Psi_b}{\nabla\Phi}\right), \tag{3.8}$$

where $\chi = 1/\mu^{-1}$ and Ψ_b is the *Newtonian* gravitational potential generated by only the baryonic component of the system. Generally, equation 3.8 is a differential equation in Φ; however, by enforcing hydrostatic equilibrium, $\Phi(r)$ may be determined to within a choice of gauge. Furthermore, if Φ is a monotone function of r ($\nabla\Phi > 0$ for all r), then $r = \Phi^{-1}(\Phi(r))$ and $A_0(\Phi)$ may be constructed as a function of the potential without solving the ODE directly.

The gauge freedom implicit in the determination of $A_0(\Phi)$ is a clear weakness of EMOND as there is not a clear line of physical reasoning on which to break the degeneracy. Furthermore, in comparing systems, one needs to be extremely careful about choosing consistent boundary conditions. HZ17 avoided confronting this issue

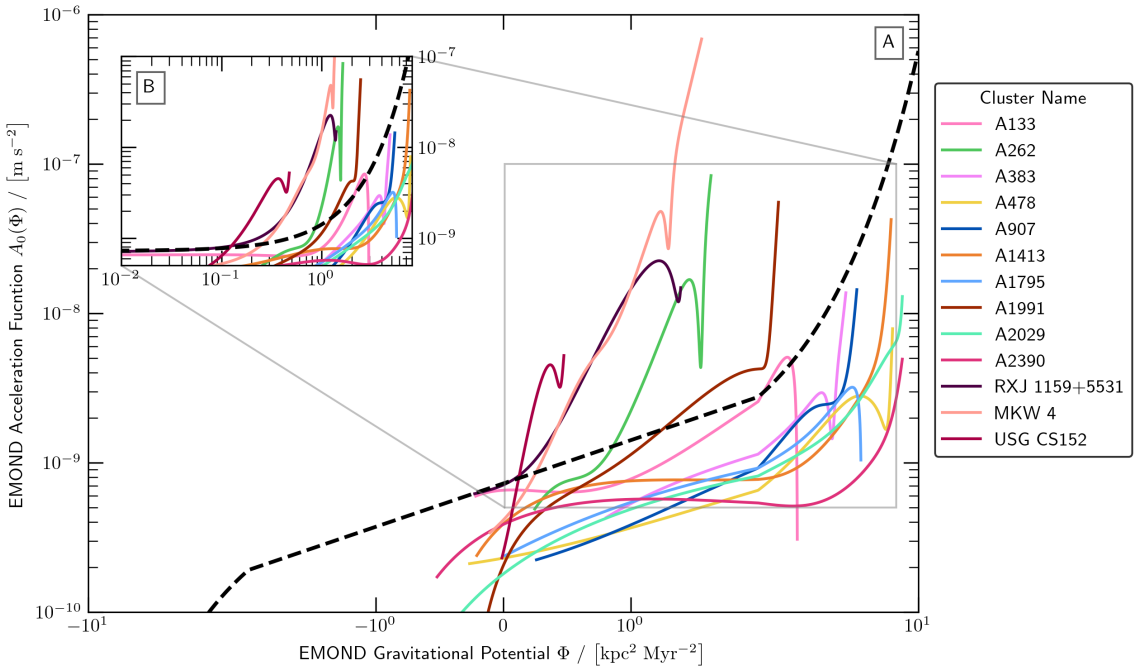

Figure 3.4: Calculated $A_0(\Phi)$ curves for each of the cluster models in our sample. The function $\alpha \exp(\Phi/\Phi_0)$ was fit using a least-squares approach to the calculated curves (black dashed). Panel A shows a symmetrically logarithmic scaling of the calculated $A_0(\Phi)$ curves as they pass through the gauge point at r_{200}. Panel B shows a zoomed version of panel A with standard logarithmic scaling to reduce visual artifacts. It should be noted that many cluster models do not appear to asymptote to the expected a_0 value at low potential and substantial scatter is observed in the best fit curve.

by adopting a boundary at $r_{\text{bound}} = 2r_{200}$ where the boundary value was some constant multiple of the corresponding potential of an NFW profile at that radius. The NFW profiles were produced as fits to the dynamical mass. This approach, while decidedly *ad hoc*, is not entirely without merit. Because the assumption of HSE implies that the gravitational field in the EMOND picture should match that of the ΛCDM picture. Thus (assuming NFW profiles provide a good fit), the corresponding gravitational field of the NFW profile should also correspond to that of the idealized model in an EMOND paradigm. Nonetheless, two points of criticism make the approach insufficient; first, HZ17's NFW fits to the dynamical mass of each system were not particularly good fits, often varying by as much as half an order of magnitude. Secondly, the notion that the *Newtonian* potential computed from each of the NFW profiles would be simply a constant multiple different from the *Mondian* potential is

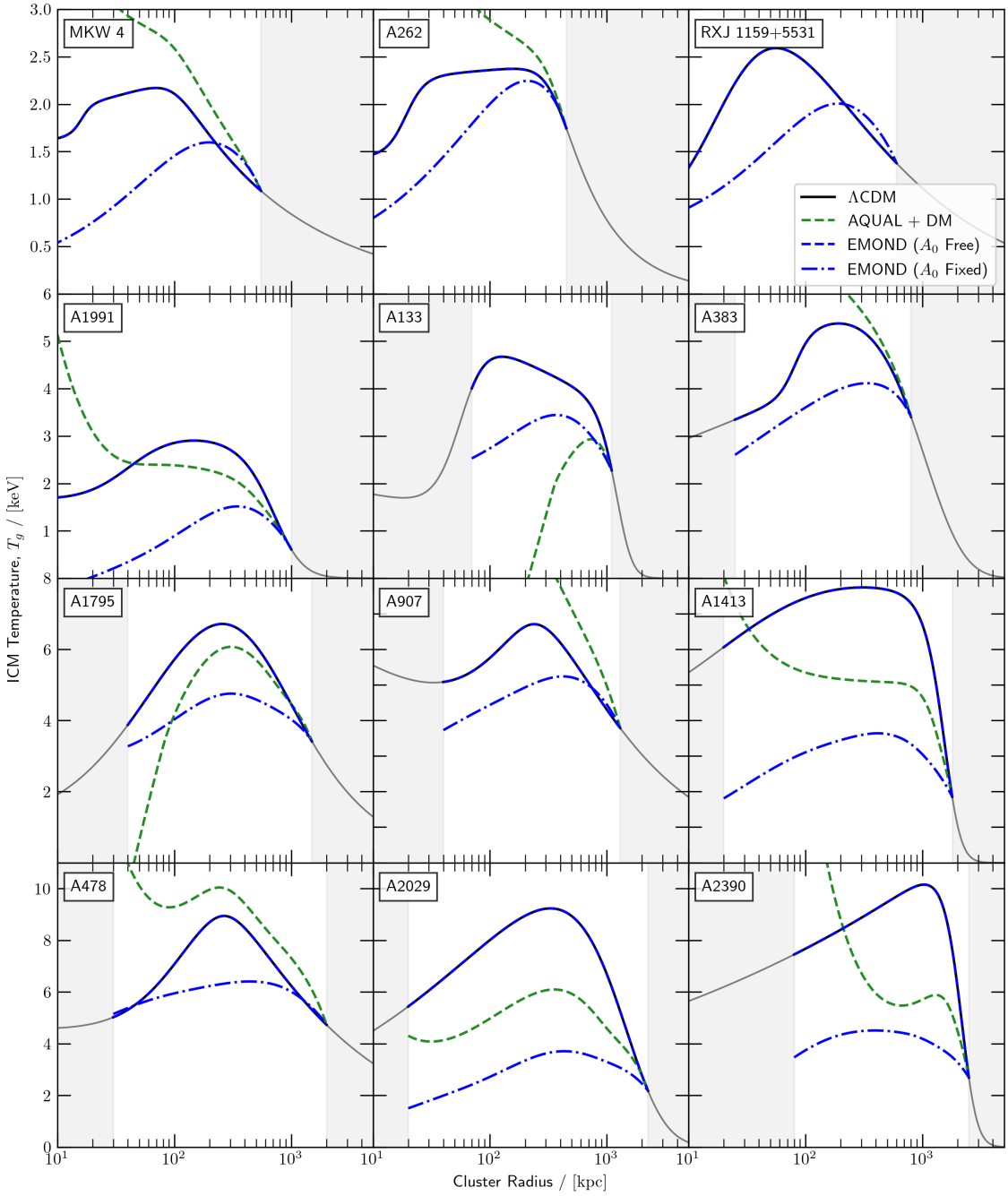

Figure 3.5: Calculated temperature profiles for each of the galaxy clusters in the sample. Temperature profiles were computed in the context of ΛCDM, and EMOND. Two EMOND cases are presented, one for which $A_0(\Phi)$ is free between clusters and one where it is fixed. Additionally, temperature profiles for the AQUAL+DM paradigm are also provided. In cases where the AQUAL+DM paradigms led to physical inconsistencies, the "minimal" correction approach was used to produce the best (physically viable) approximation to the original. In each of the clusters in the sample, EMOND was able to perfectly match temperature profiles when $A_0(\Phi)$ is freed; however, for the best fit model $\mathbf{A}_0(\Phi)$, each cluster showed easily detectable deviation from the observed temperature profile.

not a sound one. HSE implies only that the fields should match but does not endow the two systems with some commensurate gauge. In fact, because the gravitational potential in MONDian dynamics behaves as $\ln(r)$ far away from an isolated system, the suggestion that the NFW gauge at $r = \infty$ is related by any simple prescription to the gauge in a MONDian paradigm is ill-founded. As such, in this work, a different approach will be used.

In this work, we provide an alternate procedure for prescribing the gauge; instead of using NFW fits to the cluster models, we instead use a standardized gauge such that $\Phi(r_{200}) = 0$. The *Chandra* observations underlying our cluster sample are constrained (by X-ray brightness) to an outer radius $r_{3\sigma}$ for each cluster as described previously. Because $r_{3\sigma}$ may be less than the corresponding r_{200}, the following convention is adopted. When a cluster extends as far as r_{200}, its gravitational field is integrated in quadrature and the gauge adjusted to be zero at r_{200}. If r_{200} is outside of the model domain, the cluster is truncated at $r_{3\sigma}$ and the gravitational field is extended (under that truncation) to r_{200} and then integrated in quadrature. The choice to enforce this boundary condition is justified by two observations; first, because the acceleration in MONDian gravity goes as $1/r$ at large radii, the potential is logarithmic and therefore not bounded in the limit as $r \to \infty$. Thus, one *must* enforce a zero point of the potential at some finite radius. As for why to set that zero point at r_{200}, we argue that the potential at that radius represents (to the best extent possible), the "cosmological" background and therefore the closest proxy for a universal gauge. It should also be noted that, when transformed under a change of gravitational gauge $\phi \to \Phi = \phi + \phi_0$, $A_0(\phi) \to A(\Phi - \phi_0)$ with no change in shape. Thus, any observed scatter in the calculated A_0 is, save for a shift in the domain, "frozen" into the data regardless of the choice of gauge. Nonetheless, the reliance of EMOND on a (necessarily *ad hoc*) choice of boundary should be considered with severe skepticism for the entire theoretical framework.

Having established a justification for the selected boundary condition, for each of the clusters in our sample, the corresponding $A_0(\Phi)$ curve was calculated as prescribed above. To minimize the emergence of numerical artifacts, we adopt an interpolation function $\mu(x) = x/(1+x)$ as was done in section 3.1. For this choice of μ, $\chi(x) = (1-x)/x$, and $A_0(\Phi)$ curves may be constructed as described previously. For the clusters in our sample, each had $r_{200} < r_{3\sigma}$ and so no extrapolation was necessary. This is largely because the r_{200} is calculated, in this case, on the basis only of the baryonic component of the model, substantially reducing all of the concentration radii r_Δ. Similar to the findings of HZ17, we do observe a clear correlation in the general shape of the necessary $A_0(\Phi)$ curves; however, several significant differences are apparent. Of primary interest is the fact that the overall range of $A_0(\Phi)$ values calculated in our approach is substantially larger than in HZ17, spanning approximately an order of magnitude greater set of accelerations. In an effort to determine to what degree our approach corresponds to the findings of HZ17, the suggested theoretical form of $A_0(\Phi) = a_0 \exp(\Phi/\Phi_0)$ was fit to our $A_0(\Phi)$ curves. Doing so illustrates one of the serious complications arising for the gauge choice in this framework. Because our choice of gauge does not place the zero point in a region of the cluster where $\nabla\Phi$ is also near zero, the asymptotic behavior of $A_0(\Phi) \to a_0$ as $\Phi \to 0$ is not present in our approach. Given that $A_0(\Phi)$ should arise from some, more fundamental, theory, the fact that change in gravitational gauge can impede upon the asymptotic behavior of the function suggests a serious flaw in the EMOND formalism.

Despite the defects discussed above, the correlation noted in HZ17 is observed; namely that the necessary $A_0(\Phi)$ increases with increasing Φ. As such, we followed there reasoning in fitting a simple model of $A_0(\Phi)$ to the data. In an effort to minimize numerical difficulties, and because of the significant scatter of computed $A_0(\Phi)$, a

simple exponential model was selected in the form

$$\mathbf{A}_0(\Phi) = a_0 \exp((\Phi - \varphi)/\Phi_0).$$

A similar model was used in HZ17; however, we have introduced the parameter φ so as to recover the asymptotic behavior $A_0(\Phi) \approx a_0$ as $\Phi \to \varphi$. Because of the exponential growth of $A_0(\Phi)$, systems with high accelerations and high potentials (neutron stars, black holes, etc.) would potentially be influenced by MOND effects, counter to observation. HZ17 proposed a more physically reasonable option which captures the same behavior as this model in low acceleration regimes. As our purpose here is only in regard to low acceleration systems, we adopt our simple model as sufficiently accurate in the regime of application. Best fit values for φ and Φ_0 were obtained from our cluster model via standard least-squares, yielding values of $\varphi = -2.7\text{kpc}^2\text{Myr}^{-2}$ and $\Phi_0 = 1.5\text{kpc}^2\text{Myr}^{-2}$. The resulting curve is indicated in figure 3.4.

Despite being a reasonably good fit to the clusters, considerable scatter is still observed in the model $A_0(\Phi)$ function. As such, cluster models in the sample were regenerated; this time in the context of the best fit, fixed $A_0(\Phi)$. It is generally possible to do this in two ways: one may either require that the original ρ_g and T_g remain the same or one may require that the dynamical mass be limited to that of the gas. In the first case, EMOND will (in general scenarios) require the addition of a "phantom" mass component. The second case avoids requiring this additional component, but at the cost of changing the temperature. In this work, we present only the later approach as it is more inline with the MOND paradigm. The resulting temperature profiles are provided in figure 3.5. It is immediately clear that even for clusters with relatively tight fits to our model $A_0(\Phi)$ curve, the subsequent change in the temperature profile becomes quite significant. In all of the cases in our sample, such a deviation would be very apparent in observation.

3.2.1 Monte Carlo Constraints

In the previous section, it was established that EMOND fails to reproduce correct temperature profiles when applied to our cluster sample. In an effort to generalize these findings to a more comprehensive set of galaxy clusters, displaying a greater variation in their parameters and a closer link to the known cosmological constraints on galaxy clusters, at set of $N = 100$ idealized clusters were generated in Newtonian gravity using the following prescription. Galaxy clusters were generated on the basis of two parameters, M_{500} and the gas fraction f_g. For each cluster, these parameters (M_{500} and f_g) were generated from a uniform distribution between parameter values of $10^{13} - 10^{15}\mathrm{M}_\odot$ and $0.08 - 0.12$ respectively. The M_{500} parameter was sampled from a *log* uniform distribution to avoid biasing in favor of high mass clusters. From M_{500}, M_{200} was calculated approximately as $M_{200} \approx 1.23 M_{500}$ and the corresponding NFW concentration parameter was calculated using the model of Diemer and Joyce [45]. Each cluster was assumed to be at redshift $z = 0.05$. The total mass of the system was then modeled as a TNFW profile as described in Baltz et al. [13]. A corresponding ICM component was generated from density profiles of the form of equation 2.3 with parameters determined by the TNFW profile parameters. Thus, the core radius $r_c = (1/2)r_{2500}$ and the scale radius was set such that $r_s = 1.1 \cdot r_{200}$. α, β, and ϵ were uniformly set to 0.1, 0.67, and 3 respectively. The profile was then rescaled to produce the correct gas fraction as specified by the initial parameters. In this fashion, a fairly complete picture of galaxy clusters, as they are observed to appear in both simulation and observation, was generated. It should be remembered that the necessary $A_0(\Phi)$ curve for which a system would be able to rid itself of the need for dark matter in an EMOND paradigm may be calculated explicitly from the corresponding Newtonian model. Thus, the aim of this undertaking is to take a comprehensive sample of semi-realistic cluster models and test them against EMOND.

To that end, the correct A_0 curves were computed for each of the clusters in the

sample. For each, a model for A_0 in the same form as that used in the previous section was fit to the resulting $A_0(\Phi)$ curve and tabulated. Average values for both φ and Φ_0 were then computed and a bootstrapping procedure with $N = 1,000$ re-samplings was used to determine 95% confidence intervals on the $A_0(\Phi)$ curves. For each of the cluster models, the best fit $A_0(\Phi)$ curve was used to regenerate the cluster with the same gas and dynamical density profiles and the resulting temperature profiles were computed to maintain hydrostatic equilibrium despite the change in $A_0(\Phi)$. Figure 3.6 shows the sample of clusters used in this analysis, the $A_0(\Phi)$ curves computed for each cluster, the best fit model, and the resulting error in the temperature profiles. Notably, the observed error is somewhat lower than was observed in the models based on section 2.4, often around 10%. Figure 3.5 is somewhat misleading in this respect as the temperature profiles on different rows of the grid have different scalings, which gives the visual impression of higher error than is truly present. Errors in the observational models generally fell between 0.4 and 0.8; which is only marginally larger than predicted from the monte carlo approach. The underlying cause of this discrepancy is the specific shapes of the A_0 curves. Because the monte carlo sample comes from a more homogeneous set of profiles, the best fit A_0 curve has effectively the same shape as each individual A_0. In the observational models, the A_0 are more heterogeneous in their A_0 curves, which leads to greater scatter around the best fit. Nonetheless, several clusters in the simulation generate temperature errors on the order of 50%, which has just as dire implications for EMOND as was discussed in regard to the observationally motivated analysis previously described.

3.3 Discussion

In each of the paradigms described in this work, EMOND and MOND+DM, significant novel constraints were produced. These constraints prove to be a challenging

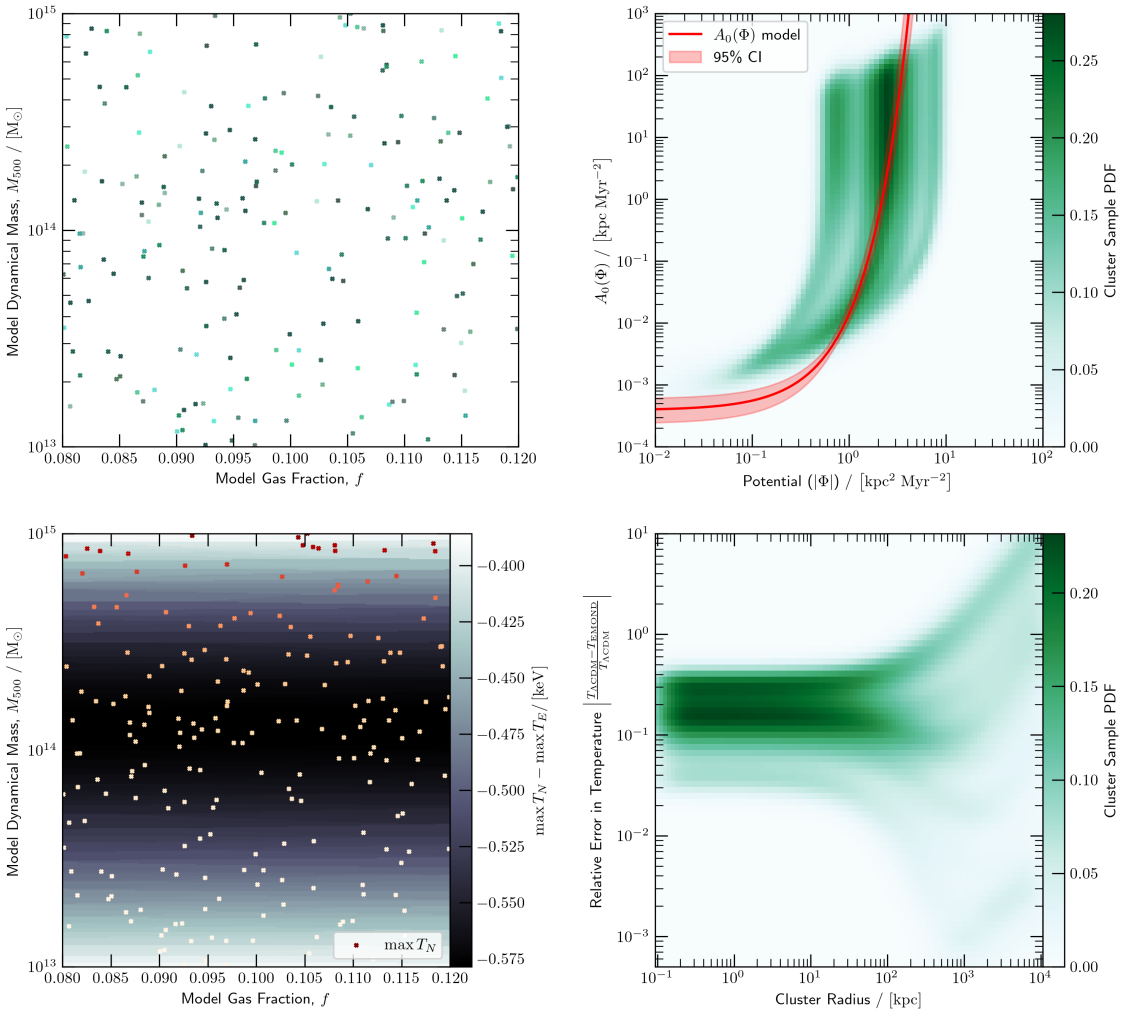

Figure 3.6: EMOND analysis of the idealized cluster models of section 3.2.1. (*upper left*) Generation parameters for each of the cluster models used in the cluster model. (*upper right*) Calculated $A_0(\Phi)$ curves for each of the simulated clusters. The heat map was created by applying a Gaussian kernel-density estimation algorithm to decompose individual curves into a representative PDF. The best fit curve was computed as the average of individual best fit models to each $A_0(\Phi)$ curve and has parameters $\varphi = 0.834\text{kpc}^2\text{Myr}^{-2}$ and $\Phi_0 = 0.80\text{kpc}^2\text{Myr}^{-2}$. The 95% confidence interval was generated by bootstrapping with $N = 1,000$ resamples. (*lower left*) Temperature profiles for each of the sample clusters in both the ΛCDM and EMOND paradigms. (*lower right*) The relative error in the EMOND temperature profile as compared to that of the ΛCDM equivalent.

hurdle for either formalism to contend with; especially given the already *ad hoc* nature of each of the extensions. Nonetheless, it would be premature to claim absolute rebuke of either theory. The underlying physics of galaxy clusters, particularly the assumption of (thermal) hystrostatic equilibrium and spherical symmetry, are not yet adequately understood to justify without skepticism the arguments made in this work. Because these assumptions are so deeply embedded in the methodology presented, the value of the constraints produced may only come to their full value after a better understanding has been established of the underlying physics. Despite these clear limitations, the constraints here presented set a clear bar for the continued development of MONDian extensions intended to resolve MOND's flaws in galaxy clusters. In the remainder of this section, we strive to discuss, in as critical and complete a sense possible, the implications of each of our findings for ΛCDM, for MOND, and for cluster physics in a general sense.

3.3.1 Fundamental Assumptions

In all of theoretical work presented, two assumptions are presumed axiomatically: that clusters are spherically symmetric and that the intracluster medium maintains hydrostatic equilibrium throughout the system. Both of these assumptions are known to be flawed, to some degree, in all observed clusters. Regardless, both of these assumptions remain foundational to X-ray observation and analysis of galaxy cluster [52, 47]. Our understanding of hydrostatic equilibrium in galaxy clusters continues to be at the forefront of scientific progress in the field. Studies combining X-ray observations with secondary methods (weak lensing in Smith et al. [129], SZ in Ghirardini et al. [59]) have shown hydrostatic mass biases ranging from 5-40% indicating that many realistic systems have meaningful non-thermal pressure components. In the work presented here, all such effects are ignored for the sake of mathematical viability and the generality of our approach; however, future work should broach the

issue of non-thermal support in the context of MONDian galaxy clusters. As it concerns observation, the issue of non-thermal pressure support (while of great interest) is generally excused on the basis that such tensions are of the same order as assorted projection effects, calibration error, and other general sources of noise [11]. Due to these various effects and the implicit effects our of assumption of absolute hydrostatic equilibrium, it remains the case that any argument claiming to refute a MONDian perpective must produce scatter from expectation on the order of 40% to be valid without further examination.

Spherical symmetry also plays a key role in our analysis in this work; however, these effects are of somewhat lesser importance than those of hydrostatic equilibrium [133, 15, 82, 121]. It should be noted that various aspects of MONDian dynamics differ in the context of a non-spherical system. In particular, the equivalence between QUMOND and AQUAL, is only valid in a spherically symmetric system; which would then imply that further analysis should be done to determine if important variations arise when considering each of these flavours in the context of this work.

3.3.2 MOND+DM

The constraints presented in this work regarding MOND+DM extensions of MOND provide a serious test for such theories. Despite the various assumptions discussed in the previous section, the theoretical implications of section 3.1 are nonetheless difficult to overlook. In the sample of clusters taken from Forman et al. [52], the observation that many clusters contain maximal viable radii well within r_{200} suggests that even with the various biases and systematics of observation, such discrepancies should be observable in, at least, a subset of known systems. Furthermore, the observation that temperature profiles (in the context of HSE) should have different asymptotic behaviours to those of ΛCDM is a fundamental aspect of MONDian gravity. In fact, to alter the theory in such a way as to eliminate this issue, one would

need to also eliminate the characteristic $1/r$ behavior of the gravitational field in low acceleration regimes. Doing so would have severe consequences for MOND in those regimes where it currently succeeds. Thus, the findings of this work indicate that including additional phantom sources of mass in MONDian gravity theories is likely not a viable approach for the continued evolution of the MONDian research paradigm. As it stands, only a significant shift in our understanding of cluster physics, in turn massively altering the observations and assumptions underlying our analysis, would be sufficient to allow these extensions to have any chance at viability. From the standpoint of ΛCDM, it seems reasonable to conclude that MOND, in this particular manifestation, is completely and irreparably flawed in the cluster regime; a conclusion which places yet more pressure on the MONDian paradigm to confront these flaws if indeed it has any hope of challenging concordance cosmology. In the context of the MOND paradigm, the developments presented here may be seen as a step forward in our understanding of MOND's behavior in galaxy clusters. Further work attempting to resolve the theoretical pitfalls that plauge the paradigm in this regime can, with relative certainty, ignore the option of including additional, unobserved, mass. Doing so is also in better accord with developments in relativistic MOND and other modified gravity theories and effectively eliminates a significant number of dead ends.

3.3.3 EMOND

Whereas the implications regarding MOND+DM were straight forward, EMOND presents a more complex picture. There are clear flaws in the formalism, particularly in regard to the gauge dependence of the $A_0(\Phi)$ function; however, such flaws may show themselves to be merely the effect of relying an empirical theory. In our analysis, the choice to make $A_0(\Phi)$ a function of $\Phi - \varphi$ effectively eliminates the issue of gauge dependence so long as the (supposed) fundamental theory leading to EMOND provides some context under which $\Phi - \varphi$ is resolved in a gauge invariant way. Zhao

and Famaey [148] observed in their original work that this may arise from the weak field approximation of a more consistent, relativistic, form of the underlying theory.

If one accepts that the inelegant aspects of the formalism may be disregarded, then the implications of our analysis still cast doubt on EMOND's capacity to account for the missing mass problem in clusters of galaxies. In applying HSE to the cluster sample of Forman et al. [52], it is clear that the calculated, best-fit, $A_0(\Phi)$ is manifestly incompatible with observations of the clusters. In each of the 13 clusters included, deviations in the temperature profiles calculated by enforcing a uniform $A_0(\Phi)$ are well within the range for which X-ray observation would be able to distinguish. Thus, the fact that such discrepancies are not observed implies that EMOND warrants serious doubt as a potential approach for correcting MOND in clusters of galaxies.

On the other hand, when analyzed in the context of the cosmologically motivated cluster models in section 3.2.1, EMOND fares far better. In fact, relative temperature errors, as shown in figure 3.6, on the order of only 10% are not sufficient to rule out an EMOND paradigm. One is therefore faced with a remaining point inquiry; namely whether the results of section 3.2 refute EMOND on the basis of the observational models, or supports EMOND on the basis of the more theoretical models. It is our assessment that the deviations observed in the temperature profiles of the observationally produced models present a serious constraint to EMOND theory; however, more work should be done to establish whether or not the deviations predicted here can be evaded by more accurate observation methodology. Regardless of one's preference regarding which models are most valid, this work firmly establishes an observational context through which to test the extended MOND paradigm.

3.4 Conclusion

In this work, we have explored the current position of the MOND research paradigm in galaxy clusters and illustrated many of the persistent difficulties involved in generating an observationally consistent MOND theory. By analyzing a set of galaxy clusters using the assumption of hydrostatic equilibrium, we demonstrated that there were severe weaknesses in both the MOND+DM paradigm and the EMOND paradigm. In the case of MOND+DM, we demonstrate that there exist strong constraints on the physicality of the necessary dark matter component which bring into question the validity of the theory at large radii. Nonetheless, our analysis of the MOND+DM paradigm was not conclusively at odds with observation and therefore requires moderate improvements in observational equipment to be conclusively demonstrable. Our constraints, when applied to ideal models of galaxy clusters, paint a worrying picture with many of the clusters failing to be consistent with the MOND approach well within the expected observable domain.

In our analysis of the Extended MOND approach, we demonstrated that, while our cluster sample was well fit by reasonable functions for $A_0(\Phi)$, the resulting scatter in that relation was far too significant to produce allowable differences in the galaxy cluster's temperature profile. A secondary analysis of a broader, but more theoretical, set of cluster models indicates a far smaller scatter which may be consistent with observation. Nonetheless, even in these systems, deviations on the order of 10% in the temperature profiles are predicted and should be observable in, at least, a subset of systems. We therefore conclude that the EMOND approach as presented in this paper is likely invalid as a method by which to rectify MOND gravity in galaxy clusters and that the persistent failure of MOND to produce reasonable extension which can explain the missing mass in galaxy cluster is indicative of some degree of stagnation in the theoretical progression of the MOND paradigm.

Chapter 4

Non-Equilibrium MOND Phenomenology in Clusters

The constraints described thus far in this work have been focused solely on dynamics assumed from hydrostatic equilibrium. In this section, we expand this picture somewhat by considering more generalized phenomena beyond this simple picture. Much of the work presented in the chapter is ongoing and is presented only to the degree to which it has thus far been developed. The selected topics presented are representative only of a small sample of the various phenomena for which MONDian dynamics predicts observable variation. Further work is required to establish more completely the extent to which non-equilibrium dynamics can be used as a probe for the validity of MOND and its subsidiary theories.

4.1 Fluid Effects

The fluid dynamics of galaxy cluster mergers is a fascinating field in its own right, and much work has been dedicated to understanding the important physical processes which occur in these events. Because the ICM is a diffuse plasma, galaxy cluster mergers often occur at or above the relevant speed of sound in the plasma, which

leads to interesting effects, including high energy shocks[89, 106, 27], cosmic ray acceleration[29, 68] and inverse Compton scattering[88]. In this section, we discuss some of the theory behind the observed fluid dynamical effects in mergers and explore re-derivations of the relevant models for MOND gravities.

4.1.1 The Mathematics of Infall

In classical treatments, one can use Kepler's 3rd law to determine the effective separation distance d_0 between two clusters based on their collision time. In doing so, we may obtain a first order approximation of the relevant speed of the merger. A complete discussion of this approach is described in [120]; however, we will only summarize the approach here. Consider a cluster merger with masses M_1 and M_2. In the Newtonian paradigm, these clusters are (for large separations) effectively point particles on Keplerian orbits. Assuming that, before the beginning of the infall, the clusters were tied to the hubble flow and were effectively stationary in their radial displacement, we may posit an initial separation d_0 between the clusters. By Kepler's 3rd law,

$$d_0 \approx (2G(M_1 + M_2))^{\frac{1}{3}} \left(\frac{t_m}{\pi}\right)^{2/3},$$

where t_m is the time at the point of merger. The equivalent computation in MOND is hardly as simple. Because MOND is not one of the classically determinable potentials for the central force problem, there is no analytical form for its orbits[28]. This implies, among a great many other interesting phenomena, that Kepler's 3rd law is invalid in modified gravity, at least in the DMR. We therefore employ an alternative approach. Consider each of the clusters is separated by distance d_0 and radially stationary to

each other. The acceleration experienced by the effective single body is

$$\ddot{\mathbf{r}} = -\frac{\sqrt{G(M_1+M_2)a_0}\hat{\mathbf{r}}}{r}.$$

Letting $\alpha = \sqrt{G(M_1+M_2)a_0}$, the differential equation reduces to

$$\ddot{r} = \frac{-\alpha}{r}.$$

This differential equation is non-linear, but has a solution

$$r(t) = \exp\left\{\frac{c_1 - 2\alpha \mathrm{erf}^{-1}\left(\Omega(c_2+t)\right)^2}{2\alpha}\right\},$$

where Ω is

$$\Omega = \pm\sqrt{\frac{2}{\pi}}\sqrt{\alpha e^{-c_1/\alpha}}.$$

Recognizing that c_2 has units of time, we expect that it should play the role of some time offset; however, because we may arbitrarily relabel the time variable, we choose to let $c_2 = 0$. If we then enforce the initial condition that $r(0) = d_0$, we find that $c_1 = 2\alpha \ln(x_0)$, which reduces the solution to the form

$$r(t) = d_0 \exp\left[-\mathrm{erf}^{-1}\left(\Omega t\right)^2\right], \quad \Omega = \sqrt{\frac{2\alpha}{\pi}} x_0^{-1}.$$

The final expression for $t(r)$ is then found to be

$$t(r) = \sqrt{\frac{\pi}{2}}\left(G(M_1+M_2)a_0\right)^{-1/4} d_0 \mathrm{erf}\left(\sqrt{-\ln\left(\frac{r}{d_0}\right)}\right) \tag{4.1}$$

Given that $d_0 \gg r$, we would ideally expand in powers of r/d_0; however, $\ln(x)$ is degenerate at 0 preventing this approach. If one assumes a relevent parameter $\delta =$

$r_{\rm col}/d_0$, then it follows that as a function of $M_1 + M_2$, the infall time becomes

$$t_{\rm fall}(M) = M^{-1/4}\sqrt{\frac{\pi}{2}}\left(\frac{1}{Ga_0}\right)^{1/4} d_0 {\rm erf}\left(\sqrt{-\ln(\delta)}\right) = \upsilon_{\rm fall} M^{-1/4}$$

In the Newtonian regime, we've seen that $t_{\rm fall} \sim M^{-1/2}$ as well; however, the constants are decidedly different.

Let's turn our attention to collision velocities. In the Newtonian regime, we have

$$\begin{aligned} L &\approx \mu v_{\perp,0} d_0 \approx \mu v b \\ E &\approx \frac{1}{2}\mu v_{\perp,0}^2 - \frac{GM_1M_2}{d_0} \approx \frac{1}{2}\mu v^2 - \frac{GM_1M_2}{d} \end{aligned}$$

at the turnaround point. By enforcing the conservation of these quantities, one arrives at

$$v^2 \approx 2G(M_1+M_2)\left(\frac{1}{d} - \frac{1}{d_0}\right)\left[1 - \left(\frac{b}{d_0}\right)^2\right]^{-1} \approx \frac{2G(M_1+M_2)}{d}. \tag{4.2}$$

In MOND, a similar procedure may be used; however, the expression for the energy will necessarily change. Consider at some distance d the two clusters are sufficiently separated to remain in the DMR. This is the case in the beginning of most simulations with clusters separated on the order of 1-3 Mpc. Then the difference in energy is determined by integrating the potential, leading to

$$\Delta U = \mu \int_d^{d_0} \frac{\sqrt{G(M_1+M_2)a_0}}{x} dx = \mu\sqrt{G(M_1+M_2)a_0}\ln\left(\frac{d_0}{d}\right).$$

As such, the energy is instead

$$E \approx \frac{1}{2}\mu v_{\perp,0}^2 - \mu\sqrt{G(M_1+M_2)a_0}\ln\left(\frac{d_0}{d}\right)$$

If we now eliminate v_0, we find

$$v^2 \approx 2(M_1 + M_2)\sqrt{\frac{Ga_0}{M_1 M_2}} \ln\left(\frac{d_0}{d}\right)\left(1 - \frac{b^2}{d_0^2}\right)^{-1}$$

And so

$$\Omega^2 = \frac{v_N^2}{v_M^2} = \frac{1}{2}\sqrt{\frac{G(M_1 + M_2)}{a_0}}\left[\frac{1}{d_c} - \frac{1}{d_{0,N}}\right]\ln^{-1}\left(\frac{d_{0,M}}{d_c}\right)\left[\frac{\left(1 - \frac{b^2}{d_{0,M}^2}\right)}{\left(1 - \frac{b^2}{d_{0,N}^2}\right)}\right] \tag{4.3}$$

Let $\eta = d_c/d_{0,N}$ and let $\xi = d_c/d_{0,M}$. Furthermore, let

$$\kappa = \frac{-d_c}{2}\sqrt{\frac{G(M_1 + M_2)}{a_0}}.$$

Then the equation reduces to

$$\Omega^2 = \kappa\,(1 - \eta)\ln^{-1}(\xi)\left(\frac{1 - l^2\xi^2}{1 - l^2\eta^2}\right),$$

where $l = b/d_c$.

If we assume that a collision occurs at time t_0, then, assuming $d_0 \gg d_c$ for both clusters,

$$\Omega(t) = \frac{-d_c}{2}\sqrt{\frac{GM}{a_0}}\left(1 - \left[d_c\,(2GM)^{-1/3}\left(\frac{t_0}{\pi}\right)^{-3/2}\right]\right)\ln^{-1}\left(\sqrt{\frac{2GMa_0}{\pi}}\frac{d_c}{t_0}\right)\left(\frac{1 - l^2\xi^2}{1 - l^2\eta^2}\right)$$

The most important outcome of these calculations is the modified collision speed in a MONDian paradigm, which will fundamentally influence the nature of cluster mergers as we will discuss in the next section.

4.1.2 Shocks in Major Mergers

In most cluster mergers with mass ratios on the order of unity, strong shocks are occur as each constituent cluster drive its ICM at velocities significantly larger than the relevant mach number $\mathcal{M}$. Shocks of these sorts are observed in a variety of systems, most famously the bullet cluster[41, 125] which hosts an undeniable bow shock with a mach number around 3.2[90]. Due to the complexity of the resultant system, these phenomena of cluster mergers are generally studied by simulation; however, there are a few analytical predictions which will be of interest later in this work.

In Newtonian mechanics, the virial theorem (in its usual astrophysical form) dictates that the thermal energy of the ICM in either of the merging clusters is

$$\langle K \rangle = -\frac{1}{2} \langle V \rangle .$$

Because the clusters involved in the merger are assumed to have fallen from a sufficient distance that they were not gravitationally bound to one another, it follows that they should have a collision velocity on the order of the relevant escape velocity, which corresponds to an energy of $\langle V \rangle$. As such, the collision occurs with velocities approximately twice that of the latent ICM and should therefore result in Mach numbers on the order of $\mathcal{M} \sim 2$. This is in agreement with observations of such systems[85, 57, 26].

The treatment of this problem in a MONDian gravitational paradigm is somewhat more complex. It has been shown[99, 101] that for a virial of the form

$$\mathcal{V} = -\int d^3r \;\; \rho \mathbf{r} \cdot \mathbf{g}, \tag{4.4}$$

A MOND virial theorem may be derived in the form

$$\left\langle v^2 \right\rangle \equiv \frac{2}{3}(MGa_0)^{1/2} + \frac{1}{4\pi MG}\left\langle \int d^3r \, \left[2\nu g_N^2 - \frac{3}{2}a_0^2\mathcal{Q}\right]\right\rangle_t ,$$

where $\mathcal{Q}$ is the function in the QUMOND Lagrangian, ν is the interpolation function, M is the total mass of the system. In the deep MOND regime, the integral term vanishes and leaves just

$$\left\langle \mathbf{v}^2 \right\rangle = \frac{2}{3}\left(MGa_0\right)^{1/2}. \tag{4.5}$$

As such, let two clusters $i = 1, 2$ be colliding from free fall. The free fall occurs in the DMR and therefore implies that

$$\ddot{r} = -\frac{\sqrt{G(M_1+M_2)a_0}}{r}, \implies v(r) = \sqrt{2}(G(M_1+M_2)a_0)^{1/4}\sqrt{\ln\left(\frac{r_0}{r}\right)} = \sqrt{2\Phi}.$$

Once the two clusters become close enough that their profiles begin to interact, the collision will still be in the DMR for any physically realistic set of clusters. As such, the velocity ratio of the generated shock when it is in the DMR is

$$\eta_i^2 = \frac{v_c^2}{\left\langle v^2 \right\rangle_i} = 3\sqrt{R_i^{-1}}\ln\left(\frac{r_0}{r}\right), \tag{4.6}$$

where R_i^{-1} is the relative mass of the ith system to the total mass. Using a characteristic infall distance of 16 Mpc, and a collision distance of 1 Mpc, we see that $\eta_i^2 \approx 9\sqrt{R_i^{-1}}$. In an ideal gas,

$$c = \sqrt{\frac{\gamma kT}{m}} = \sqrt{\frac{\gamma\left\langle v^2\right\rangle_i}{3}} \approx \sqrt{\frac{\gamma}{3\eta_i^2}}v_c = \frac{1}{9}\sqrt{5}R_i^{1/4}v_c. \tag{4.7}$$

Generically, this forms a function of the mass ratio for each of the systems; however, it is clear that in a scenario with a mass ratio of 1:1, $v_c = (0.5)^{-1/4}9/\sqrt{5}c$

resulting in a Mach number $\mathcal{M} \approx 5$. Therefore, we expect shocks in the realm of $2\times$ as strong as is predicted in Newtonian mechanics.

While this is a non-trivial result and certainly has implications for the observable physics of galaxy clusters, there are some significant caveats. The greatest of these is that the shock generally *forms* in the DMR, but need not be observed in the DMR. Needless to say, it is far easier to observe shocks once they are fully developed, typically around the epoch of pericentric passage in the merger. It is therefore also necessary to consider what happens to these merging clusters as the exit the DMR and enter the Newtonian regime, where we are most likely to make our observations. Ignoring for the moment the ever present issue of the interpolative regime, Newtonian regime, we (by the correspondence principle) have the virial theorem of the form

$$\langle K \rangle = -\frac{1}{2} \langle U \rangle \sim \frac{GM_{\rm dyn}(< r)}{2r},$$

We therefore find that the relevant velocity ratio $\eta_{i,\rm NR}$ is given simply by

$$\eta_{i,\rm NR}^2 = \frac{v_c^2}{\langle v_N^2 \rangle_i} = \frac{2\sqrt{G(M_1+M_2)a_0}\ln(r_0/r)}{GM_i/r} = 2r\ln(r_0/r)\sqrt{\frac{a_0 R_i^{-1}}{GM_i}} \tag{4.8}$$

For the same characteristic r_0 as above, but this time with a characteristic collision distance of only 500 kpc, we find the approximate relation

$$v_c = \sqrt{\frac{3\eta_{i,\rm NR}^2}{\gamma}}c \approx \sqrt{\frac{1.034\times 10^{16}\ \mathrm{M}_\odot}{R_i M_i}}c. \tag{4.9}$$

For a simple mass ratio of 1:1 and a characteristic mass of 1×10^{15} solar masses, we find shocks with $\mathcal{M} \approx 4$; however, for *lower mass systems*, say on the order of 1×10^{14} solar masses, we predict shocks with much higher Mach numbers, on the order of $\mathcal{M} \approx 14$.

Having now derived these results, there are 3 notable conclusions which should be

carried forward:

1. Merger shocks in the outskirts of galaxy clusters which are assymptotically in the DMR should be somewhat *higher* Mach number than the equivalent Newtonian systems.

2. Merger shocks in the Newtonian regime should strengthen as the traverse the ICM from the DMR regime.

3. Merger shocks in the Newtonian regime are are more mass dependent than they would be without MOND.

The final of these conclusions follows from the additional M_i term in the Newtonian regime (equation 4.9), which can produce significantly stronger shocks than would have been expected in a purely Newtonian analysis. While these results clearly il-

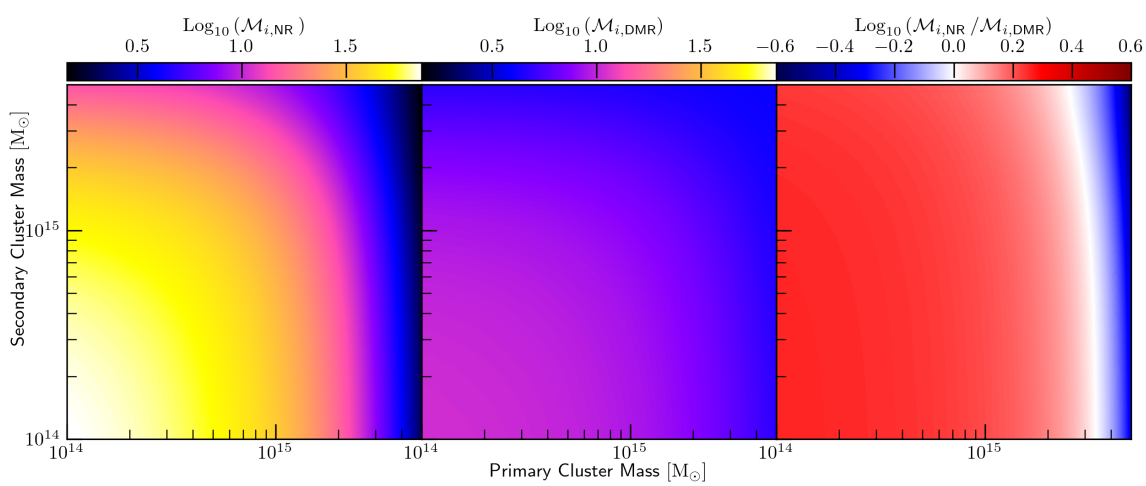

Figure 4.1: Comparison of the expected Mach numbers ($\mathcal{M}$) in both the Newtonian and MOND regimes (left and center) as well as their ratio (right). Collision radii where 1 Mpc for the MOND regime and 500 kpc for the Newtonian regime. Infall distance was 16 Mpc in all cases.

lustrate a divergence of MOND from the generally observed phenomenology of such shocks, showing this to be true is nontrivial. Because the MOND regime shocks occur at larger radii in the relevant clusters, direct observation of such shocks which also possess the necessary depth of data to allow for an accurate determination of $\mathcal{M}$ to

within the necessary accuracy is doubtful. In the Newtonian regime, it may be possible to observe the very strong shocks created by mergers between progenitors with significantly different masses; however, it should also be noted that for sufficient mass differentials between the two progenitor systems, additional effects may obscure our conclusions, particularly the occurrence of ram pressure stripping and the retarding force generated by the substantial pressure built up. We therefore save any conclusive statements about these phenomena for our treatment of hydrodynamic simulations in the later part of this work.

The fluid dynamics of galaxy cluster mergers is a fascinating field in its own right, and much work has been dedicated to understanding the important physical processes which occur in these systems. Because the ICM is a diffuse plasma, galaxy cluster mergers often occur at or above the relevant speed of sound in the plasma, which leads to interesting effects, including high energy shocks [89, 106, 26], cosmic ray acceleration [29, 68] and inverse Compton scattering [88]. In this section, we discuss some of the theory behind the observed fluid dynamical effects in mergers and explore re-derivations of the relevant models for MOND gravities.

4.1.3 Ram Pressure Stripping

When gravitationally bound systems of any kind fall into a galaxy cluster, they encounter a ram pressure from the ICM which behaves as

$$P_{\text{ram}} = \rho_{\text{ICM}} v_{\text{fall}}^2, \tag{4.10}$$

where ρ_{ICM} is the intracluster medium's density and v_{fall} is the infall velocity of the relevant system. The additional force caused by the ram pressure is capable of stripping large fractions of the gas away from the infalling system, a phenomena called ram pressure stripping. It has been suggested that the advent of ram pressure

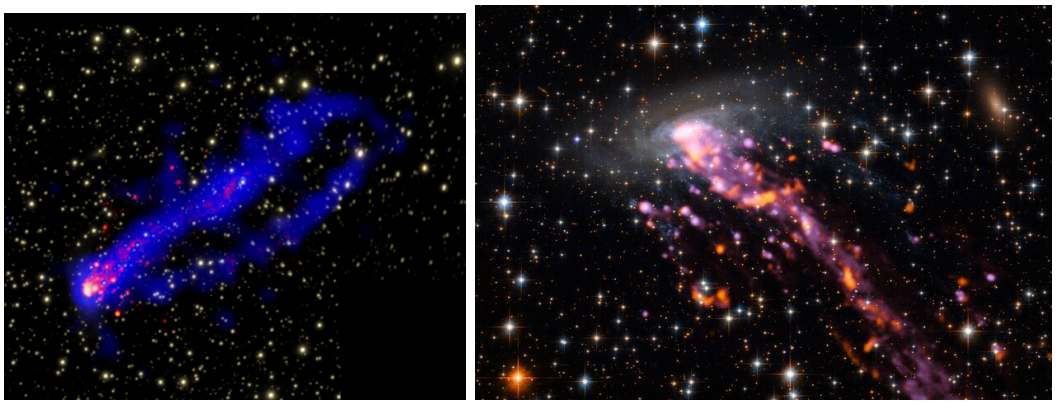

Figure 4.2: Two composite images of so called jellyfish galaxies caused by ram pressure stripping. (Right) ESO 137-001 as it falls into the Norma galaxy cluster. Composite image is composed of observations in the visible (HST-ACS and HST-WFC3), in the millimeter band (orange, ALMA) and in the H-α band (Pink, VLT-MUSE). (Left) ESO 130-001 falling into Abell 3627 with two ram-pressure induced tails. In this image, blue tails are Chandra observations (X-ray) and red regions are H-α observations from SOAR. In both systems, high luminosity in H-α implies star formation in the gasseous tails.

stripping can explain (in part) the observation that systems in galaxy clusters are generally very low in star formation.

The standard approach to modeling ram pressure stripping, introduced by Gunn and Gott [61], is predicated on the observation that the gasseous component of the system will only experience stripping if the ram pressure is suitably large to surpass the maximal restoring force due to gravity. Applying this rationale to in-falling spiral galaxies is particularly trivial and yields a ram-pressure stripping bound of the form

$$P_{\text{ram}} \geq 2\pi G \Sigma_\star \Sigma_{\text{gas}}. \tag{4.11}$$

This bound has been well justified in simulation [76, 115, 144, 3]. The bound in equation 4.11 is based on the assumption that the disk behaves as a Kuzmin Disk without any additional halo or bulge component. If one adds an additional dark matter halo component, Ψ_{dm}, then the condition becomes

$$P_{ram} \geq 2\pi G \Sigma_\star \Sigma_{gas} + \Sigma_{gas} \left.\frac{\partial \Psi_{dm}}{\partial r}\right|_{r=(z_0^2+R^2)^{1/2}} \frac{z_0}{\sqrt{R^2+z_0^2}},$$

where z_0 satisfies the equation

$$\frac{\partial^2 \Psi_{dm}}{\partial r^2} z^2 \sqrt{R^2 + z^2} = -\frac{\partial \Psi_{dm}}{\partial r} R^2.$$

Even for spherical systems, the above logic still holds. In a spherical system, the least gravitationally bound mass will strip away first from the outer projected annuli of the system. If a projected annulus has surface density $\Sigma_{\rm gas}(R_p)$, where R_p is the projected radius, then

$$P_{\rm ram}(R_p) \leq \Sigma_{\rm gas}(R_p) \left. \frac{\partial \Phi}{\partial z} \right|_{\rm max}.$$

There are several considerations which must be acknowledged when considering an equivalent problem in the context of a MONDian paradigm. Firstly, the underlying fields of the infalling system and its bounding system will be manifestly different than those predicted by Newtonian mechanics. Not only is this due to the differences in the constituent mass components of each of the systems, but also because of the EFE present in all MOND theories. To compound these differences, the lack of a similarly massive dark matter halo in the system being stripped should intuitively lead to a more rapid loss of mass in the Newtonian regime. To fully characterize the phenomenology of ram pressure stripping in MOND, we consider each relevant domain of theory individually. In the remainder of this section, we will discuss at length the behavior of ram pressure stripping in such situations.

4.1.4 In a Newtonian External Field

When a system S falls into a cluster, it is presumed that during that in-fall, the system traverses the DMR regime, the interpolative regime, and eventually the Newtonian regime. It is well known that many massive clusters of galaxies fall into the Newtonian regime to relatively large radii, even as far as r_{500}. Given the significantly less dense

nature of the ICM at those radii, it is sometimes reasonable to assume that ram pressure stripping occurs within an external field which is everywhere larger than a_0. In this section, that scenario (which is the simplest) will be described.

Let a disk galaxy be falling, face-on, into a galaxy cluster in such a way as to be in a fully Newtonian regime. Clearly the standard approaches of Newtonian dynamics apply, therefore, the constraints of equation 4.11 are equally viable; *however*, there are some remaining conclusions to be drawn from this simple scenario. Most importantly, because the galaxy should be entirely devoid of dark matter (MOND doesn't need dark matter to describe galaxies), its capacity to provide a restorative force should be diminished. Therefore, it is quite evident that in Newtonian regimes, ram pressure stripping should occur faster in MOND paradigms than in the Newtonian case. Further development is necessary to determine the precise extent of this excess stripping; however, sufficiently large discrepancies could be used as constraints on MONDian gravity when compared with the color distribution of galaxies within clusters. The condition in equation 4.11 will apply in the MOND case; however, the Newtonian equivalent system should experience an additional contribution of

$$|g_{\mathrm{max},M} - g_{\mathrm{max},N}| = \Sigma_{\mathrm{gas}} \left.\frac{\partial \Psi_{dm}}{\partial r}\right|_{r=(z_0^2+R^2)^{1/2}} \frac{z_0}{\sqrt{R^2+z_0^2}}$$

Generally, the additional term here should not contribute too much to the overall dynamics and one expects the MONDian system to behave more or less the same as the corresponding Newtonian system.

4.1.5 In a MONDian External Field

In a MONDian external field, the behavior differs significantly from the Newtonian case. Recall the BMEE (equation 1.7) takes the form

$$\nabla\delta(\theta, r) \approx \frac{M_{\rm dyn}}{r^2} \underbrace{\left(G\mu_E^{-1}(1+L_E)^{-1/2}\right)}_{G_{\rm EFE}} (\hat{e}_r - \alpha_E \cos(\theta)\hat{e}_z)(1-\alpha_E\cos^2(\theta))^{-3/2},$$

where $\hat{e}_r$ is the unit vector in the spherically radial direction ant $\hat{e}_z$ points in the direction of the external field. L_E, α_E, and μ_E are defined as they were in chapter 1. In this case, the question of maximal restoring force is somewhat more complex. If one assumes that the stripping occurs sufficiently far that $\partial_z M(< r) \sim 0$, then the effective restoring force in the z direction is

$$a_{\rm restore} = \frac{M\tilde{G}(1-\alpha_E)z}{r^3}, \quad z \ll r.$$

We find that the maximal value of this restoring force is

$$a_{\rm restore,max} = \frac{M\tilde{G}(1-\alpha_E)}{\sqrt{3}r^2},$$

and the ram pressure stripping condition becomes

$$P_{\rm RAM} \leq \frac{4}{3\sqrt{3}}\pi\Sigma_{\rm gas}\left\langle\rho_{\rm dyn}\right\rangle \tilde{G}\left(1-\alpha_E\right). \tag{4.12}$$

The equivalent expression in the Newtonian paradigm differs by $\tilde{G}\left(1-\alpha_E\right)$ from this one. Figure 4.3 shows these two distinctive regimes of the EFE and their impact on the potential for ram pressure stripping. It should be noted that in the Newtonian regime, despite indicating that the necessary stripping thresholds are the same, this doesn't take into account differences in the total mass of equivalent systems. In the Newtonian regime, one would expect the ram pressure to have a lower threshold by

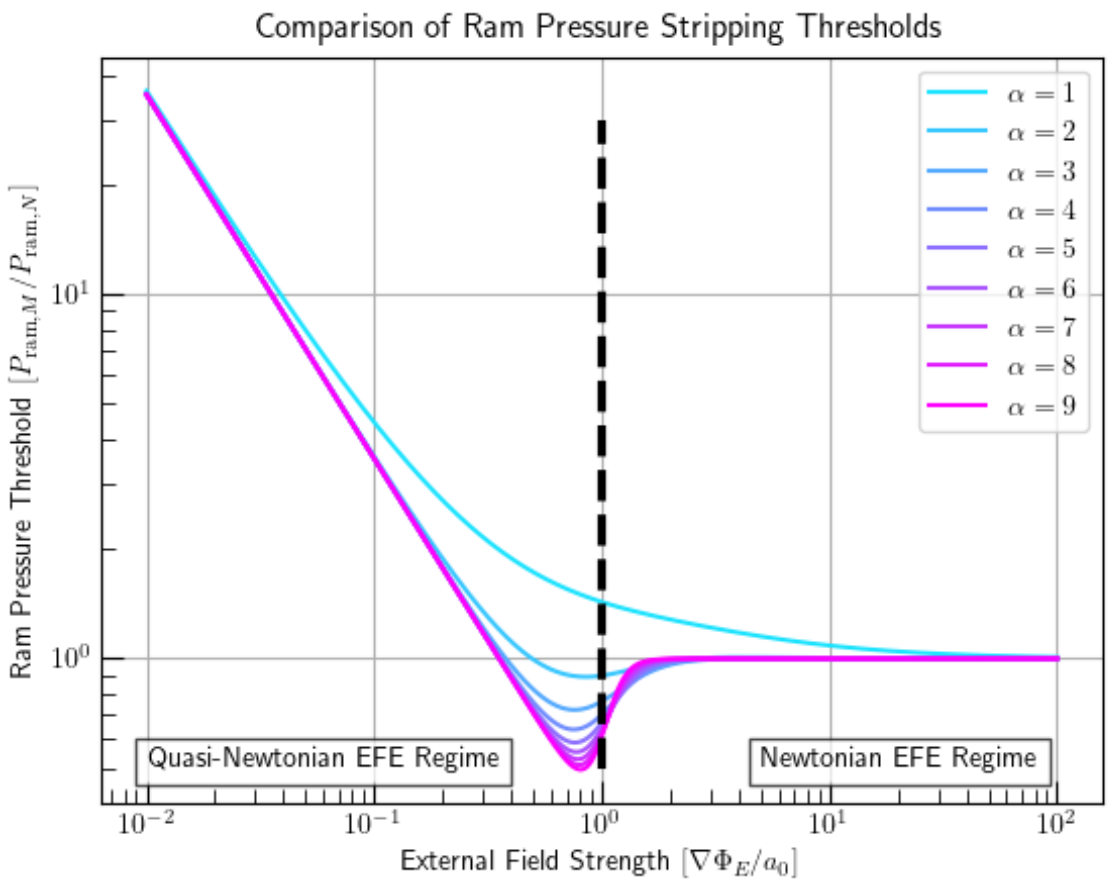

Figure 4.3: Relative minimum ram pressure for stripping to occur in Newtonian and MONDian paradigms. Resulting curves are shown for interpolation functions of the form $\mu(x) = 1/(1+x^{\alpha})^{1/\alpha}$. The ratio of the pressure thresholds is $G_{\mathrm{EFE}}(1+\alpha_E)/G$. The quasi-linear domain is characterized by MOND systems which are significantly more robust against stripping, particularly for small α. In the Newtonian regime, the expected return to the asymptotic behavior appears.

some (potentially quite small) degree due to additional stability of the halo in the Newtonian equivalent system. Nonetheless, in comparing, *ceterus parabis*, clusters in each of the two paradigms, it is clear that in the DMR, MONDian systems are considerably more resistant to ram pressure stripping. The obvious question which has not yet been discussed is whether, in practical application, there is ever a sufficient ram pressure in the DMR to strip a Newtonian system, let alone a MONDian one. This question is not easily treated as it is highly model dependent; however, these hypotheses may be put to the test in simulation, as will be done in the next chapter of this work.

4.2 Impacts

The findings presented in this section provide only a precursory account of the potential dynamical tests for MONDian gravity in galaxy clusters. A more careful examination of the relevant dynamics, particularly in the context of numerical simulations, are necessary to fully characterize the expected phenomenology. Nonetheless, our findings indicate a non-trivial expectation for both the emergence of merger shocks and the nature of infalling galaxies. The constraints placed on shocks in major mergers is apparently in tension with observed systems [e.g. 120, 112], which observe Mach numbers on the order of 2, instead of our predicted 4-5. Our findings regarding ram pressure stripping are not well tested and pose a potential test for MONDian dynamics; however, the feasibility to actually carrying out such a test is, as yet, unclear. Our work in this regard is ongoing, particularly in regard to the generation of hydrodynamics simulations which could provide a more detailed examination of these effects.

Chapter 5

Discussion

In an effort to critically evaluate the results presented in this work and their intersections with the various research paradigms in which we are interested, this chapter is framed upon a philosophical evaluation. Regardless of the results here presented, neither MOND nor ΛCDM is entirely self-consistent; persistent refutations undermine critical aspects of both theories. As such, we cannot aim to evaluate the merits of this work or the merits of either of these research paradigms on the sole basis of their "correctness". Instead, we formulate our discussion around the philosophical and sociological implications our work (and other concurrent works) imply regarding the progress of the field. The remainder of this chapter is laid out as follows: in section 5.1, a brief summary of the philosophical background is presented with the aim of supplying a framework on which to base the subsequent evaluation of our work. Sections 5.2 and 5.3 present a contemporary evaluation of MOND from both a confirmatory and dissenting lens. Finally, section 5.4 presents our thoughts on the potential for future progress in the MONDian paradigm and a discussion of the long-term outlook for the field of cosmology.

5.1 Scientific Philosophy

Foundational philosophical thought regarding questions such as "what makes a theory scientific?" and "how can one compare two theories?" has experienced continuous development since antiquity. Renaissance thinkers, most notably Bacon [12], pioneered the notion of *inductive empiricism* which would eventually form the underpinnings of the "classical" scientific method as it is generally taught [40]. In the framework of inductive empiricism, scientific progress is cyclic and cumulative: novel hypotheses are tested by experiment. Sufficient experimental support for a given hypothesis leads to said hypothesis being regarded as a physical truth and thus a legitimate basis on which to form new hypotheses. In this way, a particular scientific field progresses by the recursive cycle of hypothesis and experiment.

While this "classical" view of science successfully describes many of the key characteristics of our scientific traditions, it falls short in many, significant regards. Inductive empiricism clearly captures the importance of experimentation in scientific inquiry; however, the reality of scientific practice is far removed from this simple heuristic. Much of scientific practice, this work included, is not founded on the basis of hypothesis. In fact, most scientific works focus on fact finding, methodological refinement, or further exploration of existing theory, not on positing new theory. Furthermore, it is well established that inductive reasoning of the type used in the scientific method is not generically valid. Not only can biases suffered by the practitioner color the rationale for a given experimental outcome, but inductive reasoning is fundamentally predicated on the notion that what is true now will be true later (see for example Wason [145]).

In searching for a scientific framework which is both sufficiently representative of real scientific practice and which provides a basis for comparison and evaluation of theory, the classical scientific method falls short and must be replaced by a more refined model. There are many such frameworks: logical positivism, philosophical an-

archism, falsificationism, and sophisticated methodological falsificationism to name a few (see Hodson [67] for an introduction). In this discussion, we limit ourselves to the ideas of falsificationism: the notion that science progresses by attempted refutation and persistent evasion thereof by hypotheses. The basis of falsificationism was first introduced by Popper [114], which presents scientific progress as a cycle of theory development followed by attempted refutation and subsequent theoretical refinement. In this view, the purpose of experiment is singular: to falsify hypotheses. Theories which are refuted by experiment are discarded and those which are resistant to refutation are incorporated into the canon of physical law until such time as they suffer refutation. This picture of science captures the central framework we utilize in this chapter: theories may be compared on the basis of their falsifiability. A theory that makes bold predictions and evades refutation proves itself to be a stronger theory than one which makes lesser predictions.

Classical falsificationism (as described by Popper) meets our need for a framework on which to base comparison; however, it is not a reasonable representation of the actual practice of science. Science very rarely discards a potential paradigm on the basis of a single refutation; if it did, then neither ΛCDM or MOND would even be considered as candidate frameworks. Furthermore, it is well established that once a particular paradigm has been adopted by the community, significant effort goes into finding an interpretation of emergent experimental inconsistencies which does not rebuke the underlying paradigm [75]. One popular alternative which nullifies this issue (and the one which we will use in this work) is the "sophisticated" methodological falsificationism of Lakatos [78]. In this framework, the core ideas of Popper's falsificationism are maintained; however, theories no longer form the atomic units of scientific inquiry. Instead, the "research programme" serves as the basic element of science. A research programme is defined by three components: the *hard-core*, the *heuristic*, and the *auxiliary hypotheses*. The iterative theories present in a research

program comprise the auxiliary hypotheses, each an iterative improvement over the one before. The hard core of a research program represents the indelible basis of the program: it is the set of fundamental characteristics that ties all of the constituent theories together. Finally, the heuristic forms a critical roadmap for the progression of the research program. It lays out the open questions of the paradigm and any extant inconsistencies that must be contended with.

For Lakatos, it is the research program which is tested by experimentation. For each auxiliary hypothesis refuted by experimentation, a novel hypothesis must emerge which can account for the apparent refutation. If a research program fails to do this, then it is in a state of degeneracy and lacks scientific merit. This notion lays the basis of theory comparison as well: the progressivity of a research program is represented by its ability to both account for existing refutations and *also* provide novel opportunity for falsification. It is this picture of science which will form the basis of the remainder of this chapter. We may thus consider both MOND and ΛCDM in the context of their relative progressivities within their respective research programs.

5.2 Is MOND Refuted?

Our primary findings in this work provide a set of constraints which, to the best of our current understanding, are difficult for MOND to account for. Not only is MOND fundamentally flawed in galaxy clusters, but both of the auxiliary hypotheses discussed in this work (MOND+DM and EMOND) prove to be equally falsifiable in clusters of galaxies. Other theoretical extensions of MOND such as GQUMOND [102] and TeVeS [19] similarly fail to account for the clear refutation apparent in galaxy clusters. More telling, our findings in Chapter 3 suggest not only that EMOND and MOND+DM are incompatible with galaxy cluster observations, but also that the hard-core of the research program is inconsistent with the observed dynamics.

Our most significant finding in this respect is the differing asymptotic behavior of the ICM temperature profile for different gravity models. The asymptotic behavior of MONDian gravity is fixed by its hard-core and thus implies that the constraints described in Section 3.1 pose serious difficulties to the research program.

When considered in conjunction with MOND's continued inability to convincingly account for the observed dynamics of the Bullet Cluster [42], the outlook seems dire for the MOND paradigm. The early progressivity of the paradigm, as exemplified by its successes in galaxies, appears to have encountered a near unassailable road-block in galaxy clusters. With the first analyses of the Bullet Cluster approaching the 20 year mark and hydrostatic mass reconstruction techniques becoming ever more refined, it appears that this lack of progressivity is both persistent and consequential. Attempts at positing a novel auxiliary hypothesis capable of accounting for the observed dynamics of galaxy clusters has universally led to poorly constrained models with a plethora of free parameters and little fidelity with the real world. In this sense, it seems a reasonable assertion that MOND is refuted by the work presented here and other related constraints in the literature.

While it is seemingly unlikely, there may yet be some avenues by which to resolve these issues in a purely theoretical capacity. The lack of an accepted, relativistic MOND theory (there are many competing candidates for such a distinction) suggests that, if MOND were correct, our classical theory is only an asymptotic manifestation of a deeper theory. Thus, such a relativistic theory may emerge which succeeds in altering the dynamics in clusters of galaxies. More probable is the potential for a modified hard-core which is able to surpass MOND's refutations. Clearly, the results presented in this work are universally predicated on the basic hard-core of MOND and therefore make no assertions regarding the validity of other modified gravity theories. The evaluation of non-MONDian modified gravity theories is beyond the scope of this work; however, it is noteworthy that work continues to find such theories which

might unify the success of MOND on galactic scales with the observed dynamics of galaxy clusters.

5.3 Is MOND Correct?

Having now painted a damning picture of MOND in clusters of galaxies, it is worthwhile to also discuss its successes and their role in our evaluation of the paradigm. The MONDian paradigm has, for many decades now, been highly progressive on the scale of galaxies. For instance, its novel prediction of the Baryonic Tully-Fisher Relation [BTFR; 93] (see, e.g., Merritt [94] for a derivation) as an immediate consequence of the programme's hard-core remains an intriguing success of the theory. This is particularly true when one acknowledges that, in the 40 years since MOND's inception, it has been a continuous struggle to incorporate the BTFR into ΛCDM. Modern (magneto)hydrodynamics simulations of structure formation have been able to reproduce the BTFR, but only after implementing sub-grid models of feedback processes [107, 60, 4, 142]. In fact, the (B)TFR is commonly used as a calibration mechanism for these models. In holding ΛCDM to the same standard as MOND, we must therefore acknowledge that ΛCDM lacks progressivity in explaining the BTFR. Nonetheless, the BTFR is not a refutation of ΛCDM; feedback processes are, while somewhat *ad hoc*, an entirely legitimate auxiliary hypothesis for the fidelity of ΛCDM.

More recently, several bold tests of the MOND paradigm have found supporting evidence for the paradigm. Tests of the EFE [39, 38] indicate a significant divergence from the expected strong-equivalence of general relativity—a result necessary for the hard-core of MOND to be self-consistent. It should be noted that recent examinations of the EFE in clusters of galaxies indicates that these results do not hold in those systems [53]. Direct tests of MOND phenomenology using wide-binaries have recently become the gold-standard for testing MOND; however, current results are mixed.

Results from Hernandez [64] and Chae [37] both indicate a breakdown of GR in the lower acceleration regime; however, Banik et al. [14] found significant evidence in favor of GR when performing a similar analysis.

In considering all of these disparate evidences, any interpretation leads to intriguing questions. If MOND is accepted, then its persistent failures in galaxy clusters must be resolved; an undertaking which may require the emergence of novel physics. This work has shown that there are many strong tests of MOND phenomenology (and its extensions) in galaxy clusters. Moving forward, these must be accounted for by any auxiliary hypothesis of the MOND paradigm. Further work is necessary to fully characterize these results in light of non-thermal pressure sources and non-standard geometries; however, it is unlikely that such modifications would successfully reach fidelity with our constraints.

If ΛCDM is accepted, then one must question why MOND gets so many things right. The ability of MOND to predict, *a priori* unexpected in ΛCDM, phenomena which appear to be consistent with observation suggests an (as yet unknown) connection between these theories. The *ad hoc* nature of feedback models and their reliance on validation via fine-tuned numerical simulations, while not a methodological fault, cannot then be used as support for ΛCDM in a progressive way. Thus, an improved understanding of the underlying physics of feedback must point to a mechanism for the emergence of the BTFR. Similar arguments also apply to the dynamics of wide-binaries. In each case, a better understanding of both MOND and ΛCDM may be instrumental in the discovery and characterization of novel physics.

5.4 Moving Forward

In light of the previous sections and the findings of this work, it is natural to ask how to proceed further along these lines of questioning. In this case, the answer is

certainly dependent on the physicist and their personal evaluation of the available facts. For the physicist who is comfortable enough with the findings presented here and in other works to simply dismiss the MONDian paradigm, a few questions remain which must be confronted. The most important of these is to ascertain why MOND gets anything right at all. Disparate evidences like the BTFR, RAR, and apparent breakdown of the strong equivalence principle must all be readily explained by the ΛCDM paradigm in such a way as to preserve the progressivity of the paradigm in regard to those questions. Doing so appears to be somewhat non-trivial: many papers have emerged showing ΛCDM to be consistent with the RAR [e.g. 71], but rely on somewhat *ad hoc* models of stellar feedback to achieve the simulated result. Similarly, the BTFR is widely used as a calibration criterion for cosmological simulation sub-grid physics models [141, 87]. By no means does this mean that these evidences are invalid; however, the reliance of ΛCDM on indirect and model dependent tests of these observations is a sub-optimal approach to falsification. Recognizing this, the heuristic of ΛCDM should include efforts to characterize and explain these effects from first principles and to determine viable observational tests to confirm their legitimacy without relying on numerical simulation. Doing so is certainly a challenging task for the astronomical community, but seems a necessary step to solidify the arguments against a MONDian interpretation.

For the physicist who is dissatisfied by the arguments presented in this work, and by other arguments against the MOND paradigm, there are similarly many avenues; however, each presents a greater burden of evidence than might be demanded by the ΛCDM heuristic. For MOND to rebuke its criticisms, one of two things must be true: either our current models of the universe and the systems therein is fundamentally flawed on a scale which might account for the manifest failures of MOND or MOND is an asymptotic manifestation of a more fundamental theory. In either case, the task ahead of the MOND paradigm and it's practitioners is a difficult one.

With the emergence of precision astronomy over the past 50 years, it seems increasingly unlikely that systemic uncertainties could account for discrepancy on the scale of those faced by MOND. Novel criticisms of MOND in galactic and stellar observations [e.g. 73, 74, 70, 14] (which were previously its most successful regimes) continue to undermine the most encouraging aspect of MOND: its combined simplicity and generality in galaxies. On the cluster scale, the chance for systematic explanations is somewhat more promising but still highly unlikely. Our findings, in keeping with those of Eckert et al. [48], indicates that non-thermal pressure cannot account for the scale of the observed discrepancy. Furthermore, MOND has never been applied convincingly to merging clusters like the Bullet Cluster [42], which poses perhaps the best argument against the paradigm.

Perhaps the more plausible option, in light of the mounting observational evidence, is that of a deeper theory than MOND. While there has been widespread work in the MOND paradigm to suggest such theories, both classical [e.g. 65, 102, 148] and relativistic [e.g. 19, 128, 108, 130, 98, etc.], the corresponding work to constrain, predict, and attempt falsification is decidedly lacking. Due to their relatively simple mathematics, the classical extensions have received greater attention (as exemplified by this work); however, the implications of the various relativistic extensions are widely debated and difficult to test. In light of this, one of the most critical aspects of a progressive MONDian paradigm will be the emergence, and rigorous testing of a widely accepted MONDian alternative to general relativity. Without such a theory, it is difficult to evaluate the MONDian paradigm's validity in scales larger than that of galaxies.

Chapter 6

Conclusion

In this work, we have presented a series of constraints for MONDian gravity theories in relaxed galaxy clusters and in mergers of galaxy clusters. Taken together with the existing literature, these constraints further compound the issues faced by the MONDian paradigm in clusters of galaxies. Our findings illustrate that, for several promising auxiliary hypotheses, the emergent challenges in galaxy clusters persist and can continue to play a role in constraining further theoretical development of MOND; even when said theory can consistently reproduce the dynamical mass of such systems. More work is necessary to fully characterize the behavior of these constraints in systems which are not in the idealized state of hydrostatic equilibrium; however, such corrections should only constrain minor systematics on the order of 10%. In testing these constraints on a well characterized system of such clusters, we show very clearly that both of the auxiliary hypotheses considered are inconsistent with our constraints. Additional dynamical constraints were also illustrated in systems which are not dynamically relaxed. These findings appear to be similarly in contention with observations; however, further refinement of these arguments is necessary to entirely characterize the degree to which this is the case. Our findings strongly favor the ΛCDM model over any of the MONDian flavors discussed and lays out a clear

roadmap for the further theoretical issues which must be resolved in future iterations of the MOND paradigm.

Bibliography

[1] C. E. Aalseth, P. Barbeau, N. Bowden, B. Cabrera-Palmer, J. Colaresi, J. Collar, S. Dazeley, P. De Lurgio, J. E. Fast, N. Fields, et al. Results from a search for light-mass dark matter with a p-type point contact germanium detector. *Physical Review Letters*, 106(13):131301, 2011.

[2] C. E. Aalseth, P. Barbeau, J. Colaresi, J. Collar, J. D. Leon, J. E. Fast, N. Fields, T. W. Hossbach, M. E. Keillor, J. D. Kephart, et al. Search for an annual modulation in a p-type point contact germanium dark matter detector. *Physical Review Letters*, 107(14):141301, 2011.

[3] M. G. Abadi, B. Moore, and R. G. Bower. Ram pressure stripping of spiral galaxies in clusters. *Monthly Notices of the Royal Astronomical Society*, 308(4): 947–954, 1999.

[4] O. Agertz and A. V. Kravtsov. On the interplay between star formation and feedback in galaxy formation simulations. *The Astrophysical Journal*, 804(1): 18, 2015.

[5] A. Aguirre, J. Schaye, and E. Quataert. Problems for modified newtonian dynamics in clusters and the lyα forest? *The Astrophysical Journal*, 561(2): 550, 2001.

[6] H. Akamatsu, R. van Weeren, G. Ogrean, H. Kawahara, A. Stroe, D. Sobral, M. Hoeft, H. Röttgering, M. Brüggen, and J. Kaastra. Suzaku x-ray study of the double radio relic galaxy cluster ciza j2242. 8+ 5301. *Astronomy & Astrophysics*, 582:A87, 2015.

[7] P. Alfeld. A trivariate clough—tocher scheme for tetrahedral data. *Computer Aided Geometric Design*, 1(2):169–181, 1984.

[8] G. Angloher, A. Bento, C. Bucci, L. Canonica, A. Erb, F. von Feilitzsch, N. F. Iachellini, P. Gorla, A. Gütlein, D. Hauff, et al. Results on low mass wimps using an upgraded cresst-ii detector. *The European Physical Journal C*, 74(12): 1–6, 2014.

[9] G. W. Angus. Is an 11 ev sterile neutrino consistent with clusters, the cosmic microwave background and modified newtonian dynamics? *Monthly Notices of the Royal Astronomical Society*, 394(1):527–532, 2009.

[10] G. W. Angus, A. Diaferio, B. Famaey, and K. J. van der Heyden. Cosmological simulations in mond: the cluster scale halo mass function with light sterile neutrinos. *Monthly Notices of the Royal Astronomical Society*, 436(1):202–211, 2013.

[11] D. E. Applegate, A. Mantz, S. W. Allen, A. von der Linden, R. G. Morris, S. Hilbert, P. L. Kelly, D. L. Burke, H. Ebeling, D. A. Rapetti, and R. W. Schmidt. Cosmology and astrophysics from relaxed galaxy clusters - IV. Robustly calibrating hydrostatic masses with weak lensing. MNRAS, 457(2):1522–1534, Apr. 2016. doi: 10.1093/mnras/stw005.

[12] F. Bacon. *Novum organum*. Clarendon press, 1878.

[13] E. A. Baltz, P. Marshall, and M. Oguri. Analytic models of plausible gravitational lens potentials. *Journal of Cosmology and Astroparticle Physics*, 2009 (01):015, 2009.

[14] I. Banik, C. Pittordis, W. Sutherland, B. Famaey, R. Ibata, S. Mieske, and H. Zhao. Strong constraints on the gravitational law from gaia dr3 wide binaries. *Monthly Notices of the Royal Astronomical Society*, 527(3):4573–4615, 2024.

[15] N. Battaglia, J. R. Bond, C. Pfrommer, and J. L. Sievers. On the Cluster Physics of Sunyaev-Zel'dovich and X-Ray Surveys. I. The Influence of Feedback, Non-thermal Pressure, and Cluster Shapes on Y-M Scaling Relations. ApJ, 758 (2):74, Oct. 2012. doi: 10.1088/0004-637X/758/2/74.

[16] K. Begeman, A. Broeils, and R. Sanders. Extended rotation curves of spiral galaxies: Dark haloes and modified dynamics. *Monthly Notices of the Royal Astronomical Society*, 249(3):523–537, 1991.

[17] J. Bekenstein and M. Milgrom. Does the missing mass problem signal the breakdown of Newtonian gravity? ApJ, 286:7–14, Nov. 1984. doi: 10.1086/162570.

[18] J. Bekenstein and M. Milgrom. Does the missing mass problem signal the breakdown of newtonian gravity? *Astrophysical Journal, Part 1 (ISSN 0004-637X), vol. 286, Nov. 1, 1984, p. 7-14. Research supported by the MINERVA Foundation.*, 286:7–14, 1984.

[19] J. D. Bekenstein. Relativistic gravitation theory for the modified newtonian dynamics paradigm. *Physical Review D*, 70(8):083509, 2004.

[20] J. S. Bennett and D. Sijacki. A disturbing FABLE of mergers, feedback, turbulence, and mass biases in simulated galaxy clusters. MNRAS, 514(1):313–328, July 2022. doi: 10.1093/mnras/stac1216.

[21] L. Berezhiani and J. Khoury. Theory of dark matter superfluidity. *Physical Review D*, 92(10):103510, 2015.

[22] J. Berteaud, C. Francesca, J. Iguaz, P. D. Serpico, and T. Siegert. Primordial black holes as dark matter candidates: Constraints from the diffuse mev emission. In *EPJ Web of Conferences*, volume 280, page 07003. EDP Sciences, 2023.

[23] E. Bertschinger. Simulations of structure formation in the universe. *Annual Review of Astronomy and Astrophysics*, 36(1):599–654, 1998.

[24] V. Biffi, S. Borgani, G. Murante, E. Rasia, S. Planelles, G. L. Granato, C. Ragone-Figueroa, A. M. Beck, M. Gaspari, and K. Dolag. On the nature of hydrostatic equilibrium in galaxy clusters. *The Astrophysical Journal*, 827(2): 112, 2016.

[25] A. Bonafede, L. Feretti, M. Murgia, F. Govoni, G. Giovannini, D. Dallacasa, K. Dolag, and G. B. Taylor. The coma cluster magnetic field from faraday rotation measures. *Astronomy & Astrophysics*, 513:A30, 2010.

[26] H. Bourdin, P. Mazzotta, M. Markevitch, S. Giacintucci, and G. Brunetti. Shock Heating of the Merging Galaxy Cluster A521. ApJ, 764(1):82, Feb. 2013. doi: 10.1088/0004-637X/764/1/82.

[27] H. Bourdin, P. Mazzotta, M. Markevitch, S. Giacintucci, and G. Brunetti. Shock heating of the merging galaxy cluster a521. *The Astrophysical Journal*, 764(1): 82, 2013.

[28] R. Broucke. Notes on the central force rn. *Astrophysics and Space Science*, 72: 33–53, 1980.

[29] G. Brunetti and T. W. Jones. Cosmic rays in galaxy clusters and their non-thermal emission. *International Journal of Modern Physics D*, 23(04):1430007, 2014.

[30] D. A. Buote and P. J. Humphrey. Spherically averaging ellipsoidal galaxy clusters in x-ray and sunyaev–zel'dovich studies–i. analytical relations. *Monthly Notices of the Royal Astronomical Society*, 420(2):1693–1705, 2012.

[31] D. A. Buote and P. J. Humphrey. Spherically averaging ellipsoidal galaxy clusters in x-ray and sunyaev–zel'dovich studies–ii. biases. *Monthly Notices of the Royal Astronomical Society*, 421(2):1399–1420, 2012.

[32] R. E. Carlson and F. N. Fritsch. Monotone Piecewise Bicubic Interpolation. *SIAM Journal on Numerical Analysis*, 22(2):386–400, Apr. 1985. doi: 10.1137/0722023.

[33] B. Carr and F. Kühnel. Primordial black holes as dark matter: recent developments. *Annual Review of Nuclear and Particle Science*, 70:355–394, 2020.

[34] B. Carr, K. Kohri, Y. Sendouda, and J. Yokoyama. New cosmological constraints on primordial black holes. *Physical Review D*, 81(10):104019, 2010.

[35] A. Cavaliere and R. Fusco-Femiano. X-rays from hot plasma in clusters of galaxies. *Astronomy and Astrophysics, vol. 49, no. 1, May 1976, p. 137-144.*, 49:137–144, 1976.

[36] K.-H. Chae. Breakdown of the Newton-Einstein Standard Gravity at Low Acceleration in Internal Dynamics of Wide Binary Stars. ApJ, 952(2):128, Aug. 2023. doi: 10.3847/1538-4357/ace101.

[37] K.-H. Chae. Breakdown of the newton–einstein standard gravity at low acceleration in internal dynamics of wide binary stars. *The Astrophysical Journal*, 952(2):128, 2023.

[38] K.-H. Chae, F. Lelli, H. Desmond, S. S. McGaugh, P. Li, and J. M. Schombert. Testing the strong equivalence principle: detection of the external field effect in rotationally supported galaxies. *The Astrophysical Journal*, 904(1):51, 2020.

[39] K.-H. Chae, H. Desmond, F. Lelli, S. S. McGaugh, and J. M. Schombert. Testing the strong equivalence principle. ii. relating the external field effect in galaxy rotation curves to the large-scale structure of the universe. *The Astrophysical Journal*, 921(2):104, 2021.

[40] A. Chalmers. *What is this thing called science?* McGraw-Hill Education (UK), 2013.

[41] D. Clowe, A. Gonzalez, and M. Markevitch. Weak-lensing mass reconstruction of the interacting cluster 1e 0657–558: Direct evidence for the existence of dark matter. *The Astrophysical Journal*, 604(2):596, 2004.

[42] D. Clowe, M. Bradač, A. H. Gonzalez, M. Markevitch, S. W. Randall, C. Jones, and D. Zaritsky. A direct empirical proof of the existence of dark matter. *The Astrophysical Journal*, 648(2):L109, 2006.

[43] R. H. Cyburt, B. D. Fields, K. A. Olive, and T.-H. Yeh. Big bang nucleosynthesis: Present status. *Reviews of Modern Physics*, 88(1):015004, 2016.

[44] E. Di Valentino, O. Mena, S. Pan, L. Visinelli, W. Yang, A. Melchiorri, D. F. Mota, A. G. Riess, and J. Silk. In the realm of the hubble tension—a review of solutions. *Classical and Quantum Gravity*, 38(15):153001, 2021.

[45] B. Diemer and M. Joyce. An Accurate Physical Model for Halo Concentrations. ApJ, 871(2):168, Feb. 2019. doi: 10.3847/1538-4357/aafad6.

[46] S. Dupourqué, N. Clerc, E. Pointecouteau, D. Eckert, S. Ettori, and F. Vazza. Investigating the turbulent hot gas in x-cop galaxy clusters. *arXiv preprint arXiv:2303.15102*, 2023.

[47] D. Eckert, V. Ghirardini, S. Ettori, E. Rasia, V. Biffi, E. Pointecouteau, M. Rossetti, S. Molendi, F. Vazza, F. Gastaldello, et al. Non-thermal pressure support in x-cop galaxy clusters. *Astronomy & Astrophysics*, 621:A40, 2019.

[48] D. Eckert, S. Ettori, E. Pointecouteau, R. van der Burg, and S. Loubser. The gravitational field of x-cop galaxy clusters. *Astronomy & Astrophysics*, 662: A123, 2022.

[49] T. A. Ensslin, P. L. Biermann, P. P. Kronberg, and X.-P. Wu. Cosmic-ray protons and magnetic fields in clusters of galaxies and their cosmological consequences. *The Astrophysical Journal*, 477(2):560, 1997.

[50] L. Feretti, G. Giovannini, F. Govoni, and M. Murgia. Clusters of galaxies: observational properties of the diffuse radio emission. A&A Rev., 20:54, May 2012. doi: 10.1007/s00159-012-0054-z.

[51] C. Ferrari, F. Govoni, S. Schindler, A. Bykov, and Y. Rephaeli. Observations of extended radio emission in clusters. *Clusters of Galaxies: Beyond the Thermal View*, pages 93–118, 2008.

[52] W. Forman, C. Jones, M. Markevitch, S. Murray, and L. Van Speybroeck. Chandra sample of nearby relaxed galaxy clusters: Mass, gas fraction, and mass-temperature relation. *The Astrophysical Journal*, 640(2):691, 2006.

[53] J. Freundlich, B. Famaey, P.-A. Oria, M. Bílek, O. Müller, and R. Ibata. Probing the radial acceleration relation and the strong equivalence principle with the coma cluster ultra-diffuse galaxies. *Astronomy & Astrophysics*, 658:A26, 2022.

[54] F. N. Fritsch and R. E. Carlson. Monotone Piecewise Cubic Interpolation. *SIAM Journal on Numerical Analysis*, 17(2):238–246, Apr. 1980. doi: 10.1137/0717021.

[55] M. Fukugita, C. Hogan, and P. Peebles. The cosmic baryon budget. *The Astrophysical Journal*, 503(2):518, 1998.

[56] R. Gavazzi. Projection effects in cluster mass estimates: the case of MS2137-23. A&A, 443(3):793–804, Dec. 2005. doi: 10.1051/0004-6361:20053166.

[57] C. Ge, R.-Y. Liu, M. Sun, H. Yu, L. Rudnick, J. Eilek, F. Owen, S. Dasadia, M. Rossetti, M. Markevitch, T. E. Clarke, T. W. Jones, S. Ghizzardi, T. Venturi, A. Finoguenov, and D. Eckert. Chandra and XMM-Newton observations of A2256: cold fronts, merger shocks, and constraint on the IC emission. MNRAS, 497(4):4704–4717, Oct. 2020. doi: 10.1093/mnras/staa2320.

[58] D. Gerbal, F. Durret, M. Lachieze-Rey, and G. Lima-Neto. Analysis of x-ray galaxy clusters in the framework of modified newtonian dynamics. *Astronomy and Astrophysics*, 262:395–400, 1992.

[59] V. Ghirardini, S. Ettori, D. Eckert, S. Molendi, F. Gastaldello, E. Pointecouteau, G. Hurier, and H. Bourdin. The XMM Cluster Outskirts Project (X-COP): Thermodynamic properties of the intracluster medium out to R_{200} in Abell 2319. A&A, 614:A7, June 2018. doi: 10.1051/0004-6361/201731748.

[60] F. Governato, B. Willman, L. Mayer, A. Brooks, G. Stinson, O. Valenzuela, J. Wadsley, and T. Quinn. Forming disc galaxies in λcdm simulations. *Monthly Notices of the Royal Astronomical Society*, 374(4):1479–1494, 2007.

[61] J. E. Gunn and I. Gott, J. Richard. On the Infall of Matter Into Clusters of Galaxies and Some Effects on Their Evolution. ApJ, 176:1, Aug. 1972. doi: 10.1086/151605.

[62] A. V. Gurevich and K. P. Zybin. Large-scale structure of the universe. analytic theory. *Physics-Uspekhi*, 38(7):687, 1995.

[63] X. Hernandez. Internal kinematics of Gaia DR3 wide binaries: anomalous behaviour in the low acceleration regime. *Monthly Notices of the Royal Astronomical Society*, 525(1):1401–1415, 08 2023. ISSN 0035-8711. doi: 10.1093/mnras/stad2306. URL `https://doi.org/10.1093/mnras/stad2306`.

[64] X. Hernandez. Internal kinematics of gaia dr3 wide binaries: anomalous behaviour in the low acceleration regime. *Monthly Notices of the Royal Astronomical Society*, 525(1):1401–1415, 2023.

[65] A. O. Hodson and H. Zhao. Generalizing mond to explain the missing mass in galaxy clusters. *Astronomy & Astrophysics*, 598:A127, 2017.

[66] A. O. Hodson, H. Zhao, J. Khoury, and B. Famaey. Galaxy clusters in the context of superfluid dark matter. *Astronomy & Astrophysics*, 607:A108, 2017.

[67] D. Hodson. Philosophy of science, science and science education. 1985.

[68] S. E. Hong, D. Ryu, H. Kang, and R. Cen. Shock waves and cosmic ray acceleration in the outskirts of galaxy clusters. *The Astrophysical Journal*, 785(2): 133, 2014.

[69] J.-P. Hu and F.-Y. Wang. Hubble tension: the evidence of new physics. *Universe*, 9(2):94, 2023.

[70] R. Ibata, A. Sollima, C. Nipoti, M. Bellazzini, S. C. Chapman, and E. Dalessandro. The Globular Cluster NGC 2419: A Crucible for Theories of Gravity. ApJ, 738(2):186, Sept. 2011. doi: 10.1088/0004-637X/738/2/186.

[71] B. W. Keller and J. W. Wadsley. ΛCDM is Consistent with SPARC Radial Acceleration Relation. ApJ, 835(1):L17, Jan. 2017. doi: 10.3847/2041-8213/835/1/L17.

[72] S. M. Kent. Dark matter in spiral galaxies. ii-galaxies with hi rotation curves. *The Astronomical Journal*, 93:816–832, 1987.

[73] M. Khelashvili, A. Rudakovskyi, and S. Hossenfelder. SPARC galaxies prefer Dark Matter over MOND. *arXiv e-prints*, art. arXiv:2401.10202, Jan. 2024. doi: 10.48550/arXiv.2401.10202.

[74] A. Klypin and F. Prada. Testing Gravity With Motion of Satellites Around Galaxies: Newtonian Gravity Against Modified Newtonian Dynamics. ApJ, 690(2):1488–1496, Jan. 2009. doi: 10.1088/0004-637X/690/2/1488.

[75] T. S. Kuhn. *The structure of scientific revolutions*, volume 962. University of Chicago press Chicago, 1997.

[76] A. Kulier, B. Poggianti, S. Tonnesen, R. Smith, A. Ignesti, N. Akerman, A. Marasco, B. Vulcani, A. Moretti, and A. Wolter. Ram Pressure Stripping in the EAGLE Simulation. ApJ, 954(2):177, Sept. 2023. doi: 10.3847/1538-4357/aceda3.

[77] I. Labbé, P. van Dokkum, E. Nelson, R. Bezanson, K. A. Suess, J. Leja, G. Brammer, K. Whitaker, E. Mathews, M. Stefanon, et al. A population of red candidate massive galaxies˜ 600 myr after the big bang. *Nature*, pages 1–2, 2023.

[78] I. Lakatos. Falsification and the methodology of scientific research programmes. In *Philosophy, Science, and History*, pages 89–94. Routledge, 2014.

[79] L. D. Landau. *The classical theory of fields*, volume 2. Elsevier, 2013.

[80] T. Lasserre and E. Collaboration. Not enough stellar mass machos in the galactic halo. *arXiv preprint astro-ph/0002253*, 2000.

[81] E. T. Lau, A. V. Kravtsov, and D. Nagai. Residual gas motions in the intracluster medium and bias in hydrostatic measurements of mass profiles of clusters. *The Astrophysical Journal*, 705(2):1129, 2009.

[82] T. Lebeau, J. G. Sorce, N. Aghanim, E. Hernández-Martínez, and K. Dolag. Mass bias in clusters of galaxies: Projection effects on the case study of Virgo replica. *arXiv e-prints*, art. arXiv:2310.02326, Oct. 2023. doi: 10.48550/arXiv.2310.02326.

[83] T. Lebeau, J. G. Sorce, N. Aghanim, E. Hernández-Martínez, and K. Dolag. Mass bias in clusters of galaxies: Projection effects on the case study of Virgo replica. A&A, 682:A157, Feb. 2024. doi: 10.1051/0004-6361/202347511.

[84] F. Lelli, S. S. McGaugh, and J. M. Schombert. The small scatter of the baryonic tully–fisher relation. *The Astrophysical Journal Letters*, 816(1):L14, 2016.

[85] G. Macario, M. Markevitch, S. Giacintucci, G. Brunetti, T. Venturi, and S. S. Murray. A Shock Front in the Merging Galaxy Cluster A754: X-ray and Radio Observations. ApJ, 728(2):82, Feb. 2011. doi: 10.1088/0004-637X/728/2/82.

[86] M. Manolopoulou and M. Plionis. Galaxy cluster's rotation. *Monthly Notices of the Royal Astronomical Society*, page stw2870, 2016.

[87] F. Marinacci, M. Vogelsberger, R. Pakmor, P. Torrey, V. Springel, L. Hernquist, D. Nelson, R. Weinberger, A. Pillepich, J. Naiman, and S. Genel. First results from the IllustrisTNG simulations: radio haloes and magnetic fields. MNRAS, 480(4):5113–5139, Nov. 2018. doi: 10.1093/mnras/sty2206.

[88] M. Markevitch and A. Vikhlinin. Merger shocks in galaxy clusters a665 and a2163 and their relation to radio halos. *The Astrophysical Journal*, 563(1):95, 2001.

[89] M. Markevitch, A. Gonzalez, L. David, A. Vikhlinin, S. Murray, W. Forman, C. Jones, and W. Tucker. A textbook example of a bow shock in the merging galaxy cluster 1e 0657–56. *The Astrophysical Journal*, 567(1):L27, 2002.

[90] M. Markevitch, A. H. Gonzalez, D. Clowe, A. Vikhlinin, W. Forman, C. Jones, S. Murray, and W. Tucker. Direct Constraints on the Dark Matter Self-Interaction Cross Section from the Merging Galaxy Cluster 1E 0657-56. ApJ, 606(2):819–824, May 2004. doi: 10.1086/383178.

[91] S. McGaugh and M. Milgrom. Andromeda dwarfs in light of modified newtonian dynamics. *The Astrophysical Journal*, 766(1):22, 2013.

[92] S. McGaugh and M. Milgrom. Andromeda dwarfs in light of mond. ii. testing prior predictions. *The Astrophysical Journal*, 775(2):139, 2013.

[93] S. S. McGaugh. The baryonic tully–fisher relation of gas-rich galaxies as a test of λcdm and mond. *The Astronomical Journal*, 143(2):40, 2012.

[94] D. Merritt. *A philosophical approach to MOND: Assessing the Milgromian research program in cosmology.* Cambridge University Press, 2020.

[95] M. Milgrom. A modification of the newtonian dynamics as a possible alternative to the hidden mass hypothesis. *Astrophysical Journal, Part 1 (ISSN 0004-637X), vol. 270, July 15, 1983, p. 365-370. Research supported by the US-Israel Binational Science Foundation.*, 270:365–370, 1983.

[96] M. Milgrom. A modification of the newtonian dynamics-implications for galaxies. *The Astrophysical Journal*, 270:371–383, 1983.

[97] M. Milgrom. Marriage à-la-mond: Baryonic dark matter in galaxy clusters and the cooling flow puzzle. *New Astronomy Reviews*, 51(10-12):906–915, 2008.

[98] M. Milgrom. Bimetric mond gravity. *Physical Review D*, 80(12):123536, 2009.

[99] M. Milgrom. Quasi-linear formulation of MOND. MNRAS, 403(2):886–895, Apr. 2010. doi: 10.1111/j.1365-2966.2009.16184.x.

[100] M. Milgrom. Quasi-linear formulation of mond. *Monthly Notices of the Royal Astronomical Society*, 403(2):886–895, 2010.

[101] M. Milgrom. General virial theorem for modified-gravity MOND. Phys. Rev. D, 89(2):024016, Jan. 2014. doi: 10.1103/PhysRevD.89.024016.

[102] M. Milgrom. Generalizations of quasilinear mond (qumond). *arXiv preprint arXiv:2305.01589*, 2023.

[103] K. Nelson, D. H. Rudd, L. Shaw, and D. Nagai. Evolution of the merger-induced hydrostatic mass bias in galaxy clusters. *The Astrophysical Journal*, 751(2):121, 2012.

[104] K. Nelson, E. T. Lau, and D. Nagai. Hydrodynamic simulation of non-thermal pressure profiles of galaxy clusters. *The Astrophysical Journal*, 792(1):25, 2014.

[105] S. Nojiri and S. D. Odintsov. Introduction to modified gravity and gravitational alternative for dark energy. *International Journal of Geometric Methods in Modern Physics*, 4(01):115–145, 2007.

[106] G. Ogrean, M. Brüggen, R. van Weeren, H. Röttgering, A. Simionescu, M. Hoeft, and J. Croston. Multiple density discontinuities in the merging galaxy cluster ciza j2242. 8+ 5301. *Monthly Notices of the Royal Astronomical Society*, 440(4):3416–3425, 2014.

[107] T. Okamoto, V. R. Eke, C. S. Frenk, and A. Jenkins. Effects of feedback on the morphology of galaxy discs. *Monthly Notices of the Royal Astronomical Society*, 363(4):1299–1314, 2005.

[108] G. J. Olmo. Palatini Approach to Modified Gravity:. f(R) Theories and Beyond. *International Journal of Modern Physics D*, 20(4):413–462, Jan. 2011. doi: 10.1142/S0218271811018925.

[109] F. A. Pearce, S. T. Kay, D. J. Barnes, R. G. Bower, and M. Schaller. Hydrostatic mass estimates of massive galaxy clusters: a study with varying hydrodynamics flavours and non-thermal pressure support. *Monthly Notices of the Royal Astronomical Society*, 491(2):1622–1642, 2020.

[110] L. Perivolaropoulos and F. Skara. Challenges for λcdm: An update. *New Astronomy Reviews*, page 101659, 2022.

[111] Planck Collaboration, N. Aghanim, Y. Akrami, M. Ashdown, J. Aumont, C. Baccigalupi, M. Ballardini, A. J. Banday, R. B. Barreiro, N. Bartolo, S. Basak, R. Battye, K. Benabed, J. P. Bernard, M. Bersanelli, P. Bielewicz, J. J. Bock, J. R. Bond, J. Borrill, F. R. Bouchet, F. Boulanger, M. Bucher, C. Burigana, R. C. Butler, E. Calabrese, J. F. Cardoso, J. Carron, A. Challinor, H. C. Chiang, J. Chluba, L. P. L. Colombo, C. Combet, D. Contreras, B. P. Crill, F. Cuttaia, P. de Bernardis, G. de Zotti, J. Delabrouille, J. M. Delouis, E. Di Valentino, J. M. Diego, O. Doré, M. Douspis, A. Ducout, X. Dupac, S. Dusini, G. Efstathiou, F. Elsner, T. A. Enßlin, H. K. Eriksen, Y. Fantaye, M. Farhang, J. Fergusson, R. Fernandez-Cobos, F. Finelli, F. Forastieri, M. Frailis, A. A.

Fraisse, E. Franceschi, A. Frolov, S. Galeotta, S. Galli, K. Ganga, R. T. Génova-Santos, M. Gerbino, T. Ghosh, J. González-Nuevo, K. M. Górski, S. Gratton, A. Gruppuso, J. E. Gudmundsson, J. Hamann, W. Handley, F. K. Hansen, D. Herranz, S. R. Hildebrandt, E. Hivon, Z. Huang, A. H. Jaffe, W. C. Jones, A. Karakci, E. Keihänen, R. Keskitalo, K. Kiiveri, J. Kim, T. S. Kisner, L. Knox, N. Krachmalnicoff, M. Kunz, H. Kurki-Suonio, G. Lagache, J. M. Lamarre, A. Lasenby, M. Lattanzi, C. R. Lawrence, M. Le Jeune, P. Lemos, J. Lesgourgues, F. Levrier, A. Lewis, M. Liguori, P. B. Lilje, M. Lilley, V. Lindholm, M. López-Caniego, P. M. Lubin, Y. Z. Ma, J. F. Macías-Pérez, G. Maggio, D. Maino, N. Mandolesi, A. Mangilli, A. Marcos-Caballero, M. Maris, P. G. Martin, M. Martinelli, E. Martínez-González, S. Matarrese, N. Mauri, J. D. McEwen, P. R. Meinhold, A. Melchiorri, A. Mennella, M. Migliaccio, M. Millea, S. Mitra, M. A. Miville-Deschênes, D. Molinari, L. Montier, G. Morgante, A. Moss, P. Natoli, H. U. Nørgaard-Nielsen, L. Pagano, D. Paoletti, B. Partridge, G. Patanchon, H. V. Peiris, F. Perrotta, V. Pettorino, F. Piacentini, L. Polastri, G. Polenta, J. L. Puget, J. P. Rachen, M. Reinecke, M. Remazeilles, A. Renzi, G. Rocha, C. Rosset, G. Roudier, J. A. Rubiño-Martín, B. Ruiz-Granados, L. Salvati, M. Sandri, M. Savelainen, D. Scott, E. P. S. Shellard, C. Sirignano, G. Sirri, L. D. Spencer, R. Sunyaev, A. S. Suur-Uski, J. A. Tauber, D. Tavagnacco, M. Tenti, L. Toffolatti, M. Tomasi, T. Trombetti, L. Valenziano, J. Valiviita, B. Van Tent, L. Vibert, P. Vielva, F. Villa, N. Vittorio, B. D. Wandelt, I. K. Wehus, M. White, S. D. M. White, A. Zacchei, and A. Zonca. Planck 2018 results. VI. Cosmological parameters. A&A, 641:A6, Sept. 2020. doi: 10.1051/0004-6361/201833910.

[112] S. Planelles and V. Quilis. Galaxy cluster mergers. *Monthly Notices of the Royal Astronomical Society*, 399(1):410–424, 2009.

[113] E. Pointecouteau and J. Silk. New constraints on modified newtonian dynamics from galaxy clusters. *Monthly Notices of the Royal Astronomical Society*, 364 (2):654–658, 2005.

[114] K. R. Popper. *All life is problem solving.* Psychology Press, 1999.

[115] E. Roediger and G. Hensler. Ram pressure stripping of disk galaxies-from high to low density environments. *Astronomy & Astrophysics*, 433(3):875–895, 2005.

[116] R. Rosner and W. Tucker. On magnetic fields, heating and thermal conduction in halos, and the suppression of cooling flows. *The Astrophysical Journal*, 338: 761–769, 1989.

[117] V. C. Rubin and W. K. Ford Jr. Rotation of the andromeda nebula from a spectroscopic survey of emission regions. *The Astrophysical Journal*, 159:379, 1970.

[118] B. Ryden. *Introduction to cosmology.* Cambridge University Press, 2017.

[119] C. L. Sarazin. X-ray emission from clusters of galaxies. *Reviews of Modern Physics*, 58(1):1, 1986.

[120] C. L. Sarazin. The physics of cluster mergers. *Merging Processes in Galaxy Clusters*, pages 1–38, 2002.

[121] K. C. Sarkar, A. Dey, and P. Sharma. Deprojection of X-ray data in galaxy clusters: confronting simulations with observations. MNRAS, 516(1):992–1007, Oct. 2022. doi: 10.1093/mnras/stac2296.

[122] V. Savchenko, C. Ferrigno, E. Kuulkers, A. Bazzano, E. Bozzo, S. Brandt, J. Chenevez, T.-L. Courvoisier, R. Diehl, A. Domingo, et al. Integral detection of the first prompt gamma-ray signal coincident with the gravitational-wave event gw170817. *The Astrophysical Journal Letters*, 848(2):L15, 2017.

[123] P. Schneider. *Extragalactic astronomy and cosmology: an introduction*, volume 146. Springer, 2006.

[124] P. Schuecker, A. Finoguenov, F. Miniati, H. Böhringer, and U. G. Briel. Probing turbulence in the Coma galaxy cluster. A&A, 426:387–397, Nov. 2004. doi: 10.1051/0004-6361:20041039.

[125] T. W. Shimwell, M. Markevitch, S. Brown, L. Feretti, B. M. Gaensler, M. Johnston-Hollitt, C. Lage, and R. Srinivasan. Another shock for the Bullet cluster, and the source of seed electrons for radio relics. MNRAS, 449(2): 1486–1494, May 2015. doi: 10.1093/mnras/stv334.

[126] C. Skordis and T. Zlosnik. Geometry of modified newtonian dynamics. *Physical Review D*, 85(4):044044, 2012.

[127] C. Skordis and T. Złośnik. Gravitational alternatives to dark matter with tensor mode speed equaling the speed of light. *Physical Review D*, 100(10):104013, 2019.

[128] C. Skordis and T. Złośnik. New relativistic theory for modified newtonian dynamics. *Physical review letters*, 127(16):161302, 2021.

[129] G. P. Smith, P. Mazzotta, N. Okabe, F. Ziparo, S. L. Mulroy, A. Babul, A. Finoguenov, I. G. McCarthy, M. Lieu, Y. M. Bahé, H. Bourdin, A. E. Evrard, T. Futamase, C. P. Haines, M. Jauzac, D. P. Marrone, R. Martino, P. E. May, J. E. Taylor, and K. Umetsu. LoCuSS: Testing hydrostatic equilibrium in galaxy clusters. MNRAS, 456(1):L74–L78, Feb. 2016. doi: 10.1093/mnrasl/slv175.

[130] T. P. Sotiriou and V. Faraoni. f(R) theories of gravity. *Reviews of Modern Physics*, 82(1):451–497, Jan. 2010. doi: 10.1103/RevModPhys.82.451.

[131] V. Springel, C. S. Frenk, and S. D. White. The large-scale structure of the universe. *nature*, 440(7088):1137–1144, 2006.

[132] M. Steffen. A simple method for monotonic interpolation in one dimension. A&A, 239:443–450, Nov. 1990.

[133] J. Svensmark, R. Wojtak, and S. H. Hansen. Effect of asphericity in caustic mass estimates of galaxy clusters. MNRAS, 448(2):1644–1659, Apr. 2015. doi: 10.1093/mnras/stu2686.

[134] P. Tisserand, L. Le Guillou, C. Afonso, J. Albert, J. Andersen, R. Ansari, É. Aubourg, P. Bareyre, J. Beaulieu, X. Charlot, et al. Limits on the macho content of the galactic halo from the eros-2 survey of the magellanic clouds. *Astronomy & Astrophysics*, 469(2):387–404, 2007.

[135] H. M. Tovmassian. The rotation of galaxy clusters. *Astrophysics*, 58(3):328–337, 2015.

[136] R. Van Weeren, F. de Gasperin, H. Akamatsu, M. Brüggen, L. Feretti, H. Kang, A. Stroe, and F. Zandanel. Diffuse radio emission from galaxy clusters. *Space Science Reviews*, 215:1–75, 2019.

[137] F. Vazza, G. Brunetti, A. Kritsuk, R. Wagner, C. Gheller, and M. Norman. Turbulent motions and shocks waves in galaxy clusters simulated with adaptive mesh refinement. A&A, 504(1):33–43, Sept. 2009. doi: 10.1051/0004-6361/200912535.

[138] F. Vazza, M. Angelinelli, T. Jones, D. Eckert, M. Brüggen, G. Brunetti, and C. Gheller. The turbulent pressure support in galaxy clusters revisited. *Monthly Notices of the Royal Astronomical Society: Letters*, 481(1):L120–L124, 2018.

[139] M. A. Verheijen. The ursa major cluster of galaxies. v. hi rotation curve shapes and the tully-fisher relations. *The Astrophysical Journal*, 563(2):694, 2001.

[140] P. Virtanen, R. Gommers, T. E. Oliphant, M. Haberland, T. Reddy, D. Cournapeau, E. Burovski, P. Peterson, W. Weckesser, J. Bright, S. J. van der Walt, M. Brett, J. Wilson, K. J. Millman, N. Mayorov, A. R. J. Nelson, E. Jones, R. Kern, E. Larson, C. J. Carey, İ. Polat, Y. Feng, E. W. Moore, J. VanderPlas, D. Laxalde, J. Perktold, R. Cimrman, I. Henriksen, E. A. Quintero, C. R. Harris, A. M. Archibald, A. H. Ribeiro, F. Pedregosa, P. van Mulbregt, and SciPy 1.0 Contributors. SciPy 1.0: Fundamental Algorithms for Scientific Computing in Python. *Nature Methods*, 17:261–272, 2020. doi: 10.1038/s41592-019-0686-2.

[141] M. Vogelsberger, S. Genel, V. Springel, P. Torrey, D. Sijacki, D. Xu, G. Snyder, D. Nelson, and L. Hernquist. Introducing the Illustris Project: simulating the coevolution of dark and visible matter in the Universe. MNRAS, 444(2):1518–1547, Oct. 2014. doi: 10.1093/mnras/stu1536.

[142] M. Vogelsberger, F. Marinacci, P. Torrey, and E. Puchwein. Cosmological simulations of galaxy formation. *Nature Reviews Physics*, 2(1):42–66, 2020.

[143] C. Vogt and T. A. Enßlin. Measuring the cluster magnetic field power spectra from Faraday rotation maps of Abell 400, Abell 2634 and Hydra A. A&A, 412: 373–385, Dec. 2003. doi: 10.1051/0004-6361:20031434.

[144] B. Vollmer, V. Cayatte, C. Balkowski, and W. Duschl. Ram pressure stripping and galaxy orbits: The case of the virgo cluster. *The Astrophysical Journal*, 561(2):708, 2001.

[145] P. C. Wason. On the failure to eliminate hypotheses in a conceptual task. *Quarterly journal of experimental psychology*, 12(3):129–140, 1960.

[146] T. P. Waterhouse. An introduction to chameleon gravity. *arXiv preprint astro-ph/0611816*, 2006.

[147] S. D. White, C. S. Frenk, and M. Davis. Clustering in a neutrino-dominated universe. *Astrophysical Journal, Part 2-Letters to the Editor (ISSN 0004-637X), vol. 274, Nov. 1, 1983, p. L1-L5.*, 274:L1–L5, 1983.

[148] H. Zhao and B. Famaey. Unifying all mass discrepancies with one effective gravity law? *Physical Review D*, 86(6):067301, 2012.

[149] F. Zwicky. On the masses of nebulae and of clusters of nebulae. *The Astrophysical Journal*, 86:217, 1937.

Appendix A

Non-Physical Correction

One of the most daunting challenges when initializing galaxy cluster models is the frequency with which seemingly innocuous initial profiles lead to catastrophically non-physical galaxy cluster models. The general approach, which before now has always been used, is to simply identify failures on a case by case basis and modify the resulting profiles accordingly. In the case of the `cluster_generator` software, the need for highly general algorithms for cluster building required a more general approach be described. In this chapter, the details of that approach are discussed as are some assorted numerical algorithms which play critical roles in the larger correction algorithm.

A.1 Introduction

In the context of cluster generation, non-physicality may be though of as a mapping problem. Generically, one takes a minimial generating set $s = \{f_i, \cdots, f_j\}$, where each function $f_i : I \to \mathbb{R}$ is a physical quantity represented by a profile on the radial simulation domain I. Each such f_i is implicitly restricted by two criteria: first, it may have a smoothness restriction such that $f_i \in C^{l_i}[I]$ for some l_i and it may also have some structural restriction such as monotonicity, positivity, concavity, etc. In this

picture, generating a fully realized cluster may be thought of as a mapping $\Sigma : s \to S$, where S is the "complete set" $\{f_i, \cdots, f_j, \cdots, f_k\}$ (subscripts indicating labels, not ordinal indices) such that $s \subset S$ and each physical property of the cluster has a corresponding functional realization in S. For s to be considered a valid "generating set" it must have a unique image under Σ. The issue of physicality arises when under Σ, $s \to S$ produces a complete set which is not physically consistent in the sense that the derived profiles fail to meet the structural criteria. It is therefore useful to think of the process of non-physical correction as a (minimally rigorous) optimization problem of finding the closest S' to S such that S' is consistent.

In considering correction as an optimization problem, it may be tempting to continue along the road of abstraction and introduce some sense of a metric and other relevant structures to the sets of allowed s and their mappings; however, it is not clear that such a choice leads to tractable numerics or, in fact, to self-consistent mathematics. Instead, we present the above description of the problem less in the interest of using relevant mathematical methods to approach the problem and instead to frame the decision making which underlies the design of the correction algorithm.

A.2 Correcting Non-Physical Regions

As it turns out, the key result which underpins the remainder of this chapter has already been described: non-physicalities *always* manifest themselves in the density profiles. Therefore, it should generically be suitable to correct density profiles and then recompute the resulting cluster to obtain a best estimate. This is the first approach which we will discuss, namely the naive approach. It will become clear that, while the naive approach satisfies all of the physical requirements, a more complex approach leads to more self-consistent clusters.

A.2.1 The Naive Approach

In a general cluster generation scenario, one obtains a complete set of density profiles $\{\rho_k\}$ which will possess the gas density and any $(n-1)$ additional species of matter specified. If that cluster is non-physical, then it will be true on some subset of the interval of interest that

$$\exists \rho_j \in \{\rho_k\} \text{ s.t. } \rho_j(r) < 0.$$

The immediate issue then becomes producing a correction. Because all of the generation methods which include a gasseous component require (again, to within an isomorphism) the gas density ρ_g and any $(n-1)$ additional species must be accompanied by $n-2$ constraints (the last being determined by conservation of mass). In most cases, the final (non-trivially constrained) species is the dark matter density; however, this need not generally be the case. Let the $n-1$ known density profiles be $\rho_2, \cdots \rho_n$. Because each of these is specified before hand, none is a derived quantity and it therefore follows that the condition

$$\rho_{\text{dyn}}(r) \geq \sum_{k=2}^{n} \rho_k(r) = \rho_{\text{crit}}(r) \;\; \forall r$$

is sufficient to create a correction. We define a corrected dynamical density such that

$$\rho'_{\text{dyn}}(r) = \begin{cases} \rho_{\text{dyn}}(r), & \rho_{\text{dyn}}(r) \geq \rho_{\text{crit}}(1+\varepsilon) \\ \rho_{\text{crit}}(1+\varepsilon), & \text{otherwise.} \end{cases}$$

Here, there is some freedom in the selection of ε, which we call the correction buffer. The idea is that if $\varepsilon = 0$, one may still find that the final derived density ($\rho_1(r)$) is zero (or worse, $-\epsilon_{\text{machine}} \leq \rho_1(r) \leq \epsilon_{\text{machine}}$), thus we let $\varepsilon \in (0,1)$ so that the remaining derived density is well constrained numerically. The new dynamical density may

then be passed back through the generation system (using ρ_g and ρ_{dyn}) to produce a corrected profile.

A.2.2 Numerical Methods

Before proceeding to the smooth correction method, some discussion must be had regarding specific numerical methods used in the implementation. In the naive approach, it was sufficient to define a continuous, piece-wise alternative to ρ_{dyn}; however, in attempting to produce a fully smooth density profile, a more complex methodology must be employed to determine the locations of the non-physical regions which must be corrected. This is the first algorithm which will be discussed and which will be called the "hole-identifying algorithm". Once the holes have been identified, the remainder of the correction process is to construct a smooth estimate to the original curve. This process we call the "hole-filling algorithm;" however, it should be noted that this methodology borrows heavily from monontone spine methods. Once both numerical methods have been described, it will then be possible to introduce the smooth correction methodology.

The Hole-Identifying Algorithm

In the smooth approach to correcting non-physical regions, the intuition behind the approach is to correct the ρ_{dyn} profile in such a way as to make it monotone and smooth. The first of these objectives is relatively trivial. Let $f : [a, b] \subset \mathbb{R} \to \mathbb{R}$ such that $f(a) \geq f(b)$. This may be arranged without loss of generality by transforming functions where $f(a) < f(b)$ such that $f(x) \to f(-x)$. It is then quite obvious that the closest monotone approximation of f on $[a, b]$ is

$$\tilde{f}(x) = \sup_{\xi \in [x,b]} f(\xi) = \max_{\xi \in [x,b]} f(\xi).$$

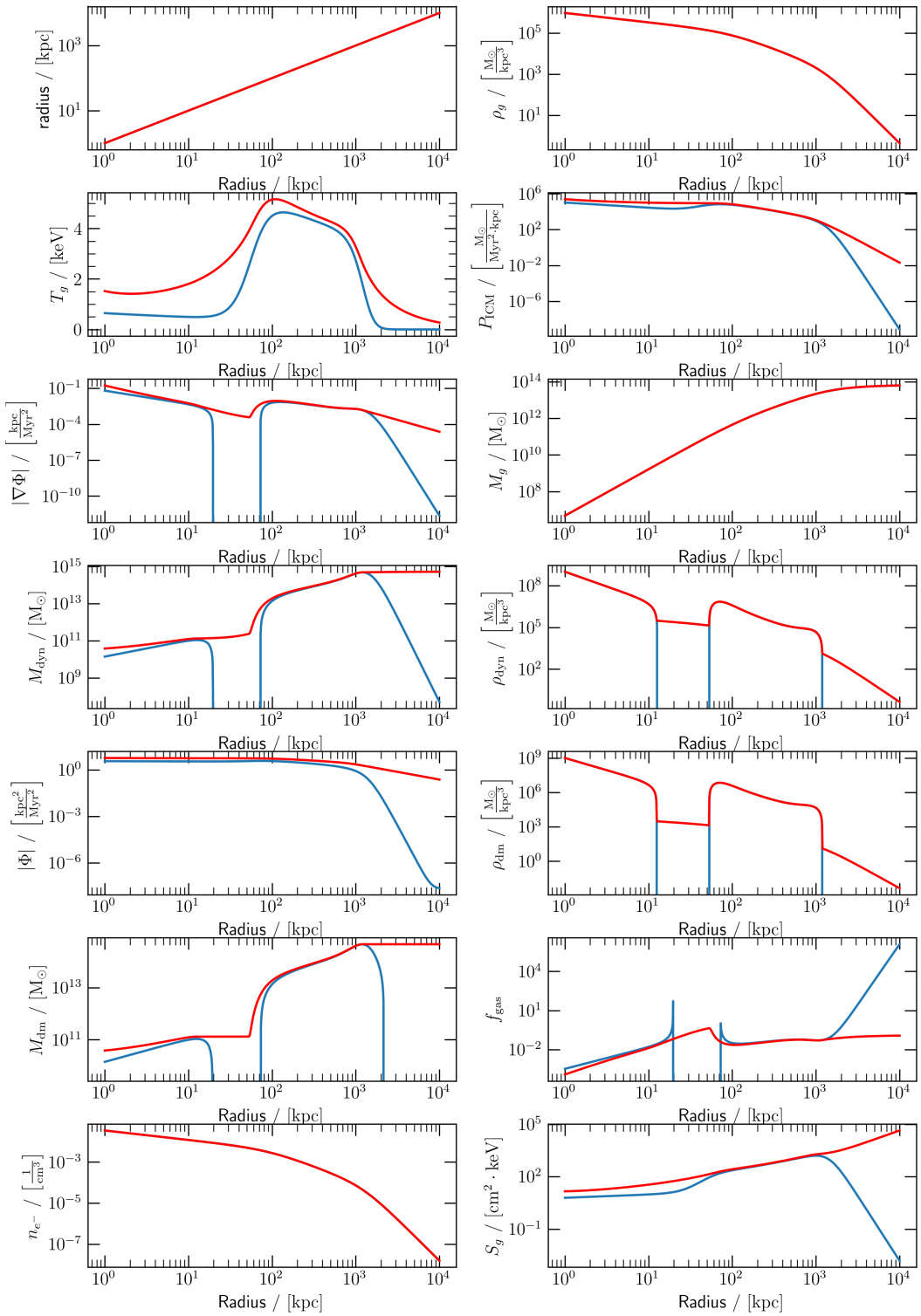

Figure A.1: Naive correction of a sample cluster with two non-physical regimes. The original (blue) clearly fails to be self-consistent while the corrected (red) is consistent but not particularly smooth.

While this function is decidedly continuous (if $f(x)$ is continuous) and monotone, it is not smooth. In order to produce a smooth and monotone analog of $\tilde{f}$, it is necessary to identify regions where $f(x) \neq \tilde{f}(x)$. These regimes indicate non-monotone behavior of f and therefore constitute "holes". The hole identification algorithm (HIA) is therefore designed to obtain these holes in a controlled and accurate way.

From a standpoint of maximal generality, we consider the problem of finding the holes in a profile described by N points $X = \{x_1 = a, \cdots, x_N = b\}$ and the corresponding $y_i = f(x_i)$ for some x_i. The function f is assumed to be at least $f \in C^1[a, b]$ and, without loss of generality, to satisfy the requirement that $f(a) > f(b)$. The intuition underlying this approach is exactly a discretized version of that described in the preceding paragraph, we construct the set

$$Z = \{\max_{j \leq k \leq N}(x_k) | \forall j \in [1, N] \cap \mathbb{N}\}, \tag{A.1}$$

which is the clear equivalent of $\tilde{f}$ from above. An additional set H is constructed to contain the holes such that

$$H_k = \begin{cases} 0, & x_k \geq z_k \\ 1, & \text{otherwise.} \end{cases} \tag{A.2}$$

While this simple sequence of steps is sufficient to identify the points in which holes arise, what is needed to proceed is precisely the boundaries of the unique holes. As such, identification of the hole boundaries is the next necessary step. To do so, we utilize the forward-difference on H in a manner layed out in the following lemmas:

Lemma A.2.2.1 (Left and Right Hand Boundaries)**.** *Let H be represented as an $1 \times N + 2$ matrix $\boldsymbol{H} = [1, H_1, \cdots, H_N, 1]$ such that the first and last component are* 1

and $\boldsymbol{H}_k = H_{k+1}$. *Then,* $\mathrm{Sum}(\boldsymbol{\Delta H}) = 0$, *where*

$$\boldsymbol{\Delta} = \begin{bmatrix} -1 & 1 & \cdots & \cdots & 0 \\ 0 & -1 & 1 & \cdots & \vdots \\ \vdots & \cdots & \ddots & \ddots & \vdots \\ 0 & \cdots & \cdots & -1 & 1 \end{bmatrix}$$

is the forward difference operator.

Proof. The proof of this lemma is largely trivial. In component form, $\boldsymbol{\Delta}_{ij} = -\delta_{ij} + \delta_{i,j-1}$. Therefore, $\boldsymbol{\Delta}\mathbf{H}$ is

$$(\boldsymbol{\Delta}\mathbf{H})_k = \boldsymbol{\Delta}_{kj}\mathbf{H}_j = -\delta_{kj}\mathbf{H}_j + \delta_{k,j-1}\mathbf{H}_j = H_{k+1} - H_k.$$

Thus,

$$\sum_{l=1}^{N+2} (\boldsymbol{\Delta}\mathbf{H})_l = \sum_{l=1}^{N+2} H_{l+1} - H_l = H_{N+2} - H_1 = 1 - 1 = 0.$$

□

While lemma A.2.2.1 is a largely trivial result in and of itself, an obvious corollary of the result is a critical result in our analysis: because $\mathbf{H}$ contains elements which are exclusively either 1 or 0, the above lemma makes clear that $\boldsymbol{\Delta}\mathbf{H}$ has an equal number of elements with value 1 as it does value -1. It is easily seen that the leading edge of any hole in our formalism is characterized by $H_k = 0, H_{k+1} = 1$ and that the trailing edge is characterized by $H_k = 1$ and $H_{k+1} = 0$. Because these correspond to values in $\boldsymbol{\Delta}\mathbf{H}$ of 1 and -1 respectively, it becomes immediately evident that one can locate the holes in the domain exclusively from the 1s and -1s of the hole vector $\mathbf{H}$. As such, we may write our hole finding algorithm as shown in algorithm 1. Several additional aspects are included in the written algorithm including the management

of persistent edge cases.

Because the hole identification algorithm need only be run on a single profile (ρ_{dyn}) and will generally only encounter arrays of length from $1 \times 10^4 \rightarrow 1 \times 10^6$, computational efficiency is not a primary concern and it is likely that considerable improvements could be made to the basic implementation of the algorithm explained here. Nonetheless, we note that because additions and subtractions are the only mathematical operations, and the distance between evaluation points will be (in all sensible cases) considerably larger than machine ϵ the algorithm is numerically stable. Furthermore, all of the list indexing operations are $\mathcal{O}(n)$ and the generation of $\mathbf{M}$ takes (in principle) $n^2/2$ flops, we recognize that this algorithm has a time complexity on the order of $\mathcal{O}(n^2)$. As such, this algorithm may be ill-suited to use on particularly large arrays; however, it is sufficient for the purpose described in this work.

Algorithm 1 Hole-Identification Algorithm

```
procedure HIA(x, y)
    idx ← [0, ··· , dim(y) − 1]
    if y[0] < y[−1] then                    ▷ reversing y if not decreasing.
        y ← y[:: −1]
    end if
                                            ▷ Construct the monotone array and build H.
    M ← [max(y[i :]) for i in idx]
    H ← zeros(dim(y) + 2)
    H[0] ← 1
    H[−1] ← 1
    H[M ≠ y] ← 1
                                            ▷ Determining holes.
    ΔH = H[1 :] − H[: −1]
                                            ▷ Building usable output arrays
    x, y, idx = [x[0], ∗x], [y[0], ∗y], [idx[0], ∗idx]  ▷ redundant 0 index for edge case.
    X_out = [x[ΔH = −1], x[ΔH = 1]]
    Y_out = [y[ΔH = −1], y[ΔH = 1]]
    I_out = [idx[ΔH = −1], idx[ΔH = 1]]
    return X_out, Y_out, I_out
end procedure
```

Monotone Interpolation

Having now illustrated the methodology from which holes in the density profile are identified, our goal now becomes to construct a relevant approach which approximates the original density profile ρ_{dyn} but which is smooth and monotone. To do so, we will borrow heavily from the theory of piecewise monotone cubic spine interpolation (PM-CSI). In this section, we will introduce the relevant background as described in Fritsch and Carlson [54] and Carlson and Fritsch [32] and implemented in Steffen [132] and in the next we will explore the modifications of these findings which are relevant to the hole-filling algorithm.

In an "archetypal" implementation, the goal of monotone interpolation is to take a set of N points $(x_i, y_i) \in \mathbb{R}^2$ (assumed to be ordered in increasing x) which are monotone in the sense that $\forall i \leq N$, either $y_i < y_j \ \forall j$ s.t $i < j \leq N$ or $y_i > y_j \ \forall j$ s.t. $i < j \leq N$ and produce some function $f(x)$ which is monotone in the same direction as the points and for which $f(x_i) = y_i \ \forall i < N$. In Fritsch and Carlson [54], an algorithm is illustrated which utilizes cubic Hermite interpolation to determine the relevant slopes $y_i' = f'(x_i)$ for which the piecewise cubic spline constructed is monotone. While this approach is well founded in a more general set of numerical problems, the hole-filling problem does not, generally, provide the necessary assumption of monotone interpolant points and thus cannot be unilaterally subjected to the algorithm. Instead, we take a different approach; to correct the non-physicalities in the profiles, we instead use the hole-identification algorithm (algorithm 1) to find holes (i.e. $[h_{0,a}, h_{0,b}]$) and then attempt to "patch" those holes with a single cubic which interpolates the profile's points on some domain containing the hole and which is sufficiently (C^1) smooth on the interval.

In constructing this method, the following theorem (which has a more general form proven in Fritsch and Carlson [54]) is of critical importance:

Theorem A.1 (Monotonicity of Cubics)**.** *Let* (x_0, y_0) *and* (x_1, y_1) *be two points in*

$\mathbb{R}^2$ *such that* $x_1 > x_0$. *Let* $P_3(x)$ *be the unique cubic polynomial passing through each of the points and having derivatives* d_0 *and* d_1 *at* x_0 *and* x_1 *respectively. Furthermore, let* $\Delta = (y_1 - y_0)/(x_1 - x_0)$, $\alpha = d_0/\Delta$ *and* $\beta = d_1/\Delta$. *If the signs of each of the derivatives and of* Δ *are equal, then*

$$\alpha + \beta \leq 2 \tag{A.3}$$

is a sufficient condition to guarantee that $P_3(x)$ *is monotone on* $[x_0, y_0]$.

Proof. To begin, let $f(x)$ be an arbitrary ($C^1[x_0, x_1]$) function on $[x_0, x_1]$ subject to the constraint that it's value and derivative match y_0, d_0 and y_1, d_1 at the relevant points. It is a trivial implication of the Intermediate Value Theorem that, if $\text{sgn}(d_0) \neq \text{sgn}(d_1)$, then there exists $c \in [x_0, x_1]$ for which $f'(c) = 0$. Furthermore, because the sign of the derivative changes over the interval, c is either a local minimum or a local maximum thus prevents $f(x)$ from being monotone on the interval. Futhermore, if the signs of d_0 and d_1 do not match Δ, then monotonicity necessarily violates the Mean Value Theorem. Thus, we recognize that $\text{sgn}(d_0) = \text{sgn}(d_1) = \text{sgn}(\Delta)$ is a necessary condition for the monotonicity of any interpolate $f(x)$ which meets our criteria. In the remainder of this proof, we assume the previous assertion is true. Finally, if $\Delta = 0$, then the interpolation function $f(x)$ must be 0 $\forall x \in [a, b]$. Thus, we assume in what follows that (without loss of generality), $\Delta \neq 0$.

For simplicity of the formulae, we assume (WOLOG) that $x_0, y_0 = (0, 0)$ and that $x_1 = h$. If $f(x)$ is a polynomial of degree three, then it may be expressed in the Newton form of the interpolating polynomial by divided difference:

$$P_3(x) = \underbrace{d_0}_{p_1} x + \underbrace{\frac{\Delta - d_0}{h}}_{p_2} x^2 + \underbrace{\frac{d_0 + d_1 - 2\Delta}{h^2}}_{p_3} x^2(x - h).$$

Taking derivatives of the expression,

$$P_3'(x) = p_1 + 2x(p_2 - hp_3) + 3p_3x^2 \tag{A.4}$$

$$P_3''(x) = 2(p_2 - hp_3) + 6p_3x. \tag{A.5}$$

Two of cases now arise.

- $(d_0 + d_1 - 2\Delta = 0)$. In this case, $P_3(x)$ is quadratic and the derivative is clearly linear. Because d_0 and d_1 share sign and a linear function has no (local) minima or maxima within its domain, it is clear that P_3 must be monotonic on $[x_0, x_1]$. Note that this condition is equivalent to $\alpha + \beta - 2 = 0$.

- $(d_0+d_1-2\Delta \neq 0)$. In this case, $P_3'(x)$ is a quadratic which allows for some deduction. Clearly $P_3'(x)$ connects the points (x_0, d_0) and (x_1, d_1). Because $P_3'(x)$ is continuous, the intermediate value theorem implies that it achieves a minimum and a maximum on $[x_0, x_1]$. Because it is a quadratic, only one of those may be away from the boundary. Thus, if P_3' is concave down, then $\min\{d_0, d_1\} \leq P_3'$ on $[x_0, x_1]$. Similarly, if P_3 is concave up, then $P_3' \leq \max\{d_0, d_1\}$ on $[x_0, x_1]$. The leading term in P_3' is $3p_3$, implying that if $d_0 + d_1 - 2\Delta < 0$, then P_3' is concave down and $d_0 + d_1 - 2\Delta > 0$, then P_3' is concave up. More generically, if P_3' is expressed as

  $$\frac{1}{\Delta}P_3'(x) = \xi(x) = \frac{p_1}{\Delta} + \frac{2x}{\Delta}(p_2 - hp_3) + 3(\alpha + \beta - 2)x^2,$$

  one may recognize that $\alpha, \beta > 0$ and that $\xi(x)$ is a quadtratic which passes through the points (x_0, α) and (x_1, β). Thus, because α and β are strictly positive, $\xi(x)$ being concave down is a sufficient condition for the polynomial to be monotonic. Thus, $\alpha + \beta - 2 < 0$.

Combining the findings of the two cases, we recognize that the proof has been shown.

$\square$

The precursory mathematics has now been completely described and the final remaining objective is to use this finding to implement a practical algorithm for hole filling.

The Hole-Filling Algorithm

The goal of the hole filling algorithm is to construct a smooth cubic which "covers" an identified hole in a profile in a monotonic way. More formally, let $f(x) : [a, b] \to \mathbb{R}$ be a generally decreasing function ($f(a) > f(b)$). Assume that there is some hole in $[h_0, h_1] \subset [a, b]$ and let $(x_0, y_0) = (h_0, f(h_0))$ and $(x_1, y_1) = (h_1, f(h_1))$. The intuition for the approach which will be rigorously explored below is that one would like to find some $x_\star \in [a, x_0]$ for which the interpolatory cubic from $(x_\star, f(x_\star))$ to $(x_1, f(x_1))$ is smooth and monotone. From theorem A.1, it is clear that for such an interpolatory cubic to be possible, one requires that

$$\frac{f'(x_\star)}{\Delta_\star} < 2,$$

where

$$\Delta_\star = \frac{f(x_\star) - f(x_1)}{x_1 - x_\star},$$

and we have utilized the (as yet unproven but intuitive) fact that $f'(x_1) = 0$. It is thus relatively intuitive that one may make the desired correction by identifying the first valid $x_\star$ for which the property holds. In the remainder of this section, a more thorough development of this intuition will be developed and methods for cases wherein no $x_\star$ may be found are discussed.

As yet, we have discussed only polynomials; however, ρ_{dyn} is most manageable

(numerically) as a logarithmic function of the form

$$\log(\rho_{\text{dyn}}) = \xi(x), \quad \text{where } x = \log(r).$$

We therefore proceed in our description by treating functions $\Xi(X)$ and $\xi(x)$ as isomorphic when they are of then form

$$\Xi(X) = \exp[\xi(\log(X))].$$

For brevity, we describe this isomorphism as being an isomorphism under the map $\pi(\Xi) = \xi$ and $\pi^{-1}(\xi) = \Xi$. In light of this notion, the hole filling algorithm proceeds by taking as inputs an ordered set of points $\mathbf{X} = \{X_1 = A, \cdots, X_n = B\}$ and a corresponding set of profile values $\mathbf{Y} = \{Y_1 = F(X_1), \cdots, Y_N = F(X_N)\}$, where $F : [A, B] \to \mathbb{R} > 0$ is at least $C^1[A, B]$. The transformation under π can then be performed to produce some $f(x) : [a, b] \to \mathbb{R} > 0$ such that $\pi(F(\mathbf{X})) = f(\mathbf{x})$ where $\mathbf{x} = \{x_1 = a = \log(A), \cdots, x_n = b = \log(B)\}$. From this definition, one clearly finds that an analogous $\mathbf{y}$ may be defined as $\{f(x_i), x_i \in \mathbf{x}\}$. Due to the nature of the mapping π, it is immediately clear that $\forall F(x) : [A, B] \to \mathbb{R} > 0$, $F(x)$ is monotone if and only if $f = \pi \circ F$ is also monotone on $[\log(A), \log(B)]$. It thus follows that the set of holes $\mathcal{H}_{[A,B]}(F)$ is equivalent to $\mathcal{H}_{[\log(A),\log(B)]}(\pi \circ F)$. Because the holes are analogous, it is possible to correct each hole in a recursive fashion. For each hole $H_i = [h_{i0}, h_{i1}]$, as ordered in increasing x_i, the correction scheme discussed above may be employed. The relevant secants d_j between elements of $\mathbf{x}$ and $\mathbf{y}$ are determined in the range $[a, h_{i0}]$ and for each $x_k < h_{i0}$ in $\mathbf{x}$ the secant slope $\bar{d}_k$ between (x_k, y_k) and $(h_{i1}, f(h_{i1})$ is determined. The closest such x_k for which the $(d_k/\bar{d}_k) < 2$ is chosen as the cubic interpolation point and the array $\mathbf{y}$ is updated to fill the hole. If no such point x_k exists, which is generically a possibility, then the point (x_1, y_1) is used as the interpolation point and its secant is adjusted satisfy the criteria for monotonicity.

A pseudo-code implementation of the algorithm is shown in algorithm 2. The numerical complexity of the algorithm is not easily identified by inspection; however, it must clearly be largely dependent on the number of holes which must be corrected. On a hole-by-hole basis, a single correction step should take on order n^3, where n is the length of the x and y arrays. This is easily seen by recognizing that the hole-identification step (algorithm 1) takes $\mathcal{O}(n^2)$ time to locate all of the holes and the search stage of the filling algorithm requires an additional (at most) n iterative operations to identify valid interpolation bounds. Nonetheless, the use case in which this algorithm is most useful needs no meaningful efficiency for non-pathological problems.

Algorithm 2 Hole-Filling Algorithm

```
procedure HFA(X, Y, Y')
                                                    ▷ Array Management.
    x, y ← log(X), log(Y)
    δ ← (X/Y)Y'
                                                    ▷ Correcting Holes.
    H ← HIA(x, y)
    repeat
        h_x, h_y, h_i ← H[:, 0, :]                  ▷ Pull 2-tuple hole info.
        d ← δ[0 : h_i[0]]                           ▷ candidate point slopes
        S ← (y[0 : h_i[0]] − h_y[1])/(x[0 : h_i[0]] − h_x[1])
                                    ▷ Check for existence of a valid interpolation point.
        if ∃i ∈ {0, ··· , h_i[0]} s.t. d[i]/S[i] < 2 then
            i_⋆ ← {0, ··· , h_i[0]}[d/S < 2][−1]
        else
            δ[0] ← S[0]                             ▷ Fix edge slope to allow for interp.
            i_⋆ ← 0
        end if
                                                    ▷ Constructing the interpolation.
        h ← h_x[1] − x[i_⋆]
        d_0, d_1 ← δ[i_⋆], 0
        Δ ← S[i_⋆]
                                                    ▷ Build polynomial
        poly ← LAMBDA (ξ = x − x[i_⋆]) : y[i_⋆] + d_0 ξ + ξ^2(Δ − d_0)/h + ξ^2(ξ +
    x[i_⋆] − h_x[1])(d_0 − 2Δ)/h^2
        y[i_⋆ : h_i[1]] ← poly(x[i_⋆, h_i[1]])
                                                    ▷ Locate new holes
        H ← HIA(x, y)
    until length(H) = 0
                                                    ▷ Clean up
    X, Y ← exp(x), exp(y)
    return X, Y
end procedure
```

Appendix B

Mathematical Derivations

B.1 MOND+DM Constraints

In order to produce a physically allowable phantom mass profile, $\rho_{\rm ph} \geq 0 \iff \partial_r M_{\rm ph} \geq 0$. Let

$$\gamma(r) = \frac{G\tilde{M}_{\rm dyn}(< r)}{a_0 r^2}.$$

This should be interpreted as the *relative acceleration scale* for the cluster at radius r, with $\gamma \ll 1$ implying a deep-MOND regime and $\gamma \gg 1$ implying a Newtonian regime. By differentiating Equation 3.1;

$$\partial_r M_{\rm ph}(< r) = \partial_r \left[\tilde{M}_{\rm dyn}(< r)\mu \left(\frac{|\tilde{\Gamma}(\rho_g, T_g)|}{a_0} \right) \right] - \partial_r M_g(< r).$$

Recall that Γ is *invariant* between each of the two paradigms in the context of the theorem, *ergo*,

$$\frac{|\tilde{\Gamma}(T_g, \rho_g)|}{a_0} = \frac{|\Gamma(T_g, \rho_g)|}{a_0} = \gamma(r),$$

leading to the simplified inequality

$$\partial_r \tilde{M}_{\rm dyn}(<r)\left\{\mu(\gamma)+\gamma\partial_\gamma\mu(\gamma)\right\}-\frac{2\gamma}{r}\tilde{M}_{\rm dyn}(<r)\partial_\gamma\mu(\gamma)\geq\partial_r M_g(<r).$$

Further simplification here is not particularly fortuitous; however, if one constrains the class of interpolation functions μ to the form

$$\mu_\alpha(x)=\frac{x}{(1+x^\alpha)^{1/\alpha}},$$

then

$$\partial_\gamma\mu(\gamma)=\frac{\mu(\gamma)}{\gamma(\gamma^\alpha+1)},$$

which implies that

$$\mu_\alpha(\gamma)\left\{\partial_r\tilde{M}_{\rm dyn}(<r)+\frac{r\partial_r\tilde{M}_{\rm dyn}(<r)-2\tilde{M}_{\rm dyn}(<r)}{r(\gamma^\alpha+1)}\right\}\geq\partial_r M_g(<r)\geq 0 \quad \text{(B.1)}$$

with the final inequality following on physical assumptions about the gas profile. Further simplification results in

$$\frac{d\ln(\tilde{M}_{\rm dyn}(<r))}{dr}\geq\frac{2}{r(\gamma^\alpha+2)}=\frac{1}{r\left(\frac{\gamma^\alpha}{2}+1\right)}\geq\frac{1}{r(\gamma^\alpha+1)}. \quad \text{(B.2)}$$

This is the extent of the analysis without further simplification. Because γ has no upper bound, there is no further relaxation without imposing cases.

1. ($\gamma>1$): In this case, the cluster resides in a Newtonian regime and because $\gamma>1$,

$$\forall r,\exists\,\alpha\ \text{ s.t. }\ \frac{d\ln(\tilde{M}_{\rm dyn}(<r))}{dr}\geq\frac{1}{r(\gamma^\alpha+1)}.$$

This value of α, denoted $\bar{\alpha}$ may be thought of as the minimal interpolation scale at which the cluster is viable to a radius r.

2. ($\gamma \leq 1$): In this case, we note that $\gamma \geq \gamma^{\alpha}$ for any positive integer α; therefore the inequality simplifies to the form

$$\frac{d\ln(\tilde{M}_{\rm dyn}(<r))}{dr} \geq \frac{1}{r(\gamma+1)} \geq \frac{1}{2r}.$$

Written in terms of the density,

$$\tilde{\rho}_{\rm dyn}(r) \geq \frac{\tilde{M}_{\rm dyn}(<r)}{8\pi r^3} \geq \frac{\langle\tilde{\rho}_{\rm dyn}\rangle_r}{6};$$

where $\langle\tilde{\rho}_{\rm dyn}\rangle_r$ denotes the average density of the cluster within the radius r.